FINAL REPORT

to

National Aeronautics and Space Administration
Lewis Research Center

Design and Development of Experimental Facilities for Short Duration, Low-Gravity Combustion and Fire Experiments

Vahid Motevalli
Mechanical Engineering Department
Worcester Polytechnic Institute
100 Institute Rd.
Worcester, MA 01609

Grant NCC3-312
May 25, 1993 - May 5, 1994

June 30, 1994

Executive Summary

This report contains the results of three projects conducted by undergraduate students from Worcester Polytechnic Institute at the NASA's Lewis Research Center under a NASA Award NCC3-312. The students involved in these projects spent part of the summer of 1993 at the Lewis Research Center (LeRC) under the direction of Dr. Howard Ross, head of the Combustion group and other NASA engineers and scientists. The Principal Investigator at Worcester Polytechnic Institute was Professor Vahid Motevalli. Professor Motevalli served as the principal project advisor for two of the three projects which were in Mechanical Engineering. The third project was advised by Professor Duckworth of Electrical and Computer Engineering, while Professor Motevalli acted as the co-advisor. These projects provided an excellent opportunity for the students to participate in the cutting edge research and engineering design, interact with NASA engineers and gain valuable exposure to a real working environment. Furthermore, the combustion group at LeRC was able to forward their goals by employing students to work on topics of immediate use and interest such as experimental research projects planned for the space shuttle, the future space station or to develop demonstration tools to educate the public about LeRC activities.

This report has been divided to three sections, each representing the outcome of the separate projects. The three reports which have been written by the students under the supervision of their advisors have been compiled into a combined report by Dr. Motevalli. Each project report is presented here as a section which are essentially self-contained. Each section contains chapters introducing the problem, solution approach, description of the experiments, results and analysis, conclusions and appendixes as appropriate. In this summary, the contents of each segment have been briefly discussed.

Section One describes the design and testing of a Miniature Drop-tower. A low-gravity miniature drop-tower, in principle similar to the actual NASA low-gravity drop tower facility, was designed and constructed which met the following requirements:

I. Light weight: total weight less than 34 kg, individual piece < 9 kg.
II. Flexible, portable, and assembly parts no longer than 1.2 m each.
III. Ease of assembly. (assembled in order of few minutes (< 10).
IV. Minimize vibration during the drop and inherently safe design.
V. Successfully demonstrate the effect of low-gravity and readily usable as a demonstration tool.

The Miniature drop tower has variable heights of 2.4 m, 3.0 m and 3.6 m. These heights provide low-gravity periods between 0.7 to 0.9 seconds. The tower consists of a simple smooth shaft with a payload platform which falls down guided by this control shaft. The shaft consists of 1.2 m long connectable pieces that can be extended from the normal operating height of 2.4 m to 3.0 m and 3.6 m lengths. A number of experiments were developed to demonstrate the

low-gravity effect. This was achieved by placing a video camera on the platform to record the event and then replaying the film in slow-motion to demonstrate the effect of lowered gravity on such phenomena as a swinging pendulum, burning candle, a weight scale measuring a fixed mass, etc. Each of these experiments are described in details within the body of the report. Measurement of the acceleration of the payload platform was performed by visual frame by frame analysis of drops. The deceleration of the platform on capture was measured by an accelerometer.

A pictorial record of the experiments comparing the low-g and 1-g conditions are presented in the Appendix A of Section One. Detailed schematic drawings of the tower are included in Appendix B. Measurements of the acceleration and deceleration at capture of the platform are documented in Appendixes D and F, respectively. A short manual describing the assembly procedure of the tower has been provided in appendix G this section.

Section Two describes the development and testing of a smoke generation apparatus for use in a Glovebox Smoke Diagnostics Experiment. This Glovebox experiment was intended to be flown aboard the space laboratory. The apparatus consisted of simple fuels (teflon and silicon rubber) heated to generate an average 2 ppm of smoke yield at a target detector. These material were selected as part of a smoke detector test program due to the likelihood of such materials being exposed to overheating in wiring and electrical systems. The smoke yield had to be achieved for a 1.0 cm/sec velocity in a low gravity environment. This is deemed to be a severe test for light scattering smoke detectors which are more suited for detection of smoldering fires. In the One-g environment, the experiment could not duplicate such a low velocity condition. Therefore, a test program was developed to determine the required power input for a heated wire element, wrapped around the fuel sample, which would yield the necessary smoke concentration, but at higher flow velocities. It was then stipulated that one could extrapolate the power input needed for the 1 cm/sec velocity condition (i.e. simply ventilation induced flow conditions onboard the space shuttle). However, simple extrapolation would be extremely unreliable. Hence a simple heat transfer model was developed to predict the power requirement. The experiments were conducted for two qualitative temperature levels, high and low. The high temperature represented a fast rise to the smoke yield level, where the sample fuels exhibited clear signs of pyrolysis and charring and often resulting in ash formation. For the "low temperature" case, only signs of degradation and pyrolysis of the fuel were evident at the location of the wire wrap. The result of the heat transfer analysis were quite promising for the low temperature case, while the difference between measurement and predictions were quite high for the high temperature case. The measured power input to the heating element simply consisted of the measurement of the current and voltage to the wire. A heat transfer analysis of the wire and test material at steady state condition was performed to predict the total heat loss which was assumed to be equal to the power input. The heat losses included the wire losses (by both convection and radiation) and losses by the test specimen. The wire heat losses were separated for the part in contact with the wire and that exposed to the surrounding. The wire wrap around the specimen for the "high temperature" case was quite different. It is stipulated that this and assumption of an infinite fin for the test specimen may have resulted in

the high difference between the calculated vs. measure values at the higher temperature. Furthermore, it is unclear if the simple measurement of the power input to the heating element is accurate. Never-the-less, the heat transfer analysis is a more sound approach to try to establish the required power for the apparatus to yield the desired smoke density in microgravity conditions.

The test results, in this section, are categorized into low and high temperature cases. The results are tabulated and plotted in Appendix A. The mathematical relationship and numerical calculations are shown in Appendix B of the report. Appendix C contains some supplementary calculations.

Section Three This section describes the design and construction of a portable and universal laser detection unit to measure relative power signals from a laser system. NASA Lewis Research Center plans to use laser diagnostic systems to measure combustion parameters for a better ground-based quantification of experiments designed for future micro-gravity experiments. The intensity of the laser light is a key parameter in the laser diagnostic measurements. A certain level of power fluctuation in the laser intensity (especially in pulsed lasers) is expected, however, the level of fluctuation must be quantified. The goal of the project was to develop a laser monitoring system to measure the relative magnitude of each laser pulse.

The laser pulse power measuring system had to have the following characteristics:

- Small enough for future incorporation into experimental packages.
- Portable to be moved to different laser systems.
- Fast response detector and associated circuit to capture 5 ns laser pulses being emitted every 20 ms.

The monitoring system consist of a pyroelectric detector and linear amplification circuit. A separate circuit was designed to enable consecutive measurements of laser pulses.

The report contains the detector selection process, circuit design and testing of the circuits. The output of the system was a normalized and integrated value of the laser power intensity and it can be used as a relative measure of intensity difference between consecutive pulses of a pulsed laser.

SECTION 1

THE MINIATURE DEMONSTRATION DROP TOWER

by

Michael Pereira

T.J. Marsden

Prepared, in part, as a Major Qualifying Project in
Mechanical Engineering Department
Worcester Polytechnic Institute
1993-94

Table of Contents

List of Figures

Acknowledgments

We would like to take the opportunity to thank the following people, without whose help this project would not have been possible:

Professor Vahid Motevalli

Howard Pearlman

David Urban

Howard Ross

Dennis Stocker

Andrew Jenkins

Tom Kahoe

Mike Johnston

Andy Jenkins

Dan Gotti

Jeff Goldmeer

L.J. Dallaire

Chris Toth

Nomenclature

g	- gravitational constant ($9.81 m/s^2$)
g_o	- local gravity level
R_o	- radius of earth (6386 kilometers)
h	- local height (meters)
t	- time (seconds)
D	- distance (meters)
V	- velocity (meters/second)
M,m	- mass (kilograms)
a	- acceleration (meters/second^2)
F	- Force (Newtons)
F_b	- Buoyancy force (Newtons)
F_m	- Magnetic force (Newtons)
T	- Tension (Newtons)

Chapter 1. Introduction

1.1. Environment and Equipment

The National Aeronautics and Space Administration has several ongoing experiments in the fields of advanced aeronautics, avionics, propulsion, materials and space flight. In the field of space flight, one of the most important consideration is the effect of gravity. The best experimental platform to study nearly zero gravity effects are the space shuttles; reusable vehicles that are able to obtain an orbit, remain there for a variable period of time and return to Earth. While in orbit, the shuttle experiences a state of microgravity (i.e. 10^{-6}g). It is a common misconception that the shuttles are in a state of zero-gravity and that the effects of Earth's gravity no longer act upon it. The orbiter actually escapes less than ten percent of the Earth's gravitational effects. To truly escape the gravitational field the shuttle would have to be 3.7 million miles away.(Walter, 1987) To determine the amount of influence the Earth's gravity has upon an object at a particular distance, the following equation must be used:

$$g = \left[R_o/(R_o + h)^2\right]g_o \qquad (1.1)$$

where g is the local gravity level, R_O is the radius of the Earth (approximately 6386 kilometers), h is the local height above the Earth and g_O is the gravitational acceleration at sea level (9.81 m/sec).(Serway, 1990)

The space shuttle is able to experience microgravity because it is in a constant state of free-fall. "Gravity is pulling "down" on the rocket, causing it to "fall". Rather than coming straight down, the forward velocity of the rocket causes it to fall in a curved path; an orbit. As long as the forward velocity vector remains constant, the rocket will remain in orbit."(Walter, 1987) The distance gravity pulls the shuttle down is equal to the distance the Earth has curved away from the shuttle. An example can be seen in the

following illustration:

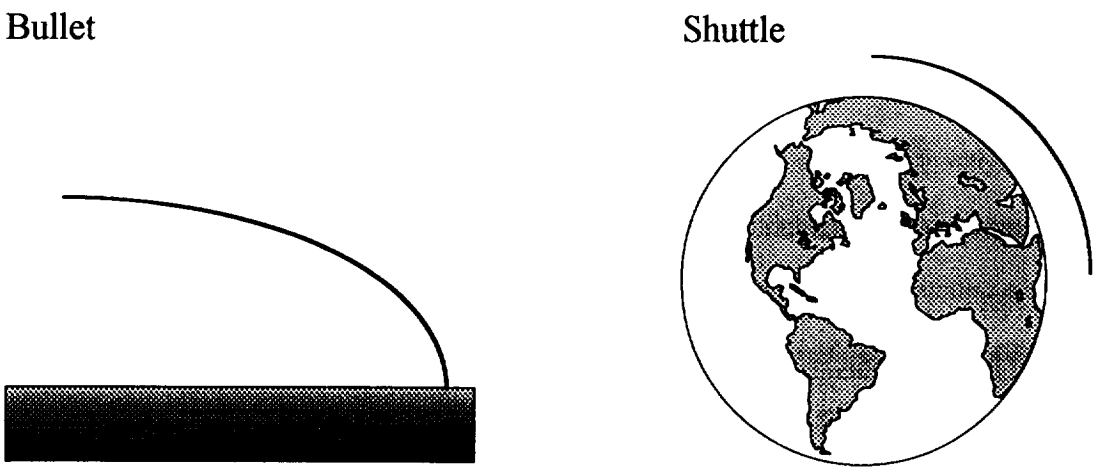

Figure 1.1 Comparison of a Bullet and the Shuttle

It can be seen in Figure 1.1 that a projectile, such as a bullet, with some initial velocity, will travel for a distance before the effects of gravity pull it to the surface. In the second figure, the projectile, in this case the space shuttle, is being influenced by gravity, but the shuttle's velocity is great enough so that the distance gravity has pulled it is equal to the distance of the Earth's curvature.

In this state of free-fall the effects of gravity are considered minimal. Ideal weightlessness is not physically possible to obtain, due to several disturbances that will create gravity-like disturbances. The first disturbance would be that the gravity and centrifugal force of the shuttle are only balanced at the craft's center of mass. In all other areas, the imbalance of these two forces creates a force called the "tidal force". A second disturbance is that spacecraft usually rotate around their center of mass while they are in orbit, creating additional centrifugal and tangential forces. Another concern is that the shuttle does experience some other forces while in orbit, primarily due to atmospheric drag, which will induce other types of acceleration upon the center of mass. The combination of all these gravity-like forces are approximately 1×10^{-6}, thus the term

microgravity is used to describe the environment that the shuttle operates in while it is in orbit.(Walter, 1987)

1.2 Ground Based Simulations

There are many experiments that can be carried out in the state of microgravity in the fields of Combustion Science, Fluid Mechanics, Biotechnology, and Material Science. A microgravity environment has unique characteristics that allow the investigation of characteristics and behaviors that are impossible to witness in the presence of gravity. It is possible to study the microgravity environment upon the space shuttle, but it is expensive and time consuming to do so. A simpler method had to be devised to simulate the low gravity environment. There basically three methods of simulating microgravity; sounding rockets, allowing a plane to fly a parabolic trajectory or to drop an experimental package in a free fall which will experience low gravity.

Sounding Rockets are fired from Earth and cruise to an altitude above 90 km where aerodynamic forces are sufficiently low. At this point the motor is released and an experimental package is allowed to freefall until approximately 5 km, when a parachute opens. Sounding rockets will provide ten to fifteen minutes of low gravity; achieving accelerations of approximately 10^{-4} of normal gravity.(Walter, 1987) These rockets are cost effective means of developing complex experiments. The safety requirements are much less stringent than those for shuttle experiments and the lead time is not as great.

Aircraft parabolic flight patterns are another method of conducting low gravity experiments. The aircraft that NASA uses for large low gravity experiments are the KC-135, Lear Jet and DC-9 which are able to achieve an acceleration of 10^{-2} - 10^{-3} for eighteen to thirty seconds.(NASA 10113, 1992) The low gravity is only obtainable when the experimental package is allowed to free float within the aircraft and does not come into contact with any other object. If the package is in contact with the airframe vibrations from the engines or turbulence will drastically effect most experiments.

Shuttles, aircraft and sounding rockets are known as orbital flight simulations of low gravity. Another method of creating a low gravity environment is vertical free fall simulations which can be performed in a drop tower.

A drop tower is a facility that will release an experimental package, allow it to free-fall through a distance and safely decelerate it at the bottom. The towers at the NASA Lewis Research Center are designed to provide several seconds of micro gravity and are, therefore, quite large. The design and operation of the NASA drop towers will be described in Chapter 2.

1.3 Motivation

NASA would like to be able to create a small version of a tower that would be classified as a Miniature Drop Tower.

The Mini-Drop Tower will be a structure that is fully portable. In this way, some of the microgravity experiments and results will be able to be seen by the general public. This new mini-tower can be used for demonstrations to varying audiences; other scientists within NASA, high school and college students and science fairs.

The objective of this project is to design and create a demonstration device that will fulfill the needs and concerns stated by NASA. It has been determined that the device should conform to four governing design parameters:

- Portability
- Visual Effectiveness
- Vibration
- Safety

which will all be discussed in depth in Chapter 3. Design and construction of the tower was completed at the NASA Lewis Research Center, Cleveland, Ohio under the guidance of the Microgravity Combustion Group (refer to Appendix A).

Chapter 2. Background

The most commonly used drop tower at the Lewis Center is the 2.2 second tower which is able to simulate g-levels of 10^{-5}g. The tower is housed in an eight story building that has a rectangular hole cut in the center of all the floors. This allows for an experimental package to be dropped a distance of approximately 26.8 meters. (NASA 10113, 1992) The method for determining the amount of distance needed to obtain a desired amount of freefall follows the equation:

$$D = \frac{1}{2} g t^2 \qquad (2.1)$$

From this equation, to obtain 2.2 seconds of drop time, the experiment must be allowed to fall 23.8 meters. The tower that the experiment is in must be larger than 23.8 meters to allow for a release mechanism, as well as, a deceleration mechanism. In the case of the 2.2 tower, the release mechanism is a string of piano wire. The wire is notched just before the fall and fails due to the tension load upon it. In this fashion, the release produces no side forces that would interfere with the experimental package. The capture is a large bin of sand that decelerates the package at an acceptable rate. Another concern in the use of drop towers is the effect of air drag upon the experimental packages. The force of air pushing "up" upon the package as it falls will result in reduced acceleration and, therefore, and increased g-level. The effects of air drag are minimized on the 2.2 second tower by allowing the experimental package to fall within a free falling drag shield. The package and the shield are independent so that air will slow the drag shield, but would not effect the package inside.

NASA also has a drop tube that is capable of providing 5.18 seconds of 10^{-5}g. In this case a hole 154.8 meters deep, has been dug into the ground. When a payload package is dropped, it experiences 132.0 meters of free-fall.(NASA, 1993) The packages

fall into a bin of styrofoam beads for deceleration. The problem of air drag is eliminated in the drop tube by evacuating the air from the tube (evacuated chamber @ 10^{-2} Torr) prior to dropping the experimental package.(NASA 10113, 1992)

One unique way of countering the effects of air drag is employed by the Japanese. In their ten second tower, where g levels of 10^{-4} are obtained, the experimental package is placed in a large drag container which is equipped with rockets.(NASA 10113, 1992) The container is then evacuated so that the payload will experience no drag within the shield. The rockets are used to propel the entire container down the shaft. Without rocket assistance the container would reach terminal velocity before it reached the bottom of the shaft. Terminal velocity is reached when the effects of gravity and air drag match each other and an object is no longer accelerating while it is in free-fall. If the drag shield was no longer accelerating and traveling at a constant velocity; the payload, which is still accelerating, would catch up to the shield very quickly. Rockets in the Japanese tower ensure that the drag shield is always accelerating. The Japanese experimental packages are guided down on a system of magnetic rails. While the package is falling, the rails and package have like charges, repelling one another, resulting in magnetic suspension and no frictional losses. When the package nears the bottom, the charge is slowly changed to opposite charges and the package is slowed in a controlled fashion by magnetic breaking.(Urban, 1993)

Chapter 3. Requirements

The Miniature Demonstration Drop Tower is designed around four fundamental concepts; portability, visual effectiveness, minimal vibration and safety. The tower is a demonstration device that is used to display the effects of low gravity to several audiences.

3.1 Lightweight

The first practical requirement is that the tower must be light weight so that one to two persons are able to transport it easily and that no one part is particularly heavy or cumbersome. With this concept in mind, the tower was designed to weigh less than seventy-five pounds, when fully assembled, and that individual pieces could not weigh more than twenty pounds.

3.2 Portability and Ease of Assembly

The next requirement was the size and portability of all the separate components. The first potential problem is the overall length of any one component. The principal behind any drop tower is that to experience low gravity, an object must be allowed to free-fall over a great distance, therefore, the support and hoist mechanisms for the tower would have to be tall in order to obtain any useful results. The tower was designed so that it would be of variable height, eight, ten or twelve feet, and that no single section will be more than four feet six inches. This length was chosen as the maximum length of any section so that all of the pieces would be able to fit into the back seat or the trunk of most cars. The second factor in the category of portability was that the tower had to be assembled in the field, quickly and easily. Although the tower is at least eight feet tall, the design has tried to alleviate the need for a step ladder and a great deal of tools and equipment. It was deemed optimal if the tower could be assembled by one person with only a few simple tools, such as a crescent wrench and a screwdriver.

3.3 Vibration

The third, and potentially the most difficult requirement of the tower was minimizing vibration in the tower. The design of the tower was centered around a solid steel shaft provided by NASA. The initial NASA design had an eight foot shaft that was supported at the base by a one inch screw. This set up is similar to a cantilever beam and therefore had a great deal of deflection at the top of the shaft when any side force was imparted onto the shaft

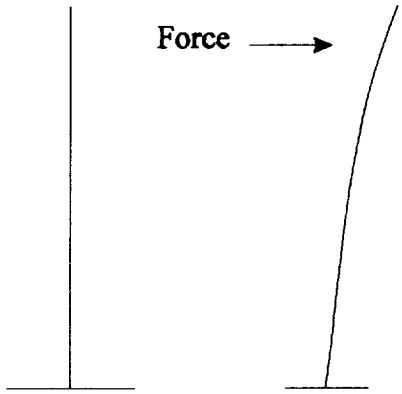

Figure 3.1 Beam Supported at One End

As seen in Figure 3.1, as a force is applied to the shaft, it will bend. In an attempt to eliminate a great deal of this deflection, and in turn eliminate vibration, the tower will be supported at both the top and the bottom.

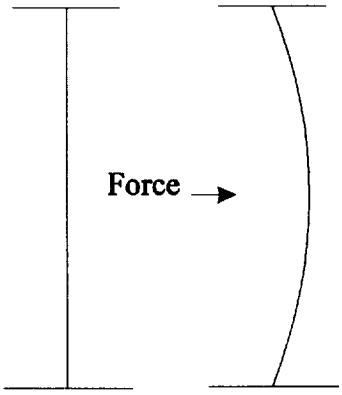

Figure 3.2 Beam Supported at Both Ends

This configuration dramatically reduces the amount of deflection, instability and

vibration that the shaft could experience. Supporting the shaft at both ends will reduce the deflection and vibration in the shaft.(Beer, 1992)

Being able to support the shaft at both ends requires the use of a system of support rods around the main shaft. The rods must be able to rigidly support the top of the shaft, but it must not interfere with the falling payload package and it must not interfere with the visibility of the process.

3.4 Safety

The final consideration in the design of the tower is safety. The purpose of the project is to provide an apparatus that can be taken to various locations, including schools where children would have access to it. The fact that the experiments are based on a large falling object induces a certain amount of risk. Due to this constraint, a shaft is needed to guide the payload in a controlled manner, whereas real drop towers allow the packages to free-fall without any guide. Experiments must also be able to withstand the force of impact without coming apart, or else a piece might travel out and strike an observer. The payload platform and drag shield must be constructed such that no parts would come loose, especially after several drop experiments.

With these criteria in mind, the next step of the project describes the design of the tower.

Chapter 4. Miniature Drop Tower Design

The first stage of the project was to formulate an initial design that would encompass all of the project requirements, as well as, being cost effective and feasible to build.

4.1 Tower

The design centers around a three-quarter inch steel shaft, manufactured by the Thompson Industry. This shaft was originally used in the preliminary miniature tower developed by Dennis Stocker and Howard Pearlman and was deemed acceptable in the new design. The shaft, originally 3.66m (12 ft.), would be cut into two 1.22m (4 ft.) sections and two 0.61m (2 ft.) sections, so that the variable height and the maximum length of an individual piece requirements would be satisfied.

The bottom and the top of the shaft would be supported by means of a large, stable base plate, and a lightweight top that would be simple to lift into position. The base plate would be fitted with four adjustable feet and a bubble level so that the tower could be leveled on inclined surfaces, ensuring that there would always be only a vertical component to the gravity force.

The final major design consideration for the tower was the support structures and several designs were considered. The first design was to be a system of four support rods, positioned in the corners of the base plate, which would be ideal because it would provide support equally from all four directions. This idea was quickly found to be unacceptable because it would require a great deal of materials and would be difficult to assemble. In addition, there would be several individual pieces upon disassembly, reducing the portability of the entire structure and increasing the weight.

The next method considered was a triangular configuration with three support rods. The major problem with this method, is that the steel shaft would be in the center of the support structure, which would hamper the visibility of the experimental package in

Chapter 4. Miniature Drop Tower Design

The first stage of the project was to formulate an initial design that would encompass all of the project requirements, as well as, being cost effective and feasible to build.

4.1 Tower

The design centers around a three-quarter inch steel shaft, manufactured by the Thompson Industry. This shaft was originally used in the preliminary miniature tower developed by Dennis Stocker and Howard Pearlman and was deemed acceptable in the new design. The shaft, originally 3.66m (12 ft.), would be cut into two 1.22m (4 ft.) sections and two 0.61m (2 ft.) sections, so that the variable height and the maximum length of an individual piece requirements would be satisfied.

The bottom and the top of the shaft would be supported by means of a large, stable base plate, and a lightweight top that would be simple to lift into position. The base plate would be fitted with four adjustable feet and a bubble level so that the tower could be leveled on inclined surfaces, ensuring that there would always be only a vertical component to the gravity force.

The final major design consideration for the tower was the support structures and several designs were considered. The first design was to be a system of four support rods, positioned in the corners of the base plate, which would be ideal because it would provide support equally from all four directions. This idea was quickly found to be unacceptable because it would require a great deal of materials and would be difficult to assemble. In addition, there would be several individual pieces upon disassembly, reducing the portability of the entire structure and increasing the weight.

The next method considered was a triangular configuration with three support rods. The major problem with this method, is that the steel shaft would be in the center of the support structure, which would hamper the visibility of the experimental package in

motion. Since the project's primary goal is to be a visual demonstration device, it would be unacceptable to obscure the audience view.

Upon the failure of the triangular supports, a two shaft support system was devised where the two support rods would be parallel to one another at the rear of the base plate and the shaft would be at the forward, center portion of the base, as seen in Figure 4.1. This would be another triangular configuration, using the primary steel shaft as one of the structural members, thus reducing the weight and increasing the visibility of the experimental platform.

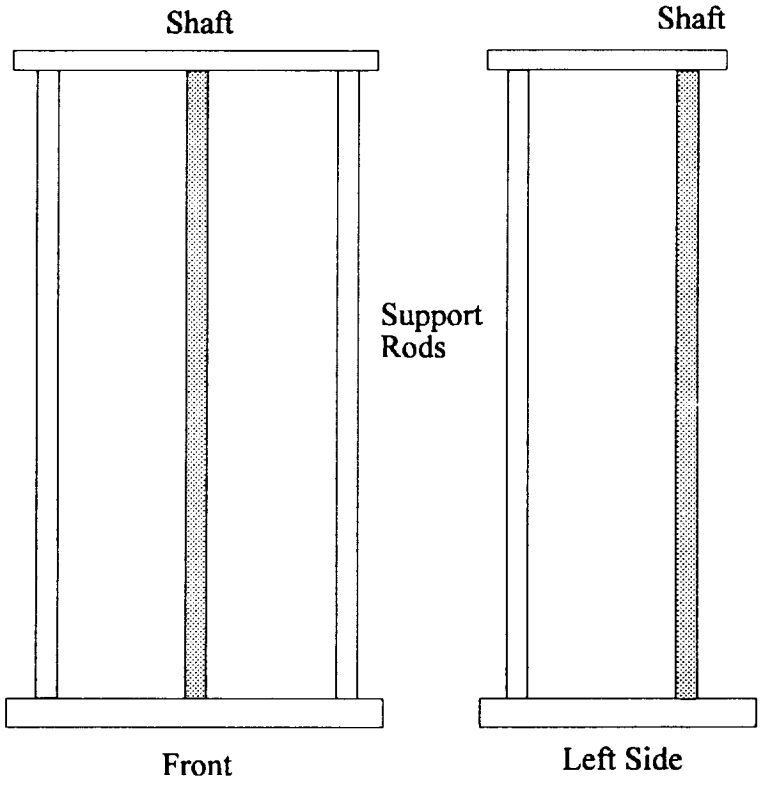

Figure 4.1 Triangular Shaft and Support Rod Configuration

The two support rod configuration would be the most effective method in that it would require a minimal amount of materials and weight, as well as being the simplest to assemble. The rods would have to be supplemented with a system of truss like supports so that the vibration of the steel shaft would be kept to a minimum.

4.2 Operation

A method was needed to raise and subsequently release the payload platform to the top of the tower, while the operator was standing on the ground. The device would have to be simple and yet induce minimal side forces when the package was released. A pulley mounted to the top plate, with one end of the rope attached to the rear of the experimental platform, close to the shaft, was chosen for this purpose. The pulley would be mounted directly above the location where the rope attaches to the platform, inducing minimal side forces when the platform was raised. The pulley will provide some amount of friction upon the system, but since the operator simply has to let go of the rope to commence the drop, there would be little residual force remaining in the rope to induce drag. The materials and assembly for this release mechanism are minimal, the pulley is pre-mounted in the top plate so assembly is simply the rope being connected to the platform and run through the pulley. A three inch diameter, plastic, ball-bearing pulley was used that would be of negligible weight.

4.3 Experimental Platform

The next step was to design an platform that would house the experiments and camera to record low gravity experiments. In addition to the experimental platform, a drag shield had to be devised that would demonstrate the effects and elimination of air drag upon a free fall experiment. It was decided that the experimental platform would be, simply, a rectangular piece that would have the camera and experiment attached in the front and two Thompson sleeve bearings in the rear, represented in Figure 4.2.

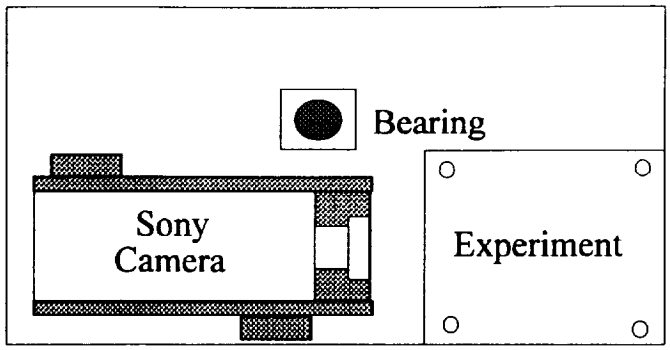

Figure 4.2 Basic Experimental Platform Design

The experiment and the camera would be positioned in the front to enhance visibility and understanding of the demonstration. The sleeve bearings would ride the shaft and be positioned on the top and the bottom of the plate to ensure that it fell vertically and that there would be no disturbances due to the plate wobbling on the shaft. The use of two bearings would increase the drag as the package fell, but, the additional stability would ensure that fluids, and other sensitive experiments, would not be effected.

4.4 Drag Shield

The drag shield was designed as an integral part of the experimental platform. Tabs would be secured to the top of the shield, so as the experimental platform was lifted, it would catch the tabs and raise the shield. Once the platform was released, pressure upon the tabs would be eliminated and it would be able to free fall within the shield. The shield was designed so that it would be about an inch larger than the actual rectangular platform on all sides so that if the platform were to rotate around the shaft during the drop, it would not strike the shield. The shield walls would be constructed from plexi-glass so that the visibility of the experiments would not be hindered within the shield. The shield was also designed with a single Thompson bearing to guide it down the shaft. A sketch of the Drag Shield is provided in Figure 4.3.

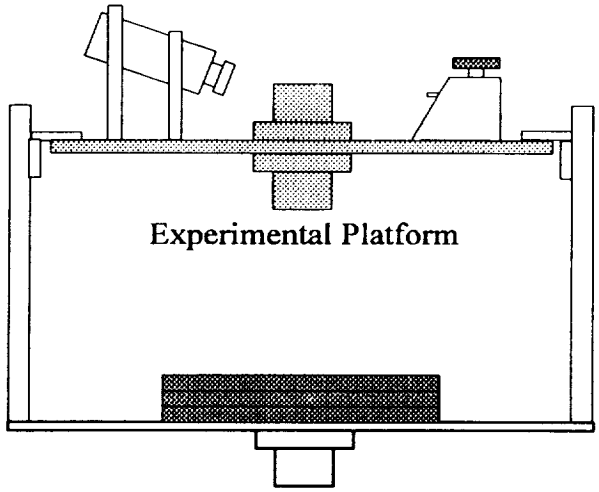

Figure 4.3 Drag Shield and Experimental Platform

Deceleration of the experimental package (shield and platform) would be accomplished through use of foam padding. Padding is used at the bottom of the tower to decelerate the shield upon impact and the shield will also be equipped with foam to decelerate the experimental platform.

Chapter 5. Construction

This section describes the different methods and design features that were involved in constructing the tower, experimental platform and drag shield. A detailed description of assembling the drop tower is provided in Appendix G.

5.1 Tower

A sketch of the complete tower is provided in Figure 5.1 and more detailed drawings can be found in Appendix B.

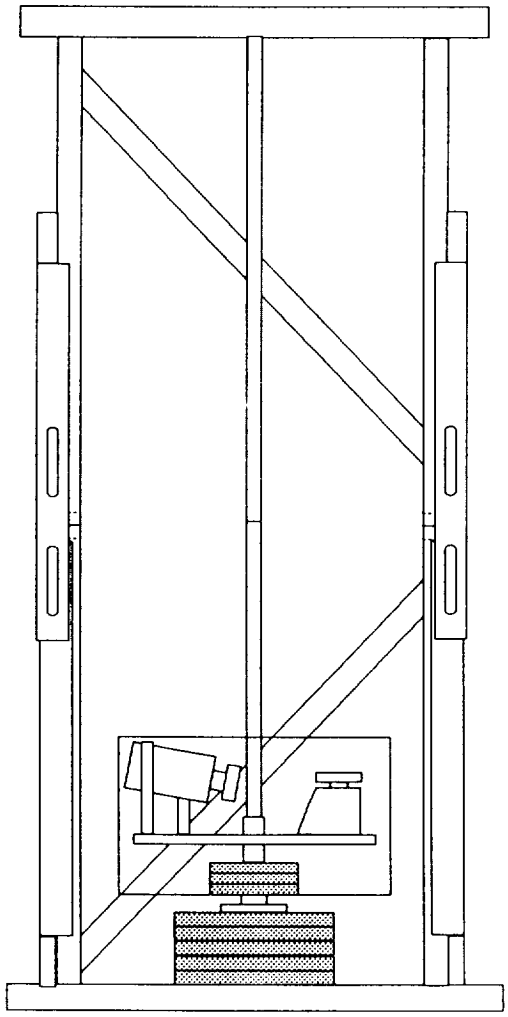

Figure 5.1 Complete Tower Construction

The construction of the tower began with the three-quarter inch solid steel shaft.

The shaft was as a solid piece 3.66m (12 ft.) and was then machined into two 1.22m (4 ft.) segments and two 0.61m (2 ft.) segments. The segments were connected by a 50.8mm (2 in.) 3/8 in.-16 threaded hole tapped into the ends of one segment and a set screw was placed into the other end and tightening the next segment on by turning the shafts. The ends of each segment were also chamfered 3.175mm (1/8 in.) to ensure a fit with minimum disruption to the smoothness of the shafts. The circular tolerance for the shaft and the segment joints was 0.051mm (0.002 in.) The two 1.22m sections are used as the basis for the tower, providing a 2.44m (8 ft.) drop and the other 0.61m segments can then be added to obtain a 3.05m (10 ft.) or 3.66m (12 ft.) height, if desired.

The next step was to construct a base for the shaft, a sketch of which is provided in Figure 5.2. The base needed to be large enough to provide a stable base, and yet be light enough to be easily transported. The choice of base size became a matter of convenience rather than a matter of design. A light weight material that would not flex when the experimental package struck after the fall was needed and half inch aluminum was selected.

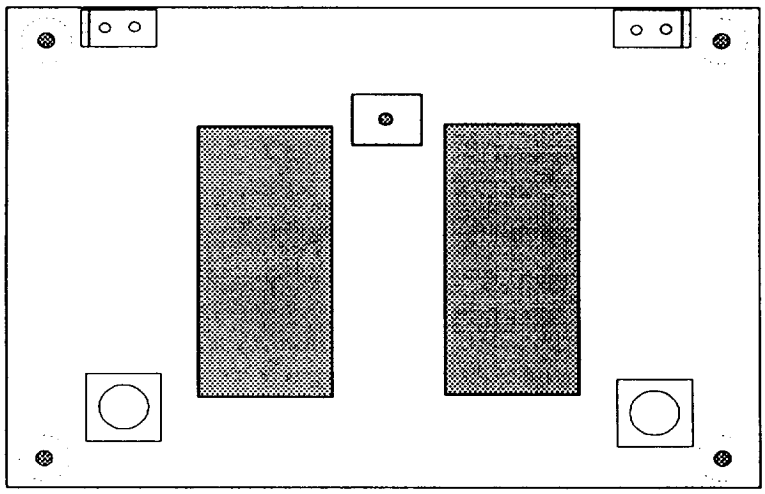

Figure 5.2 Base Plate

Half an inch aluminum would provide the stiffness and rigidity that was needed, but this thickness is not easily machined with standard industry tools. The base was,

therefore, a piece of scrap from another larger project that had access to large pieces of machinery. It was originally planned that the base would be 508mm X 711.2mm (20 in. X 28 in.) and a piece 673.1mm X 546.1mm (26 1/2 in. X 21 1/2 in.) was found and was acceptable. This piece, however, weighed over 9.98kg (22 lbs.) and would be difficult to carry and put in a car. Two holes 368.3mm X 152.4mm (14 1/2 in. X 6 in.) were cut into the piece to reduce the weight to approximately 6.35kg (14 lbs).

The support rods necessary to support the top had to be made from material that would make the rods stiff, but light. Due to the abundance and low cost, it was decided that steel conduit would be used. The conduit had an outside diameter of 23.81mm (15/16 in.) and an inside diameter of 20.64mm (13/16 in.). To be able to quickly assemble and disassemble the conduit sections, the bottoms of the tubes were swaged so that they would fit into the top of the other segment, similar to the construction of common tent poles. A 76.2mm (3 in.) aluminum peg was machined that would slide into the unswaged bottom conduit section, which was then mounted to the base plate. This process is demonstrated in Figure 5.3.

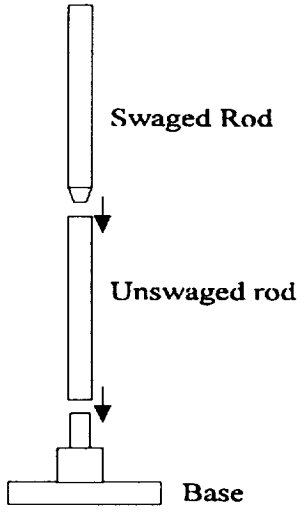

Figure 5.3 Support Rod Assembly

Employing this method allowed the assembly of two variable length support rods without the use of any hardware or tools to assemble. The only item that was used to assemble the

rods were pins that could be slid into pre-drilled holes. The holes were drilled at exact lengths so that when assembled the support rods would be the exact height of the tower shaft.

The top of the tower is constructed from 3.175mm (1/8 in.) of aluminum in the shape of a trapezoid with the small end towards the front of the tower. This shape was chosen because it would support all three shafts with minimal material. The trapezoidal shape was also essential due to the fact that the camera and the experiments were several inches tall and when the experimental platform was raised, they would strike the top plate, reducing drop distance. By cutting the corners from the front of the top plate allowed the camera and experiments to rise above the top and maximize the drop distance and low gravity time. A sketch of the top plate is provided in Figure 5.4.

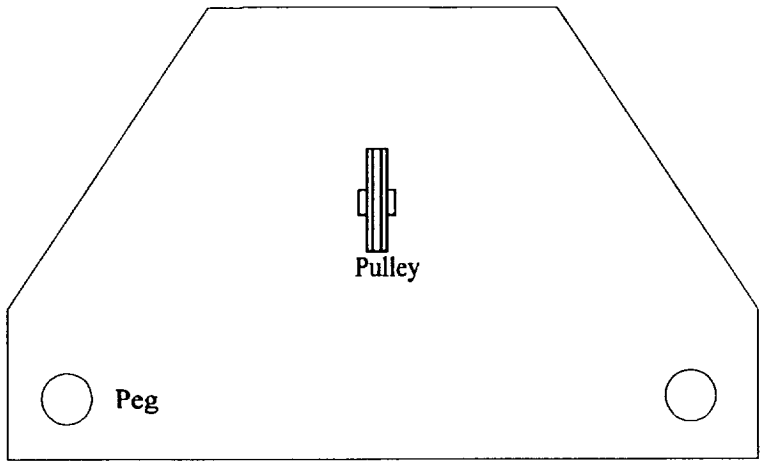

Figure 5.4 Top Plate and Pulley

The next problem that was encountered was that the support rods had a great deal of flex and motion or low torsional stiffness. This was due to a combination of factors. The first was the extended length of the bars, at over 2.44m, there was a significant amount of bending when a side load was applied. Another reason for the instability was the swage fittings, which were snug, but it was not possible to make them within exact tolerances because if they were too tight, it would be difficult to pull them apart and slide

them together. It became obvious that a method of bracing the support rods was needed and several options and geometries were considered.

The first material used was one inch wide strips of 3.175mm (1/8 in.) aluminum, which provided adequate support while in tension, but would buckle easily while in compression. The next material that was used to alleviate this problem was 25.4mm X 25.4mm (1 in. X 1 in.) aluminum angle, as seen in Figure 5.5.

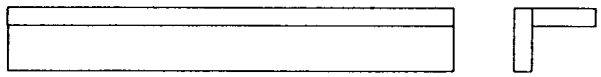

Figure 5.5 Angle Bracket

Since there were two structural segments joined at a right angle, there was no buckling when a compressive load was applied. The angle was used in a criss-cross pattern between the two support rods to eliminate side displacement, seen in the front view of Figure 5.6. Another section was mounted in the front of the base and connected to the support rods to eliminate forward displacement, represented in the side view of Figure 5.6. The angle in the front of the base had to be constructed in two pieces so that they would be long enough to stretch from the front of the base to above the swage fittings on the rods and still not exceed the maximum length requirement.

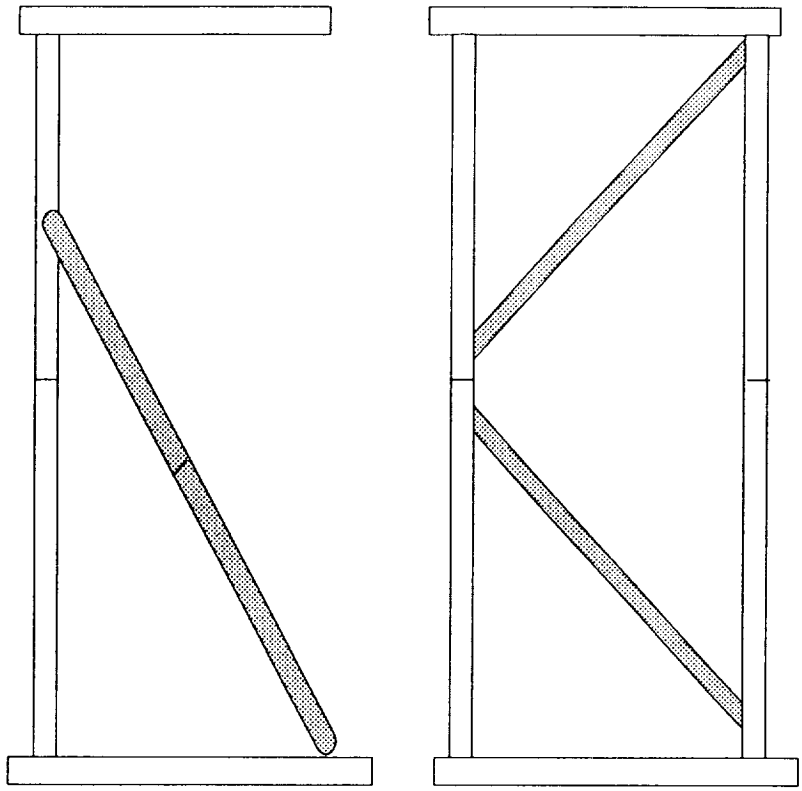

Figure 5.6 Front and Side View of the Angle Supports on the Tower

5.2 Experimental Platform

The experimental platform will have the camera and experiments mounted upon it and will slide down the steel shaft during the experiment. A sketch of the platform is provided in Figure 5.7. The platform was constructed using a 381mm X 254mm (15 in. X 10 in.) piece of 3.175mm (1/8 in.) aluminum, with the center of the bearing located 76.2mm (3 in.) from the back and in the center of the plate. The bearing would have been optimal in the exact center of the plate because it would not produce a bending moment upon the shaft while it was in the air. This would not be practical, however, for the plate would have to be significantly larger and counterweights would need to be incorporated. This entire process would add weight, complications and additional components to the system, which would be detrimental to the project goals.

The plate was the basis for the camera mount and the experiment packages.

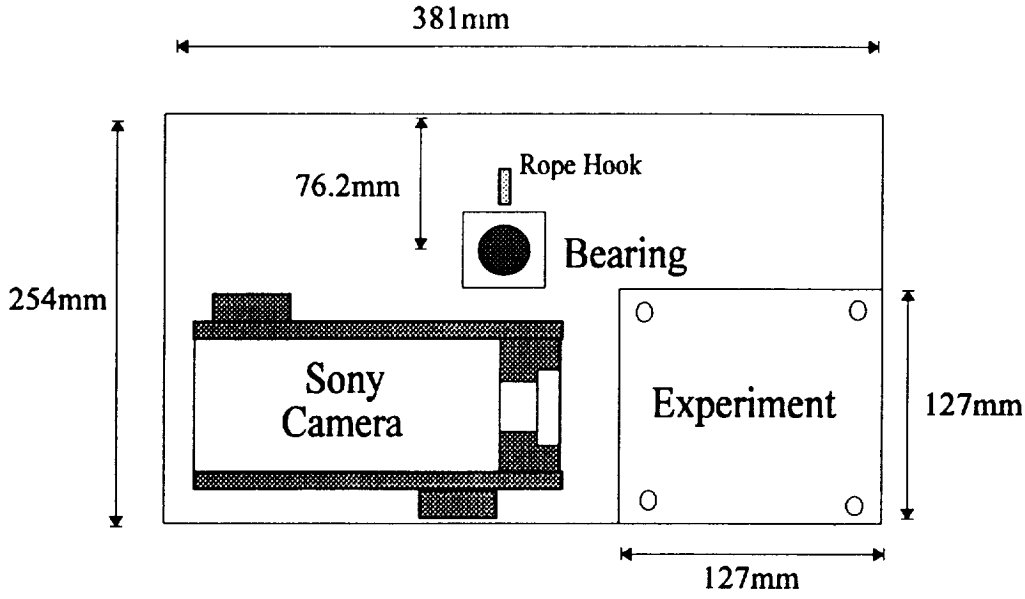

Figure 5.7 Configuration of Experimental Payload

The area labeled experiments is where all of the experiments would be mounted. For convenience and the ability to be changed quickly, all of the experiments were mounted to a standard 127mm X 127mm (5 in. X 5 in.) aluminum templates. Four bolts were mounted upwards on the experimental plate and the templates fit onto the bolts and simply had to be tightened down with wing nuts, requiring no tools.

In this configuration, there is only provision for one solid state video camera. The initial design called for the use of two cameras so that several aspects of the experiments could be captured. Since only one camera was available, a method had to be devised to be able to adjust the single camera into a variety of positions to witness experiments at several angles. The camera was mounted within a padded tray of 3.175mm (1/8 in.) aluminum with two blocks mounted on the outside that were threaded so a 1/4-20 bolt could be screwed in. Two "L" shaped brackets were also constructed. The brackets were milled out along the center so that it would be possible for the bolts to pass through and then be tightened into the camera mount. The brackets were milled on the sides, as well

as the bottom so that the camera could be moved horizontally and vertically. A possible configuration of the "L" brackets and the camera tray can be seen in Figure 5.8.

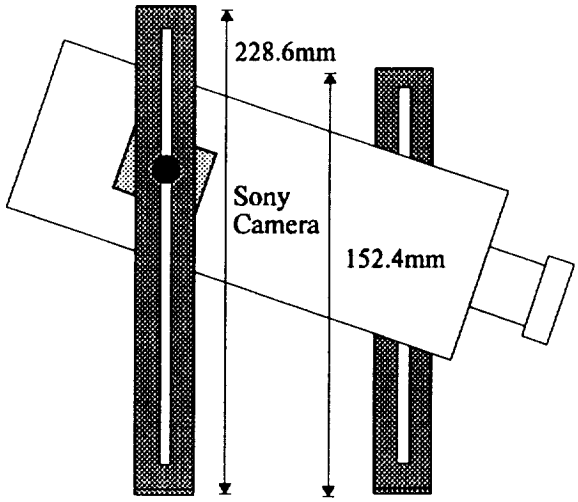

Figure 5.8 Side view of Camera Mount

The camera mount brackets are of different height because to obtain angle views, it was necessary to raise the rear of the tray higher than the front. The screws holding the camera in place were socket type so that the only tool needed to adjust the camera was a small 6mm socket key.

5.3 Drag Shield

To completely emulate a large drop tower, a method of reducing air drag was needed. A drag shield would be included in the development of miniature tower even though air drag over the 2.44m (8 ft.) distance was negligible. The effects of gravity (G) and air drag (AR), upon the system in the miniature tower are demonstrated in Figure 5.9.

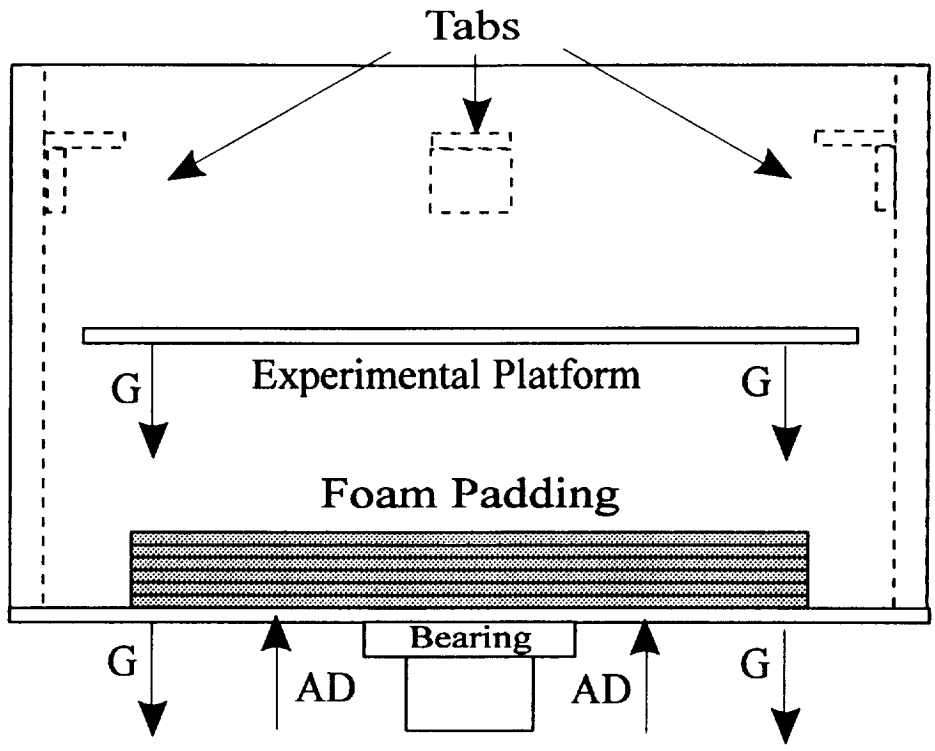

Figure 5.9 Drag Shield and Effects of Gravity and Air Drag

During the low gravity acceleration measurements, the distance the experimental platform gained upon the drag shield was measured and found to be approximately one half inch which would be insignificant for the experiments that were being performed. The drag shield was created to satisfy the education and demonstration requirements of the tower. Both towers at NASA use some type of approach, whether it be a drag shield or evacuating the drop tower, to reduce the air drag upon the payloads. The drag shield constructed for the miniature tower is more of an example for explaining the concept and uses for a drag shield rather than an integral part of the experiments. The base of the shield was constructed from a 431.8mm X 304.8mm (17 in. X 12 in.) piece of 1.59mm (1/16 in.) aluminum. To this were mounted 3.175mm (1/8 in.) plexi-glass sides that were 254mm (10 in.) tall. The side that faced the rear of the camera had to have a section cut out to allow the power and video cables to have a clear access to the ports on the camera. The shield was not connected to the experimental plate so that the two could fall

independently. Three pieces of aluminum angle were mounted to the sides of the shield 25.4mm (1 in.) from the top, thus when the experiment plate was pulled up, it would catch the shield and draw it up as well. A demonstration of the platform and the shield being raised together is demonstrated in Figure 5.10.

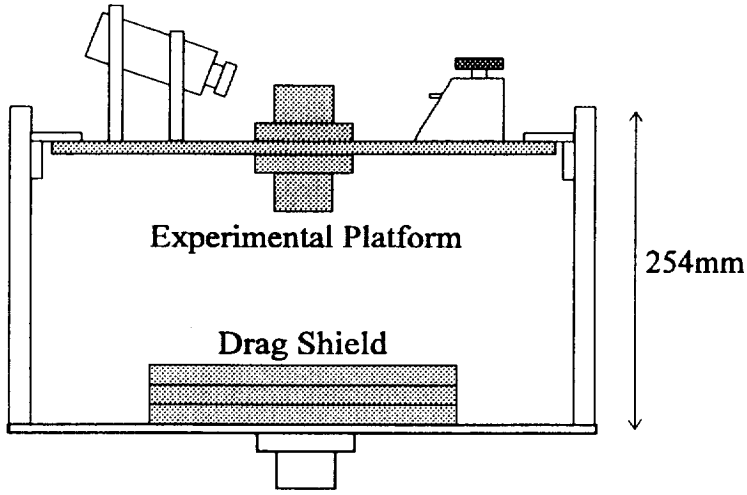

Figure 5.10 Drag Shield and Experimental Payload

This method required no modification to the release mechanism and still allowed both pieces to drop freely. Other features of the shield included a hinged front that could open so the experiments and camera could be changed quickly, as well as, 101.6mm (4 in.) of temper foam used to decelerate the experiment package.

Chapter 6. Acceleration and Deceleration

The development of the demonstration tower is based on the assumption that free-fall will create a low gravity environment. This can be confirmed through the use of simple measurements of time and distance. The tower was created to simulate an environment where the acceleration of the experimental platform is close to that of gravity. In an ideal free-fall, the acceleration of objects will equal the acceleration of gravity, but factors, such as friction and air drag, will slow the objects. It will be necessary to determine the acceleration of the experimental payload to find the gravity level during the free-fall portion of the drop.

The first derivative of distance is velocity and the second derivative is acceleration. Knowing this, if distance measurements and corresponding time measurements can be taken, the acceleration can be found. The equations are as follows:

$$V = \frac{\Delta D}{\Delta t} \tag{6.1}$$

and

$$a = \frac{\Delta V}{\Delta t} \tag{6.2}$$

Where D is the distance traveled, V is the velocity of the experimental platform, and t is the time.

It was possible to measure distance and corresponding time using the camera mounted on the drop rig and a counter that would provide an on-screen display while the camera is recording. An indicator was mounted on the rig in the field of view of the camera and a tape measure was secured to a bar outside of the tower. The camera was focused so that the indicator would correspond to a reading on the tape measure and as the camera and indicator fell, the reading on the tape measure would change. During the period of the fall, a frame counting timer was running; with the speed of the camera running at thirty frames per second.

Using these two indicators, drops were conducted, recorded and then replayed so that measurements could be taken and recorded. The tests were run using both the 2.44m (8 ft.) version and the 3.05m (10 ft.) version so that a larger number of points could be collected. Data was compiled through the use of the Microsoft Excel spreadsheet package and values for the velocity and acceleration at selected times were computed. The entire collection of data can be referenced in Appendix D. The average of the accelerations for the 3.05m and the 2.44m heights were found to be approximately 8.87 m/sec^2 (29.1 ft/sec^2). This means that the acceleration realized by the dropped package is; 1.0 - (8.87/9.81)g = 0.096g, i.e. 9.6% of normal gravity.

Another measurement that was needed to determine the basic characteristics of the tower was to determine the levels of deceleration upon impact of the experimental skid. The impact measurements were found through the use of Piezotronics Quartz, Low-Impedance, Voltage-Mode Accelerometer. Exact specifications and description of the accelerometer can be found in Appendix E. The device was mounted to the experimental platform and then connected to a laptop computer that would record data as the drop occurred. The program that would convert the voltages sent by the accelerometer into an actual list of numbers was written by Andy Jenkins and could easily be imported into a spreadsheet to analyze the data. The instrument is not extremely sensitive at low g readings and could not be used to measure the low gravity portion of the drop with any accuracy.(Jenkins, 1993) It is capable of reading the high g levels upon impact. The program provides over ten thousand points of data and would not be worthwhile to reproduce here, but plots of the data can be found in Appendix F.

Upon analysis, it was found that the maximum deceleration level was approximately 100 times that of gravitational. This acceleration results in a large force exerted on the drop package, but it only acts for a period of approximately one

millisecond, so it is still safe for the optical equipment supported upon the experimental platform. The phenomena of the initial high g level spike is common in the drop towers and is an acceptable result, because it damps out extremely rapidly.

Chapter 7. Experiments

7.1 Introduction

The experiments provided with the Miniature Demonstration Drop Tower are designed to highlight a wide variety of low-g behavior. The Experiments designed include mechanical, hydrodynamic, and thermal physical concepts. In this way much of the basics of what the people in the microgravity division at NASA work with can be seen. The experiments are themselves simple, but their effectiveness lies in that they can visually demonstrate low-g effects on physical phenomena.

Because of the limited size of the tower, the size and weight of the experiments had also to be limited, but at the same time be effective. The experiments had to be small enough to function on the payload platform and they also have to illustrate low-gravity in the small time allotted in the drop. From these basic constrictions, design parameters for the experiments were developed. The experiments have to fit and be affixed to a 133 mm X 133 mm (5.25"x5.25"), 3.175 mm (1/8") thick aluminum plate, that will be attached to the payload platform. They must be able to withstand impact and be no more than 2.27 kg (5 lbs.). This will insure that the setup remains portable.

As part of this project at NASA Lewis, there were a total of 11 experiments designed and performed. They include: the Pendulum, the Newton's cradle, the paper burning, the candle burning (2 orientations), the liquid reorientation, the magnetism/weight, the scale, the coriolis, the buoyant force, and the tension force experiments. The rest of this chapter will be devoted to describing the theoretical basis of each experiment.

7.2 Basic Premise

All the experiments demonstrate phenomena which are in some way affected by

gravity. The equations that model the experiments therefore contain a gravitational term within them. This term always approaches zero when the payload is falling.

In the explanations that follow, many of the equations may relate to each other or seem too similar, but these kind of experiments were chosen because of their simplicity and commonalty in the world. This way when a demonstration is being performed for a group, the visual effects dramatically display the simplest of concepts in physics. The following table concisely states the experiments.

Table 1. - Description of Experimental Phenomena Demonstrated in Low-G

Experiment Name	Illustrated Physical Phenomena (low-g)	Future Improvement
Pendulum	Change in period of pendulum.	Stronger twine is needed for repeated drops
Buoyancy	Reduced buoyancy force on bubbles	
Scale/weight	Weightlessness of matter in low - g	
Tension	Change in tension forces due to lower force of opposing weight	
Magnetism	Illustration of magnetic force on object at different weights.	A stronger shaft is required .
Newton's Cradle	Change in periods of a double pendulum	Stronger twine is also needed for repeated drops
Liquid Orientation	Change in a meniscus size and curvature	
Candle Burning	Illustration of flame shape due to reduced air buoyancy	
Paper Burning	Demonstrates flame spread with reduced air buoyancy	
Coriolis	Illustrates coriolis effects on a weight in reduced gravity	A more suitable motor should be obtained to create coriolis effect

7.3 The Pendulum.

A pendulum was constructed using fishing twine a ball bearing (containing a hook), 2 pieces of 3.175mm (1/8 in.) tubing and four 50.8mm X 25.4mm X 38.1mm thick (2 in. X 1 in. X 1.5in.)aluminum blocks. As seen in Appendix A, the tubing was bent ninety degrees in two places and the ends were screwed into blocks. The blocks themselves had 2 holes on one side and one other hole on the other drilled and tapped. The tubes were secured to the blocks which in turn were secured to the plate. The fishing twine holding the ball bearing was finally epoxied to the two tubes.

The pendulum was manufactured in a manner, so that the motion of the pendulum was orthogonal to the line of sight of the camera.

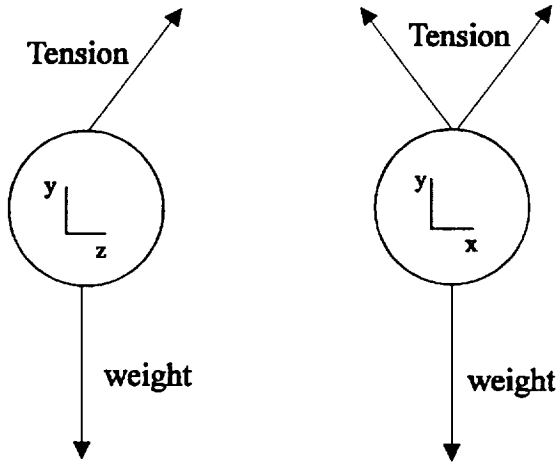

Figure 7.1 Pendulum

As seen in Figure 7.1., the tension in the fishing twine is equal and opposite in the x-direction, providing no net force in a sideways manner. The only forces that affect the motion are in the y & z directions. The gravitational force and the tension in the twine are the only forces affecting the ball bearing.

From the summation of forces in the y-direction, where l is the length of the chord, an equation of motion for the pendulum can be derived:

$$I\omega = mgl(\sin\theta) \qquad (7.1)$$

Solving for the angular velocity and substituting into the relationship T=2□/w, where T is the period, the following equation can be determined.

$$T = 2\pi\sqrt{\frac{l}{g}} \qquad (7.2)$$

In microgravity the g approaches zero, therefore the period goes to infinity. Physically, the pendulum slowly comes to rest. Since the g-levels were measured to be .1g for the tower the period was approximately increased by a factor of 30. In the experimental drop that was conducted, a dramatic increase in period was observed. The ball continued to ascend past the original peak, confirming the theory.

7.4 The Buoyancy Force experiment.

From basic physics, we know that the buoyancy force on an object is equal to the weight of the water the object displaces. To the average high school student this might not be apparent. By showing that in the absence of gravity there is no buoyancy force, a direct correlation from visual observation of the two forces can be made.

In this buoyancy experiment a bubble cylinder was utilized, which can be purchased at any "Spencer's" stores. This device has the capability of releasing many bubbles of air as well as globules of a liquid into the water contained within it. This made the bubble cylinder an ideal choice for illustrating buoyancy in low-g.

As seen in Fig 7.2, the bubble cylinder was affixed to bar with bottle clamps, which was connected by a screw to a U shaped bracket. In this way, the bubble cylinder can be turned over by turning the screw, initiating the experiment with out it ever being removed from the support.

In the experiment there are three forces acting on any given bubble: the buoyancy force, the bubbles weight, and the liquid's viscosity. The buoyancy force, is directly proportional to the g-levels. We can see this in the equation modeling the force:

$$Fb = (M_{water})(g) = (Density_{water})(Volume_{submerged})(g) \qquad (7.3)$$

The bubble cylinder releases air bubbles from the bottom of a cylinder. Since the buoyant force is greater than the weight of the bubbles, the bubbles rise. This can be seen in Appendix A. In the absence of gravity, the buoyant force becomes very small, as well as the weight of the bubble. Viscous effects slow down the bubble and it eventually becomes stationary; thus dramatically illustrating the theory to the observer.

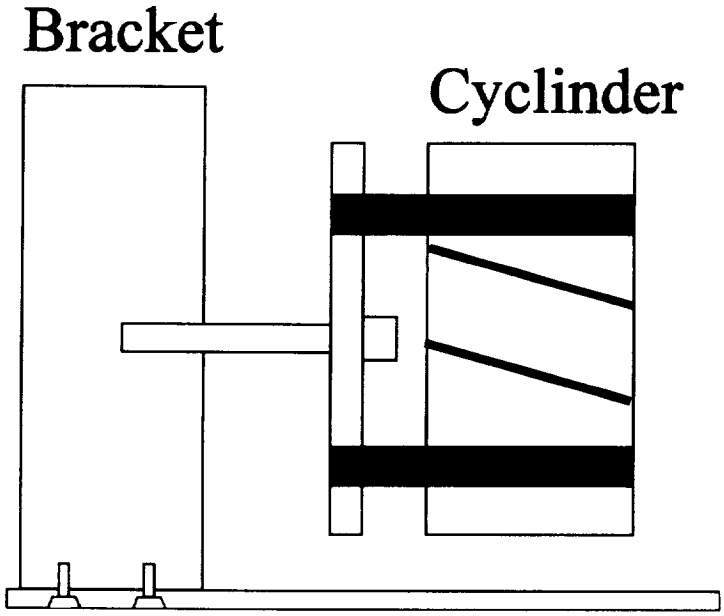

Figure 7.2 Buoyancy

7.5 The Scale/Weight.

One of the most simple ways of demonstrating the low-g effects on a body is by measuring its weight, while it is stationary and during a drop. According to Newton's equation F = m * a, the force (weight) being exerted by an object is directly proportional to the acceleration of gravity. Therefore, while an object is in freefall the scale, measuring the objects weight should read approximately zero.

A small spring scale was purchased and a 114g (4 oz.) weight was affixed to the scale by means of two small screws. A reading of the objects weight, therefore, could always be taken. As seen in Figure 7.3 and in Appendix A, the scale was secured to a plate by means of a bent bar attached to the plate that securely hugged the scale.

The scale was dropped and in fact did read zero, demonstrating that the object was indeed weightless.

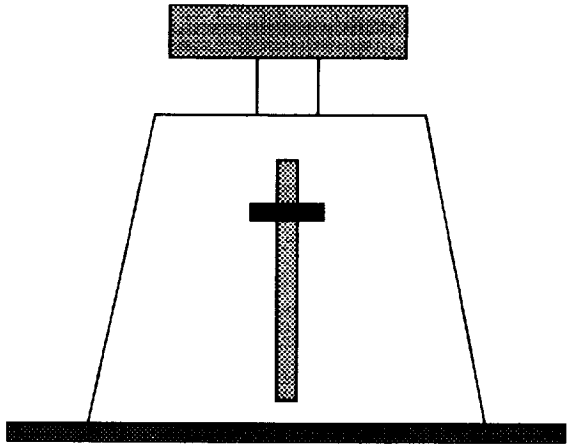

Figure 7.3 Scale

7.6 The Tension Experiment.

When a rubber band is in tension, it is being caused by outside forces acting on it. This tension experiment is similar to the scale experiment in that a weight is used as the primary force to cause tension.

The tension experiment was constructed using two screws set in two blocks that were affixed to a plate. The rubber band was fed through two tiny holes and a knot was tied on either end. the rubber band itself was put slightly in tension between the two poles. A weight was affixed to the rubber band at the center and let go, creating a greater tension and causing the rubber band to sag as seen in Appendix A.

The forces in the x-direction are equal and opposite and are constant. The forces in the y-direction are the weight of the object and the y component of the tension in the rubber band. This is illustrated in Fig. 7.4.

$$2T\sin\theta = mg \tag{7.4}$$

As previously mentioned, once the drop begins the gravitational constant will approach closely to zero. The result is that the tension in the y direction will also approach zero. The visual effect is that the mass appears to be hovering.

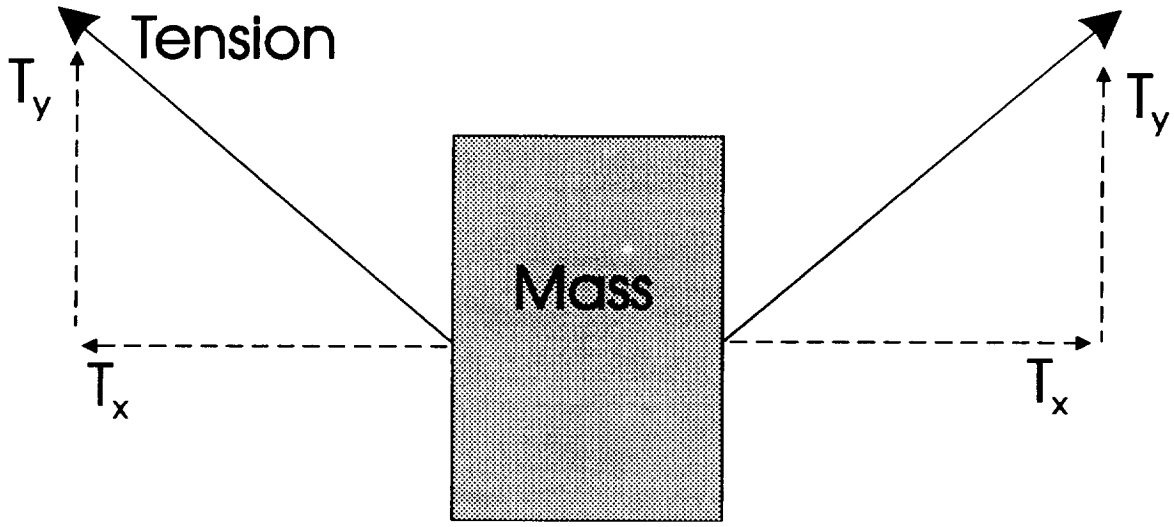

Figure 7.4 Tension

7.7 The Magnetism Experiment.

This magnet experiment is different from the other experiments in that the magnetic force of repulsion is not a function of the amount of gravity, as we have seen in the tension and buoyancy experiments.

The experiment was constructed using two donut shaped magnets that are held in place by a rod attached to the plate as seen in Fig 7.5. Temper foam is used in between the two magnets to reduce the force on the magnets at impact.

The sum of the forces in the vertical direction include the force of the magnetic field and the weight of the magnet.

$$F_m = mg \tag{7.5}$$

Again, during the drop, the g levels are reduced and the only force left is the magnetic force. The result is that the top magnet is accelerated upward. A stopper was added to the end of the rod in order to stop the magnet from launching. This experiment demonstrates visually the idea of two separate forces acting on an object.

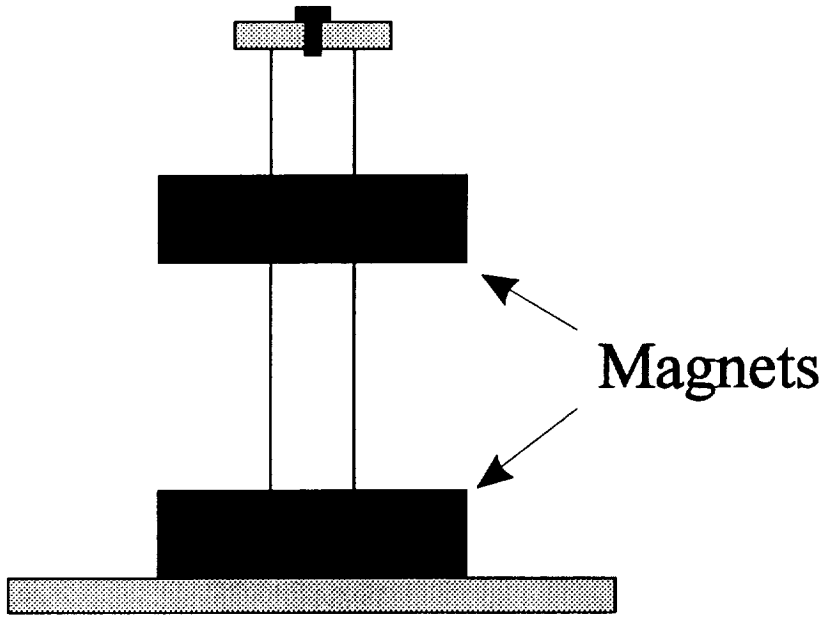

Figure 7.5 Magnets

7.8 Newton's Cradle Experiment.

The Newton's cradle experiment is very similar to the pendulum experiment. The cradle is composed of two pendulums, in which two balls strike one another transferring their momentum to the each other. This experiment serves only to reiterate what the first pendulum experiment does, except that it shows that two pendulums, with the same period, will be affected by the lower g in exactly the same way. The experiment serves as a more interesting way for the observer to see the original pendulum experiment.

The construction itself is the same as the single pendulum described previously except that a second pendulum is added. To get the pendulums into stable periods the fishing twine lengths are the exactly the same and the ball bearings just touch one another. This is shown in figure 7.6 and Appendix A.

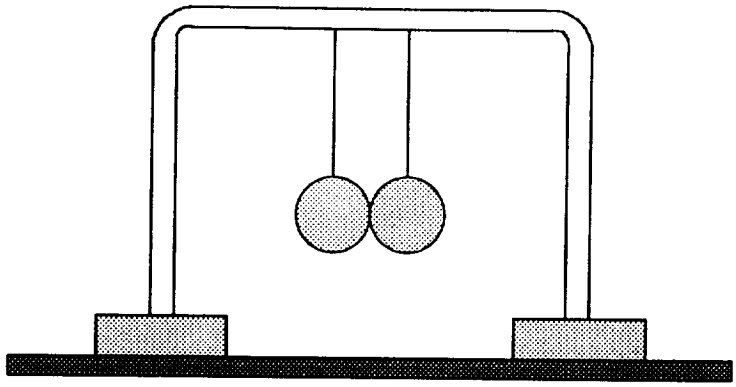

Figure 7.6 Newton's Cradle

7.9 The Liquid Reorientation Experiment.

How fluids behave in microgravity is essential to the flights of space aircraft. Surface tension is a property to all fluids. It binds the fluid together and is the result from all the attractive forces of the molecules in that fluid. This force can hold a drop of water suspended on a rod and limits the size of the drop that may be held. Because of the low gravity of orbit, surface tension in liquids cause interesting effects.

In a clean tube, at the interface between water and air, a meniscus forms because the weight of the water is pushing downward, while the surface tension of the water causes the sides to rise, forming the meniscus. This can be seen in Figure 7.7 This can be modeled in the following equation.

$$\sigma\pi D - \rho g \frac{\pi D^2}{4} h = 0 \qquad (7.6)$$

If sigma is the surface tension of the water, the height of the meniscus can be found to be.

$$h = \frac{4\sigma}{\rho g D} \tag{7.7}$$

In this experiment, a tube was constructed from Plexiglas and affixed to a plate for the platform. It was then filled half way with silicon oil (100cs). A definable meniscus was observed. Silicon oil was chosen, because it was a more viscous solution and because of this, the fluid did not slosh around as much, due to vibrations of the tower.

From the previous equations, if the g-levels were to approach zero the height would begin to approach infinity. In reality this would only occur if the tube siding had almost no friction, which was not accounted in the equation. The meniscus, though, should still show an increase in size due to a reduced weight of the water. The drops done in the Miniature Demonstration Drop Tower confirmed this theory. There was indeed an increase in the meniscus size, although it wasn't as substantial as the equations predicted. Friction, the fact that it was a viscous solution and there was limited fall, all contributed to the smaller actual change in meniscus size.

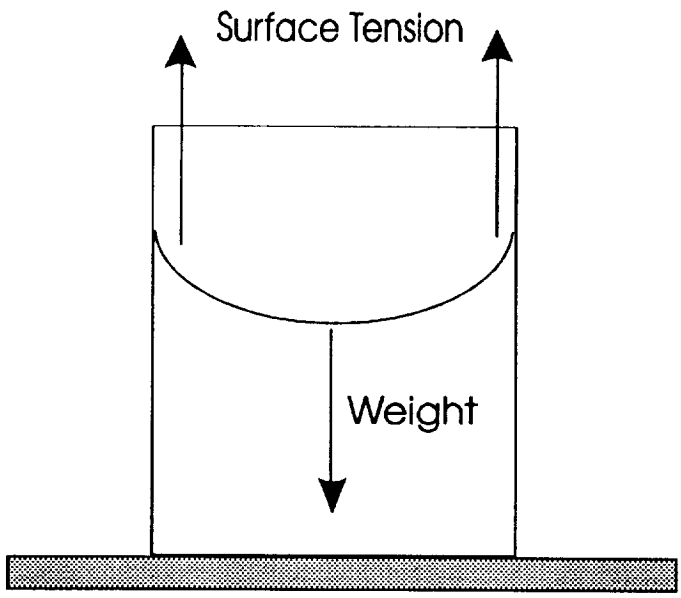

Figure 7.7 Meniscus

7.10 The Candle Burning Experiment.

When one observes a candle flame, one expects to see a tear drop shaped flame pointing upward. This flame shape occurs when the air surrounding the flame is heated. The air becomes more buoyant and rises, the flame then shapes into the tear drop because of this air flow. One can rotate the candle sideways and the effect of buoyancy becomes more pronounced, since the flame is forced to turn upward.

In a low-g environment, the buoyancy of the air, when heated would not change, since the effect of the gravitational force on the density differs from normal g. The change in the density caused by heating is negligible, so there would be no air flow. Since there is no air circulation, one would expect that the flame would burn in a spherical shape, drawing from an evenly disbursed air gradient surrounding the flame.

In the candle burning experiment, two holders were designed to accommodate different orientations. In the first case, the candle stood upright, wedged into a small block that was attached to a plate. In the second case, the candle was attached to the side of a tube, in a horizontal configuration. A Plexiglas tube of diameter four inches and a height of a foot was secured to the plate and encased the candle. This was done to eliminate any air circulation that might be in the environment and that would affect the experiment. This can be seen in figure 7.8.

In the results of the experiments, it was observed that the flame did assume a spherical shape. The two configurations looked very similar in shape, in that if one would rotate a picture of the upright one and compare it with the sideways candle, the flame shape would look the same. This is especially interesting in that we observe a flame that doesn't know which way is up.

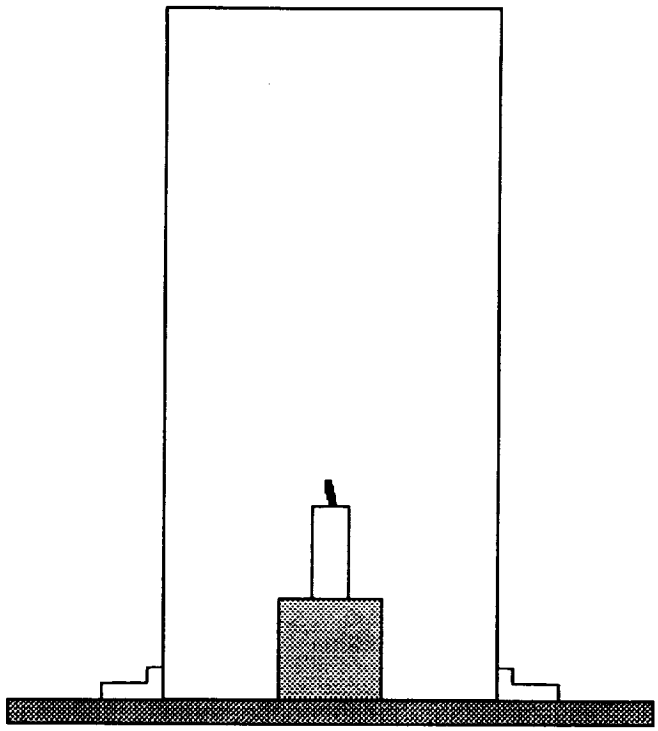

Figure 7.8 Candle Burning

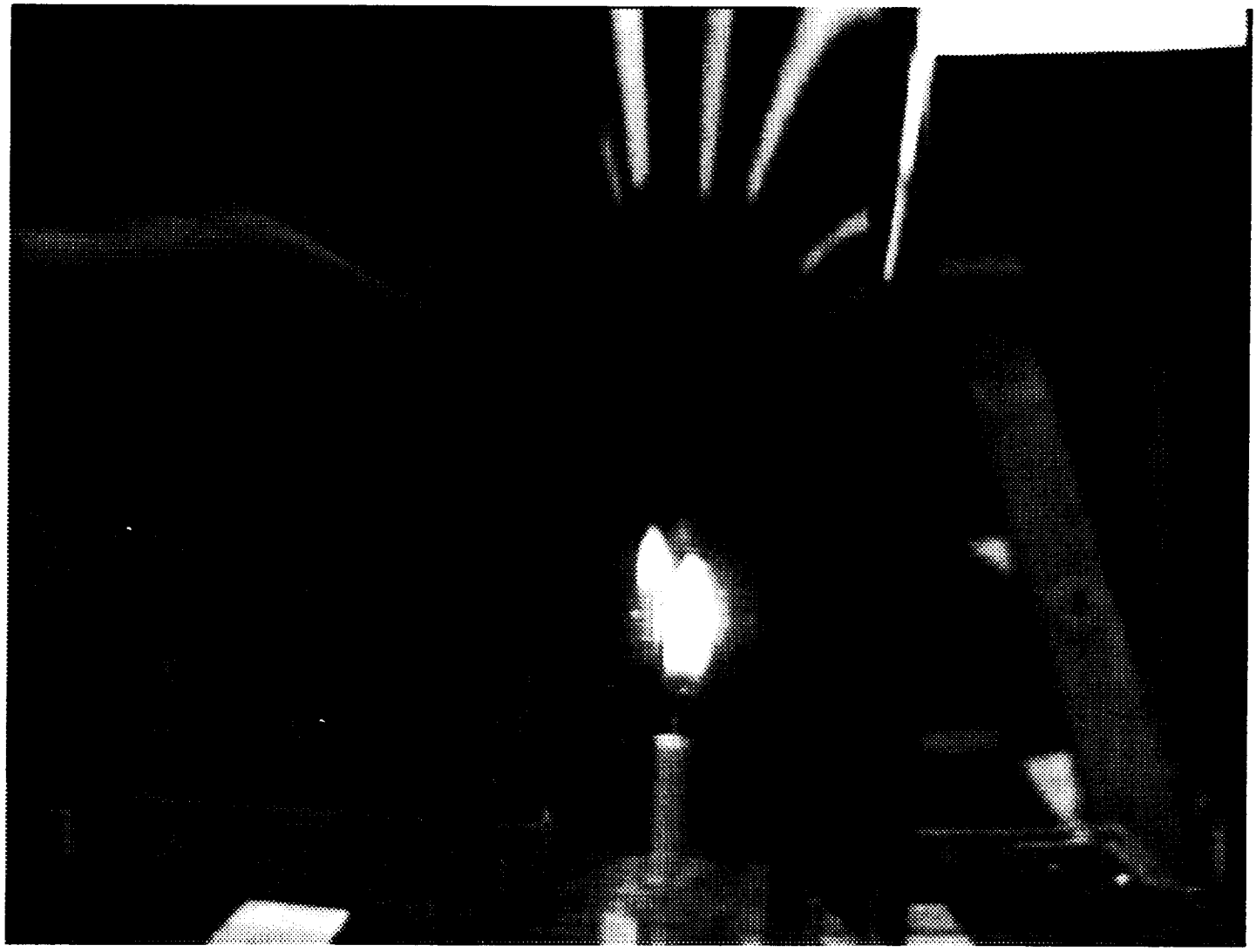

Candle Experiment : Normal - g (Figure 7.8a)

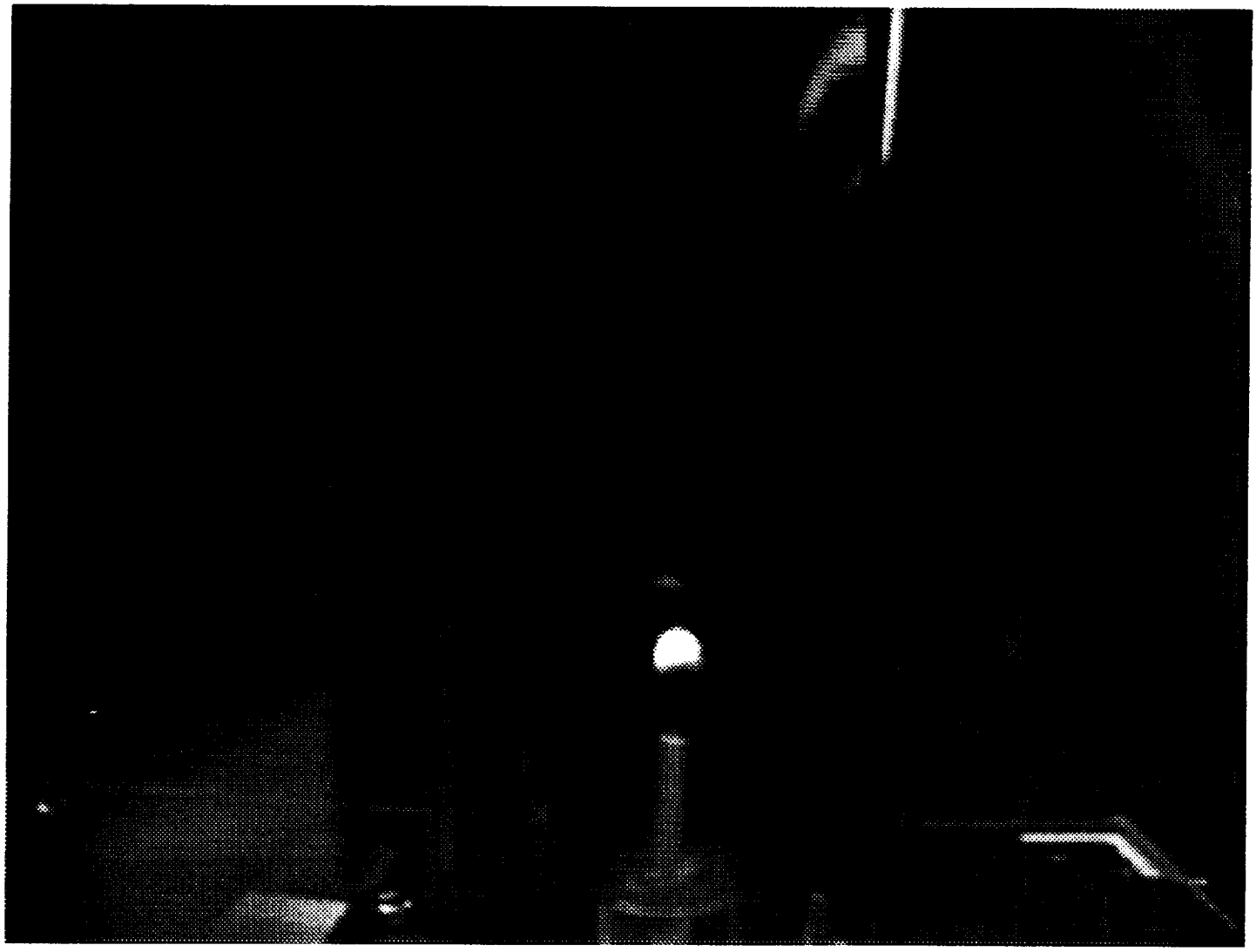

Candle Experiment : Low - g (Figure 7.8b)

7.11 The Paper Burning Experiment.

The paper burning experiment, similar to the candle burning experiment, illustrates the shape and propagation of a flame. In normal -g if one ignites a flame at a paper's center, the flame would burn the paper similar in fashion as a candle's shape. The flame propagates upward in a plumb shape, then outward, and finally downward. This again is due to the convection of air when its buoyancy changes due to the rise in temperature.

In the experiment, a very thin sheet of paper was affixed to a stand, provided by David Urban of Sverdrup Technology, that stood affixed within and to a Plexiglas tube, 304.8mm (12 in.) tall and 101.6mm (4 in.) in diameter. This is illustrated in Fig. 7.9. The paper was ignited by means of kanthal which was heated when current was passed through it. This was done in normal g and low g.

Unlike the normal g burn configuration, the low g flame propagates radially. This, again, similar to the candle, was due to the fact that air in the tube did not convect upward due to a difference in buoyancy between the warmer and cooler air.

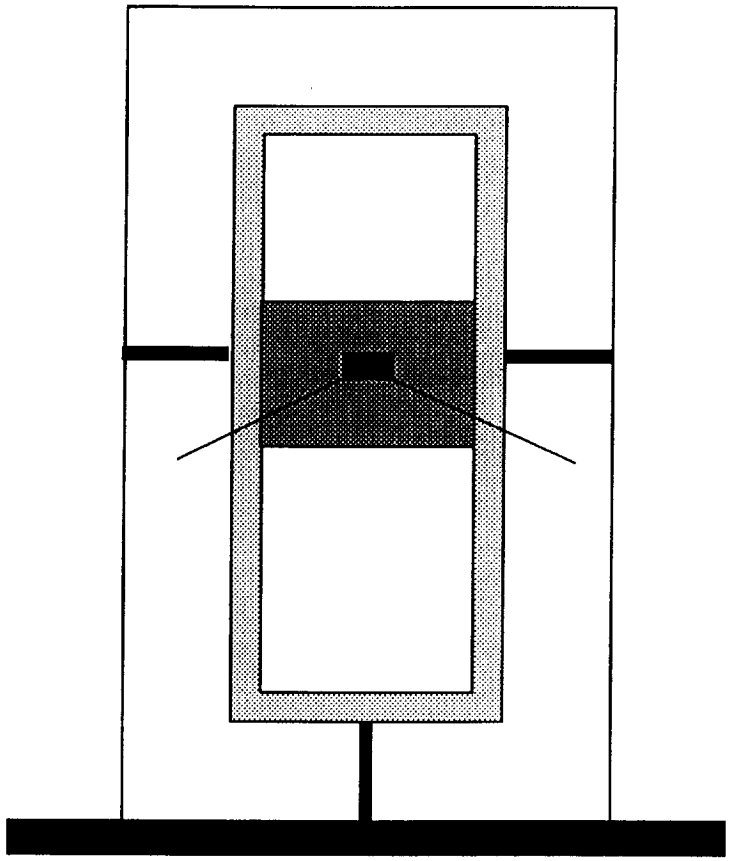

Figure 7.9 Paper Burning

7.12 The Coriolis Experiment.

"An orbiting body of mass, M, moving with uniform velocity, V, about a fixed point in space , O, possesses a centripetal force equal to MV^2 / R where R is the distance from the center of mass M to point O. If the mass is rigidly connected to point O, the tension in the member counterbalances both the gravitational force in the y-direction and the centripetal force in the x-direction as shown in Figure 7.10. A simple relation is easily obtained which relates the angle θ (between the x-axis and the member connecting point O to mass M) to the local gravitational acceleration:

$$g = R^2\Omega[\cos\theta \cot\theta] \tag{7.8}$$

This device is a simple accelerometer. If one measures the length R and the angle Θ in one g, one can calculate Ω in radians/sec. When the apparatus is dropped in the Low - gravity Demonstration Device, one will observe that the angle Θ is smaller than its one g counterpart. The gravitational acceleration during the drop can then be calculated since R, Ω, and Θ are known. In the limit as g approaches zero, Θ also approaches zero and the mass rotates in the x - z plane." (Pearlman)

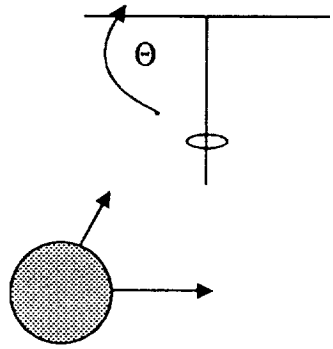

Figure 7.10 Coriolis

7.13 Summary

Even though many of the experiments just illustrated the effect of weight on systems, the visualness of the experiments serve greatly to demonstrate just how gravity affects a variety of systems. These experiments also teach just how interrelated many of the physical laws are, since many ideas were repeated in experiments. The experiments were successful because they met the criteria of being small enough to fit the 127mm X 127mm (5 in. X 5 in.) plate; they met the criteria of functioning in the small drop time; they simply and visually illustrated basic physical laws.

REFERENCES

Beer, Ferdinand P. and Russell Johnston, Jr. *Mechanics of Materials (Second Edition).* McGraw-Hill Inc., New York. 1992.

Jenkins, Andrew. Private Conversations. 1993.

National Aeronautics and Space Administration Conference Publication 10113. *Second International Microgravity Combustion Workshop, 1992.* NASA 1993.

National Aeronautics and Space Administration. *Microgravity Science and Applications Program Annual Report.* Fiscal Year 1992.

National Aeronautics and Space Administration. *Microgravity Science and Applications Program Biennial Report.* Fiscal Year 1990-1991.

National Aeronautics and Space Administration. *The First United States Microgravity Laboratory.* U.S. Government Printing Office. 1992.

Pearlman, Howard. Private Conversations. 1993.

Serway, Raymond A. *Physics for Scientists and Engineers (Third Edition).* Saunders College Publishing, Philadelphia. 1990.

Urban, David. Private Conversations. 1993.

Walter, H.U. (editor). *Fluid Sciences and Materials Science in Space.* Springer-Verlag, New York. 1987.

APPENDIX A

Instantaneous Photographs of Experiments at
Low-g and Normal-g

Pendulum Experiment

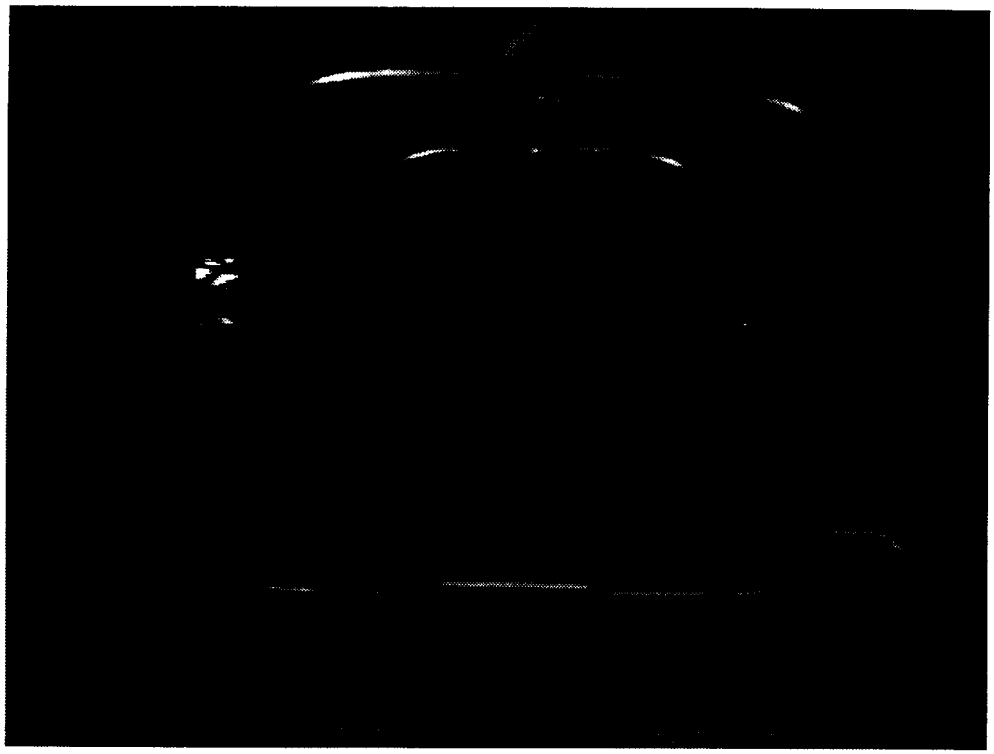

Low - g

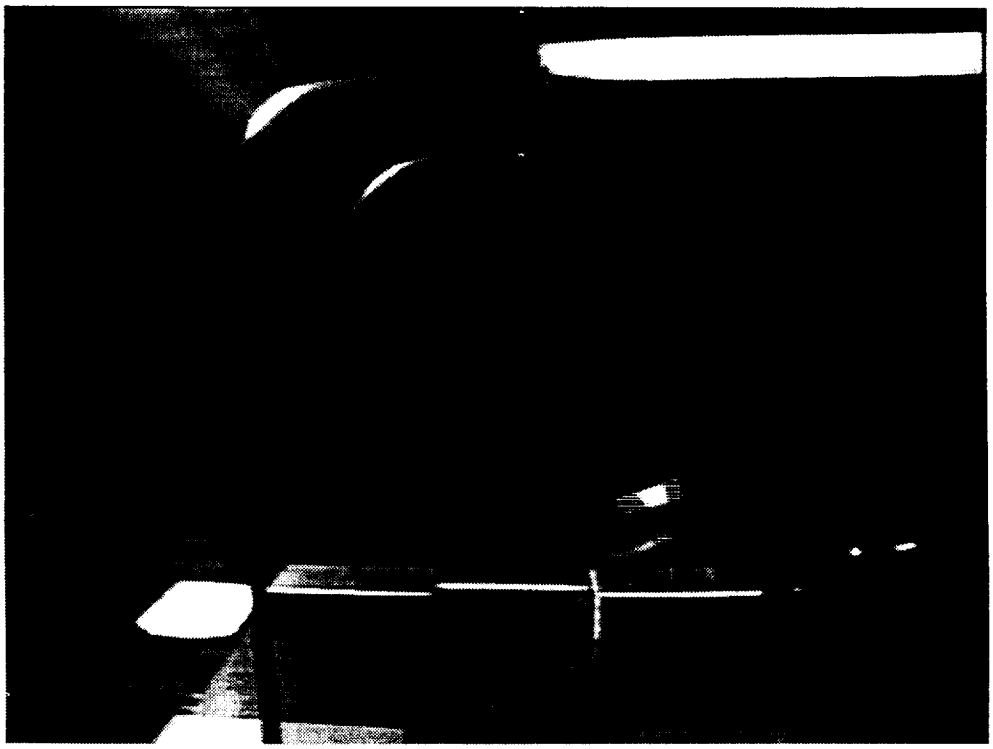

normal - g

Bouyancy Experiment

Scale Experiment

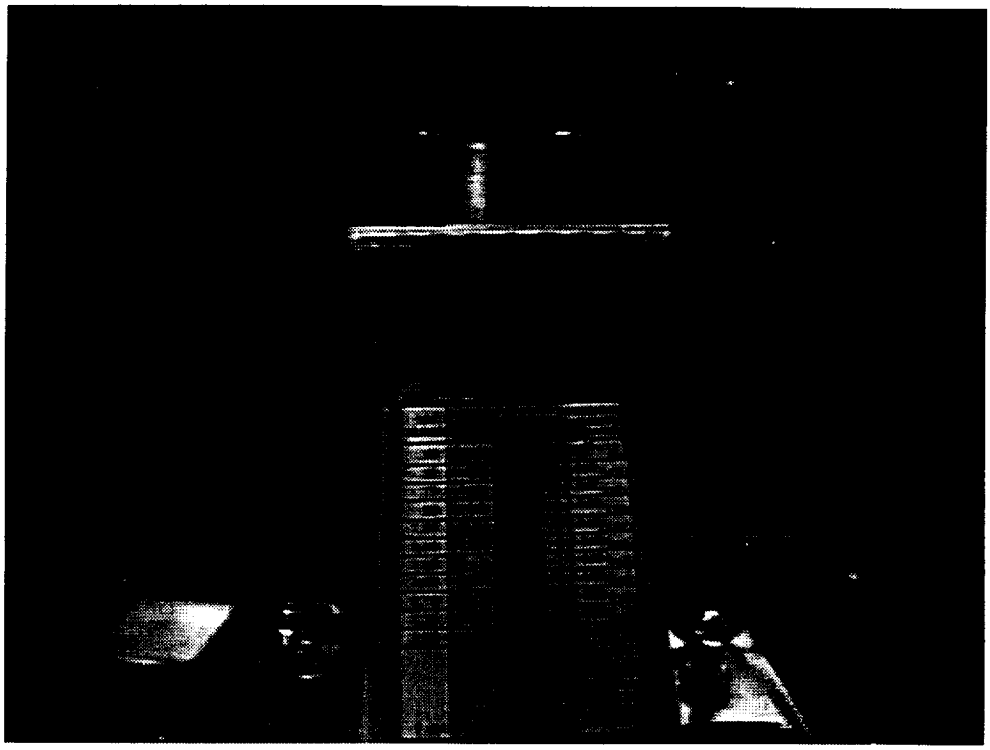

Low - g

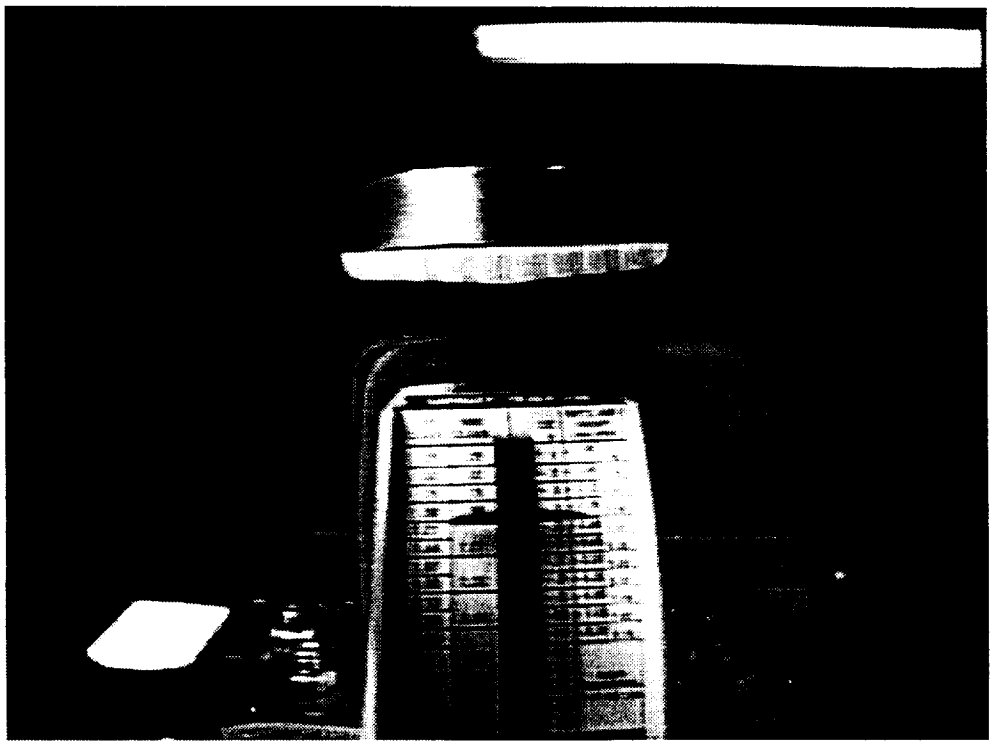

normal - g

Tension Experiment

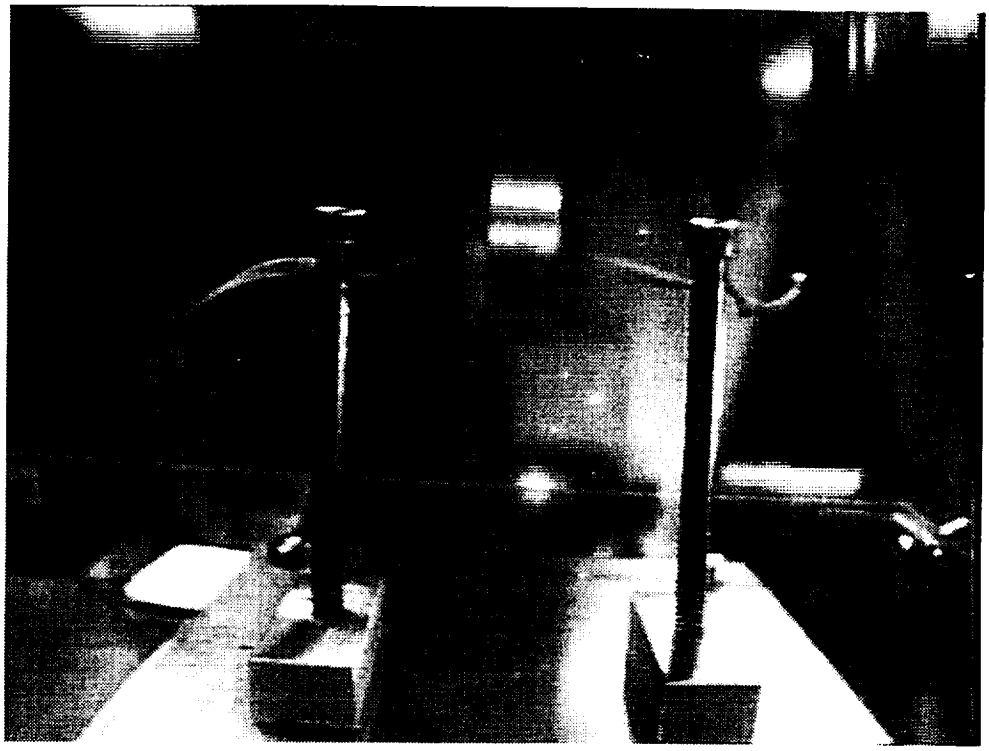

Low - g

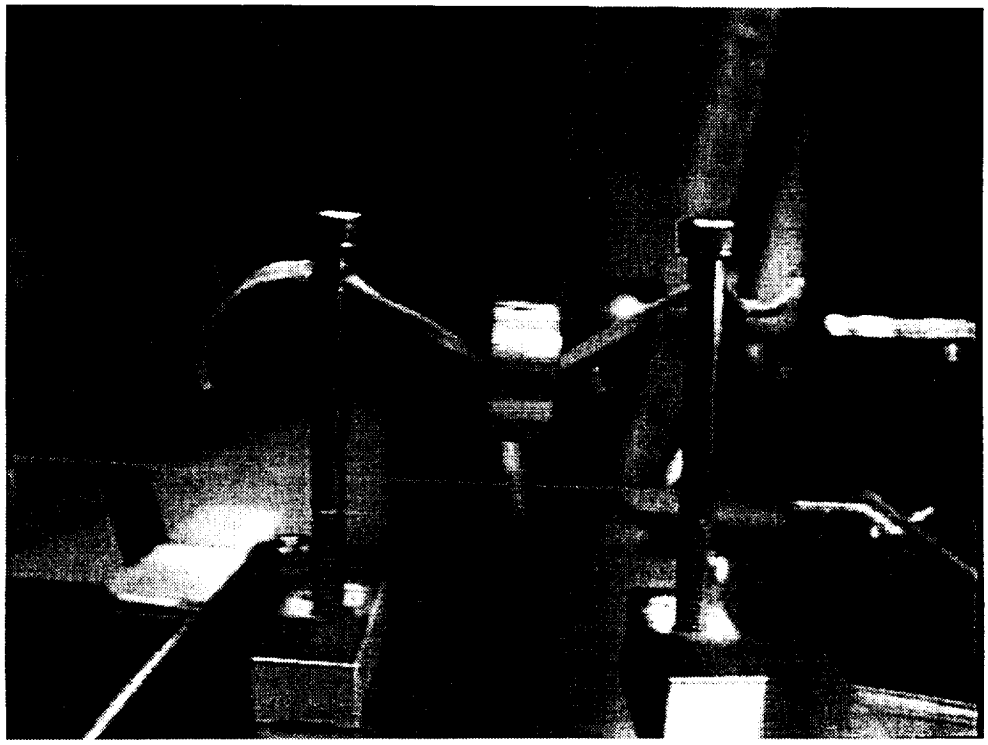

normal - g

Magnet Experiment

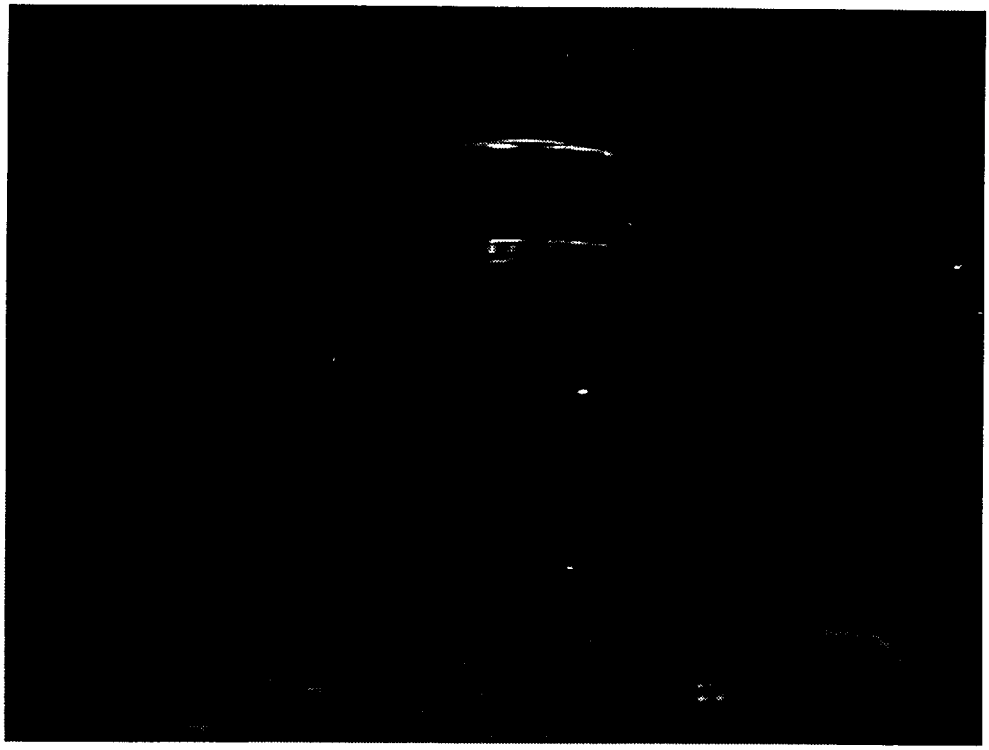

Low - g

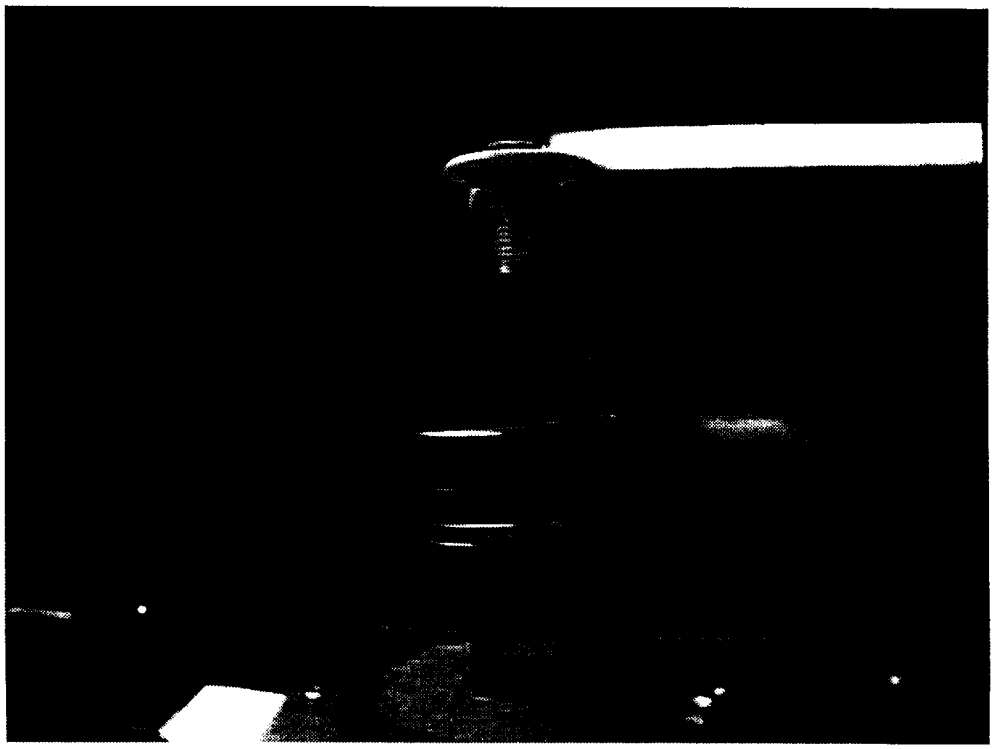

normal - g

Newton's Cradle Experiment

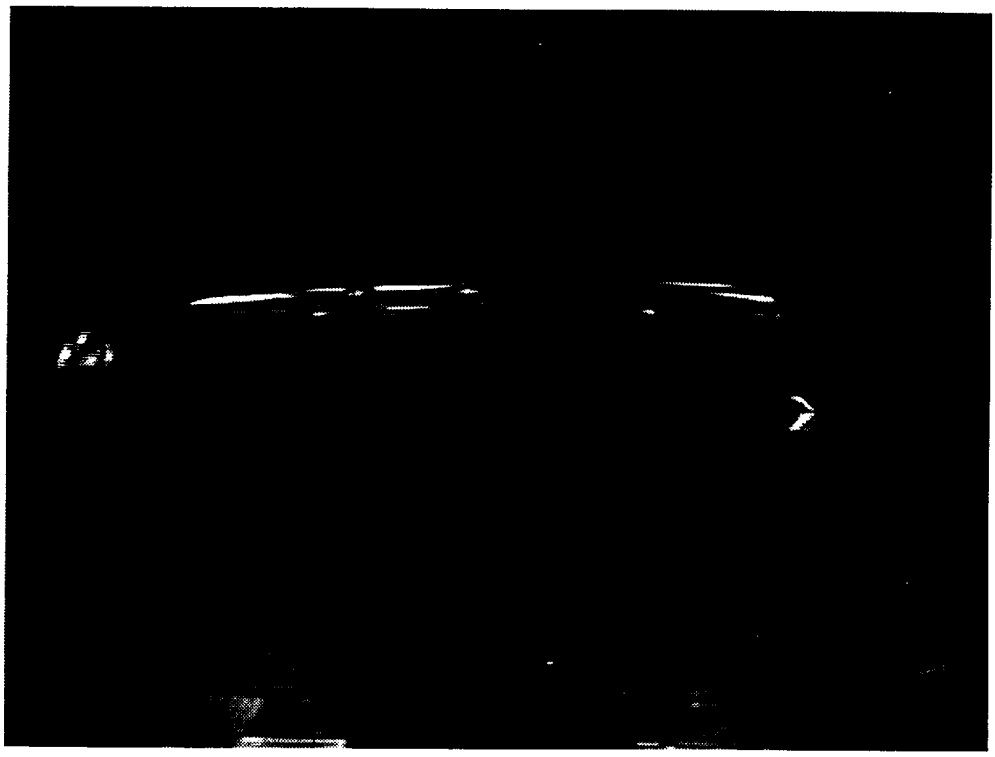

Low - g

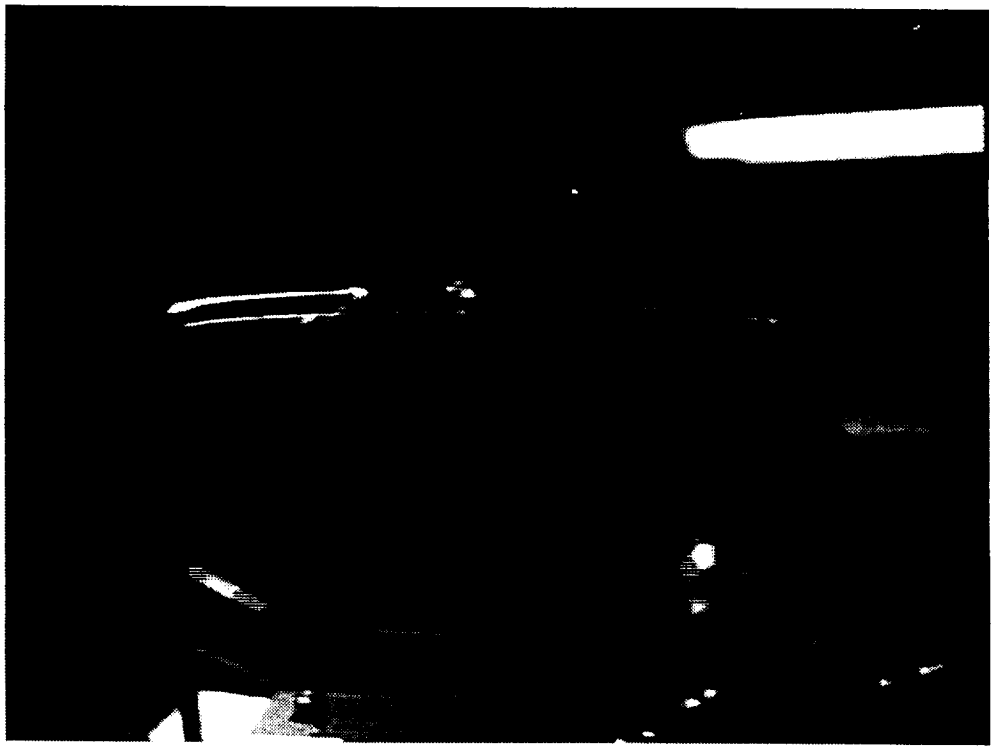

normal - g

Meniscus Experiment

Low - g

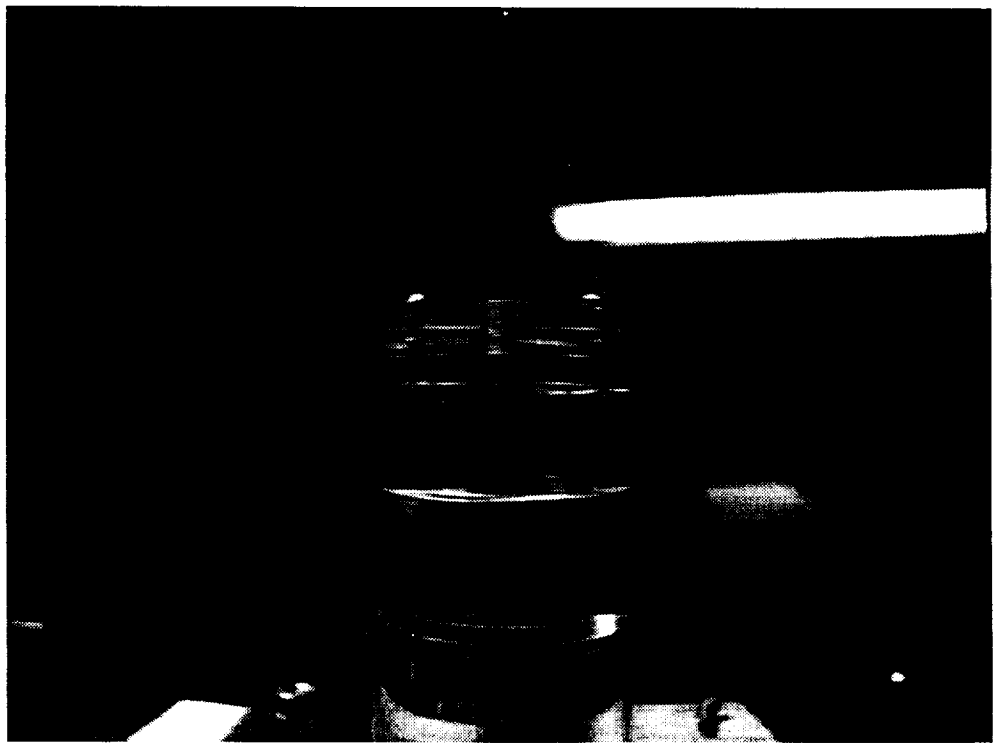

normal - g

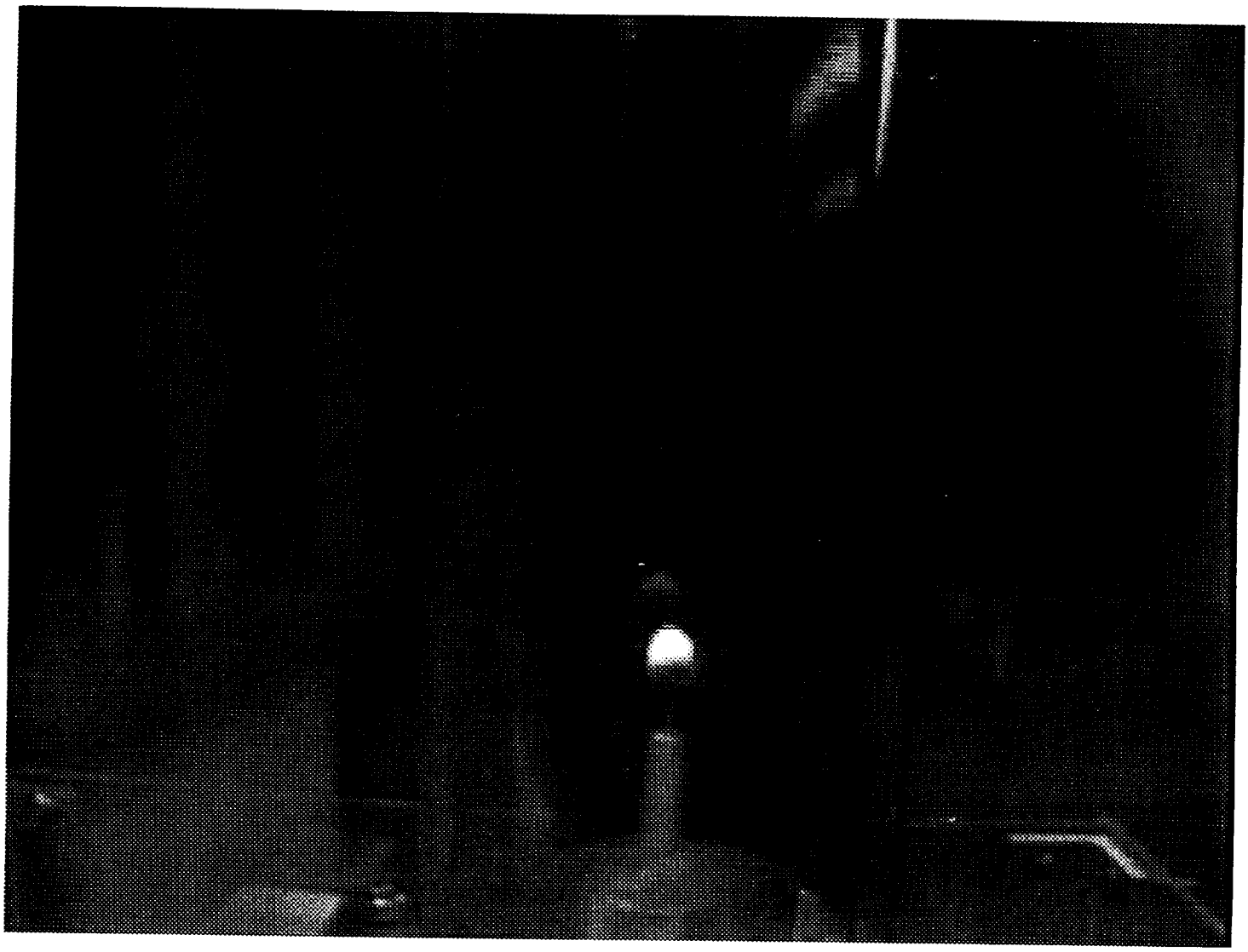

Candle Experiment
Low-g

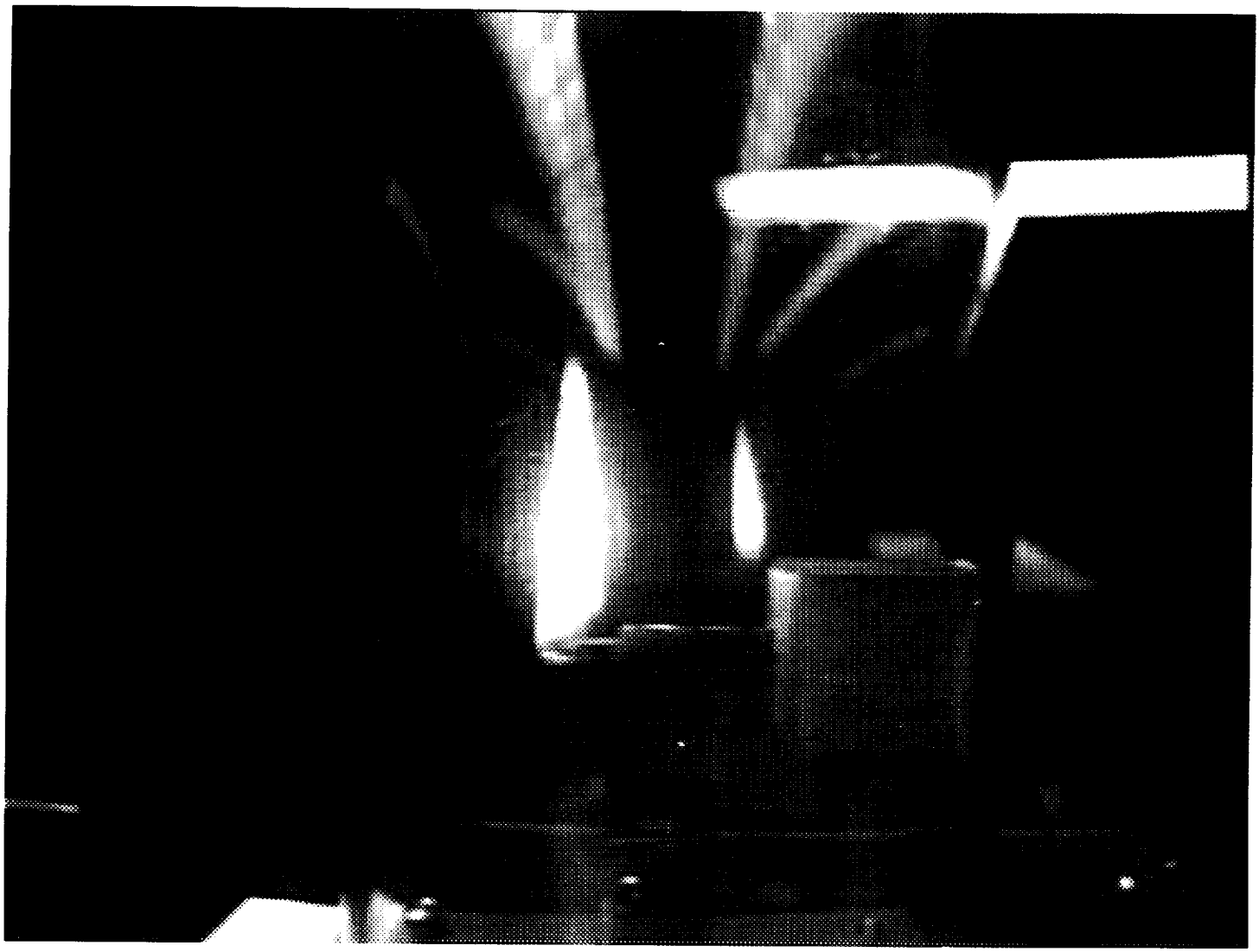

Horizontal Candle Experiment

Normal - g

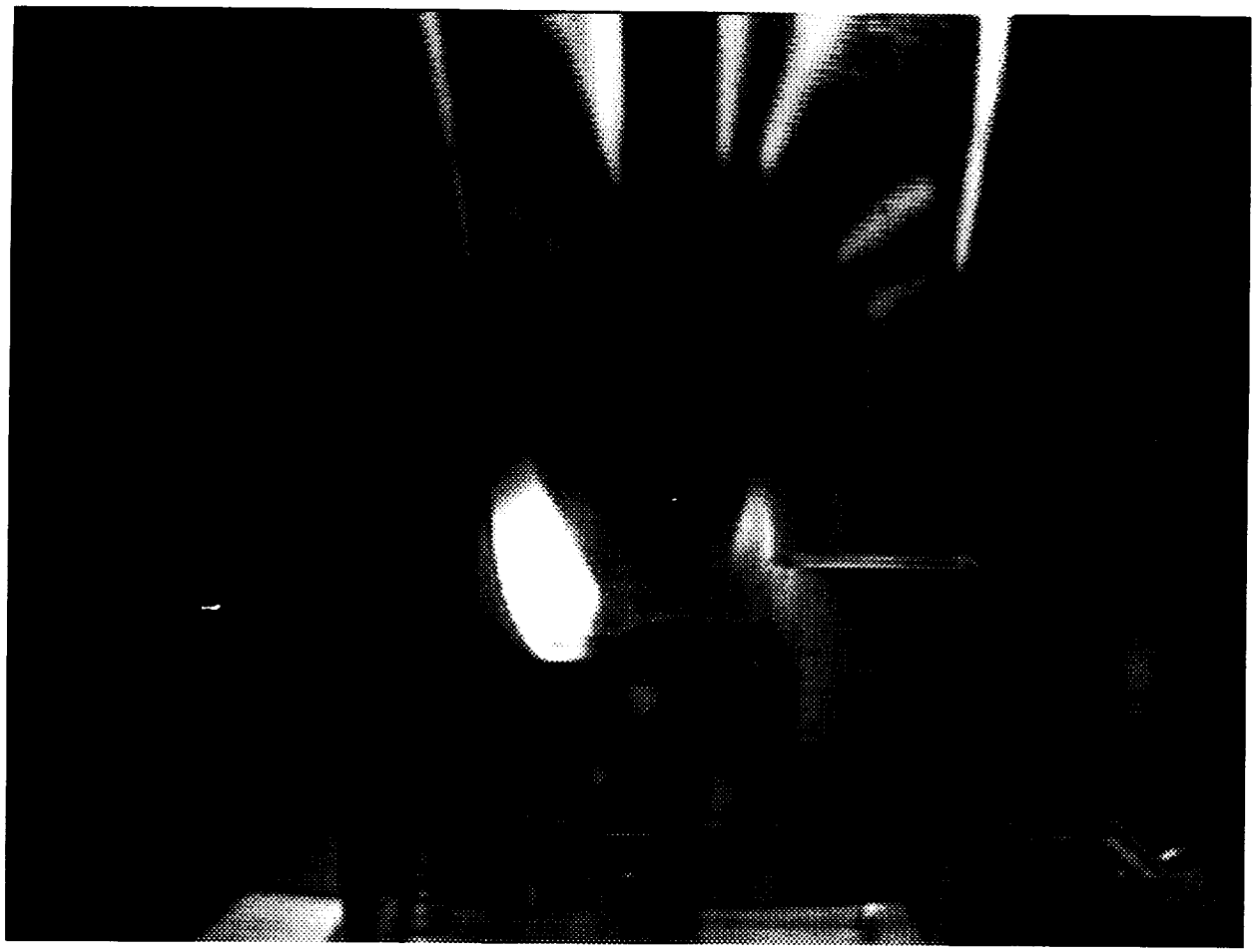

Horizontal Candle Experiment

Low - g

Low - g : Flame Spread on Paper

Coriolis Experiment

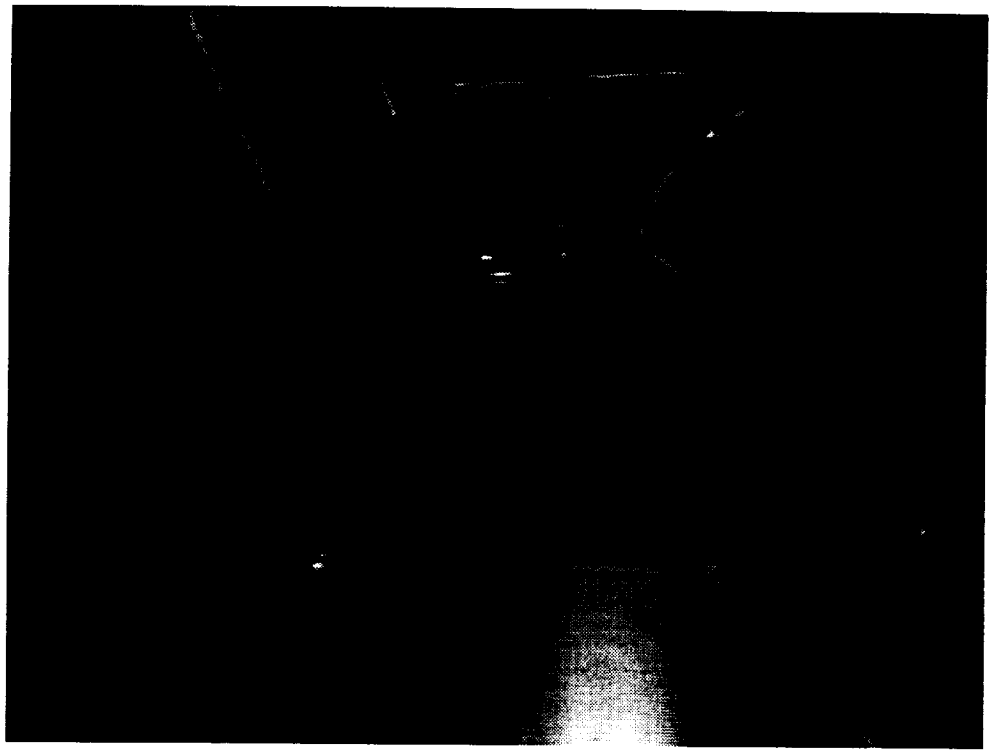

Low - g

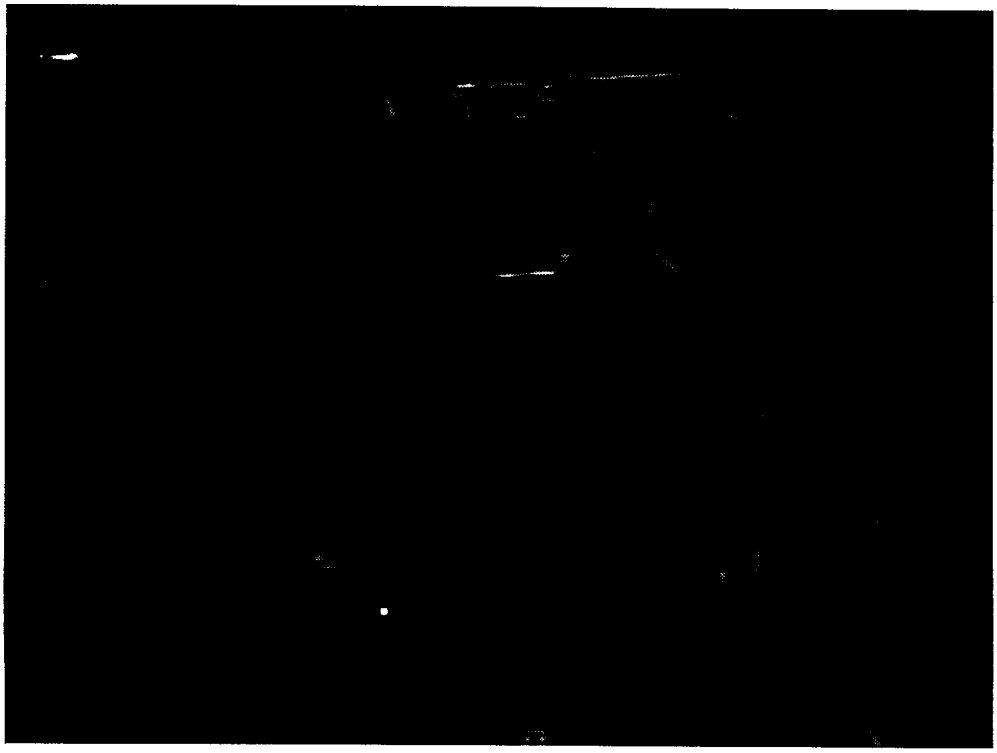

normal - g

APPENDIX B

Schematic Drawings of the Miniature Tower

Base Plate

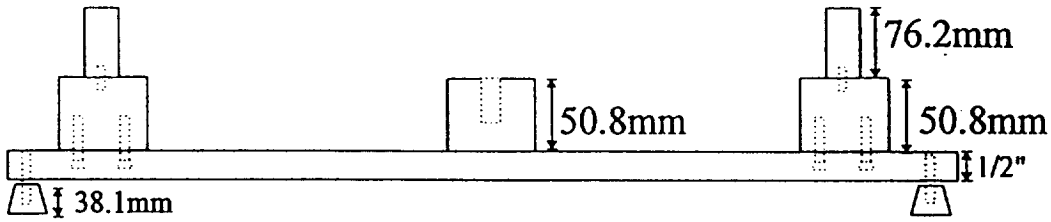

Side View

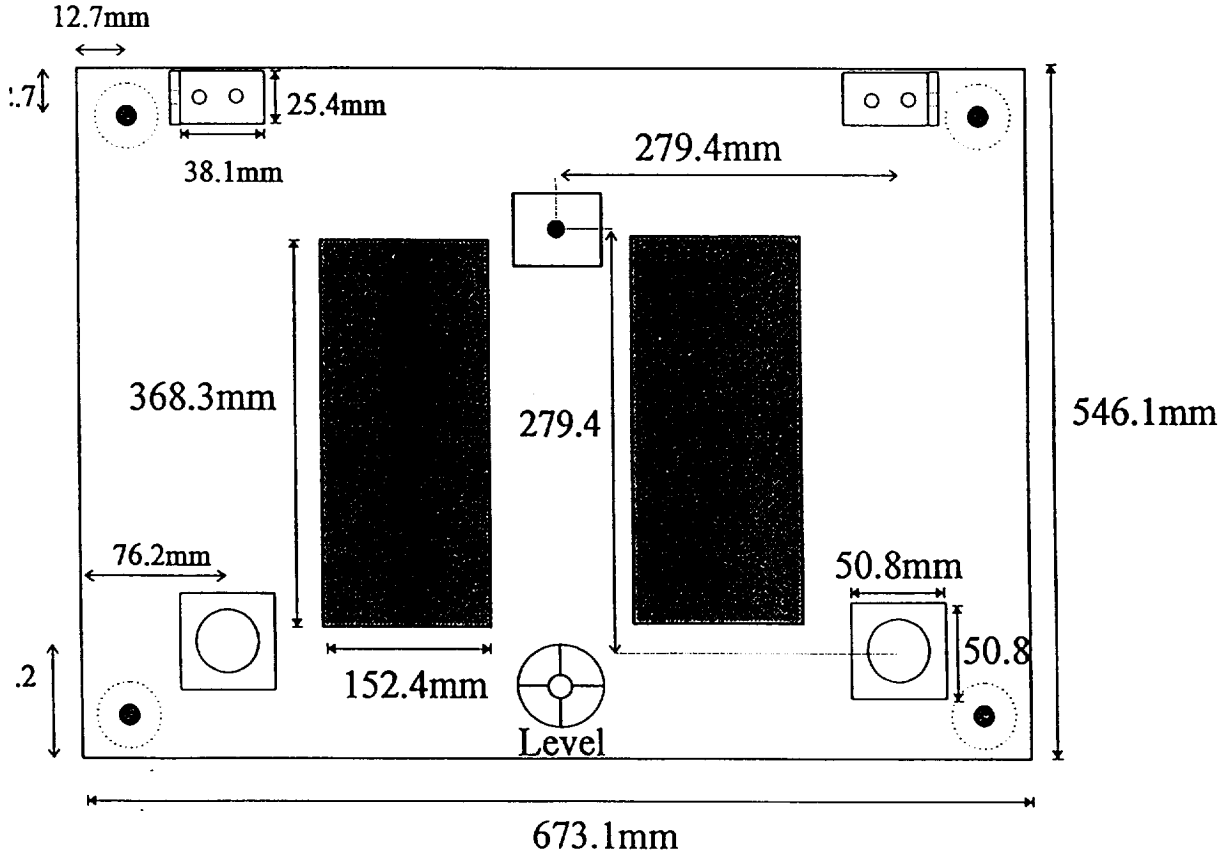

Top View

Top Plate

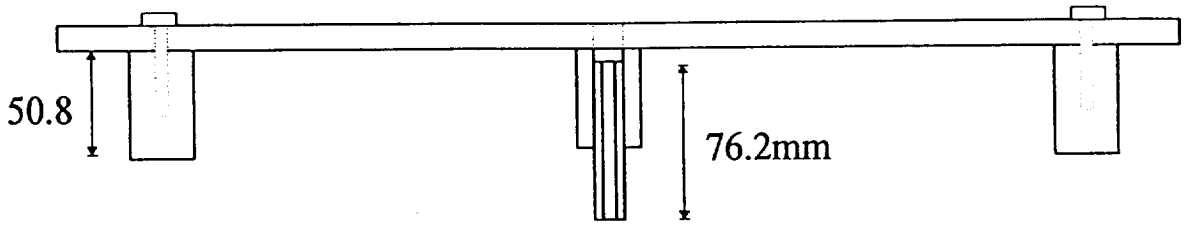

Front View

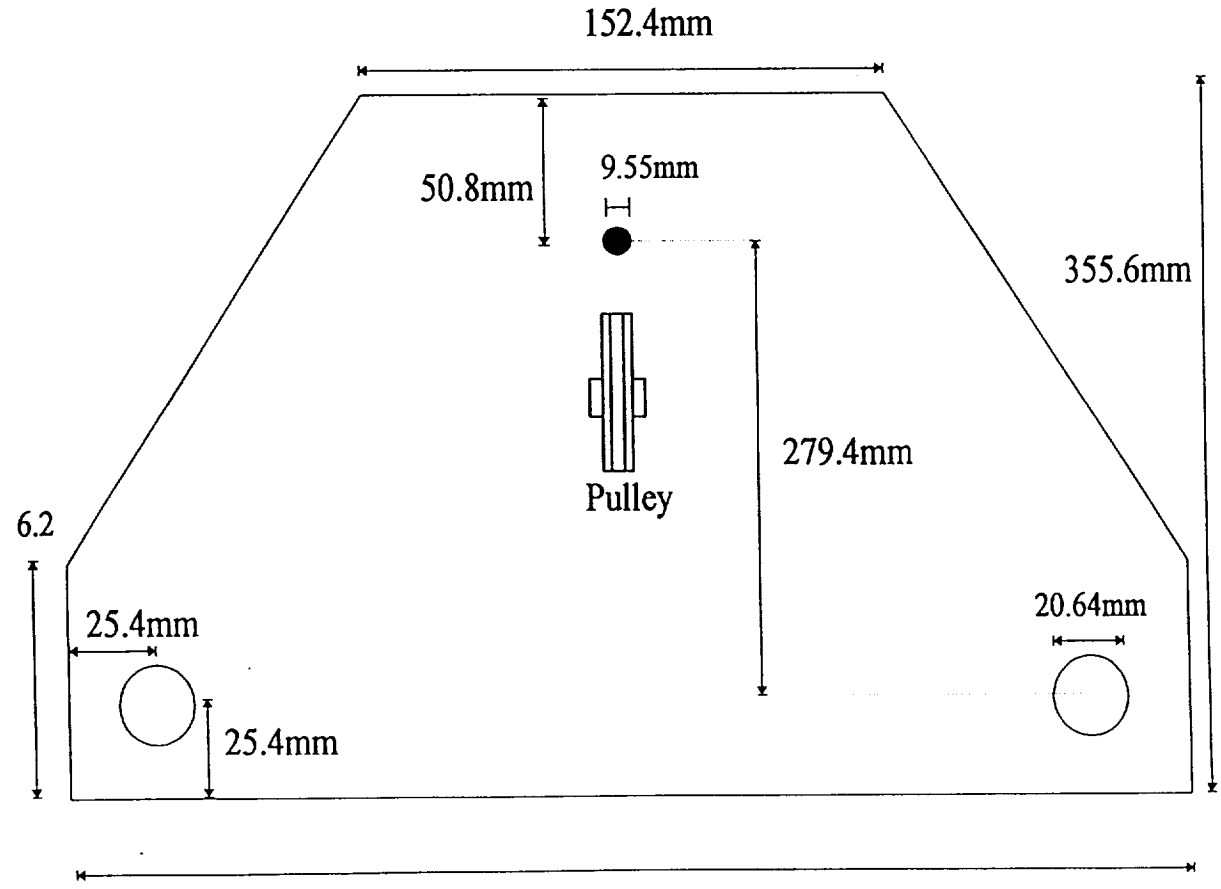

Bottom View

Shaft and Supports

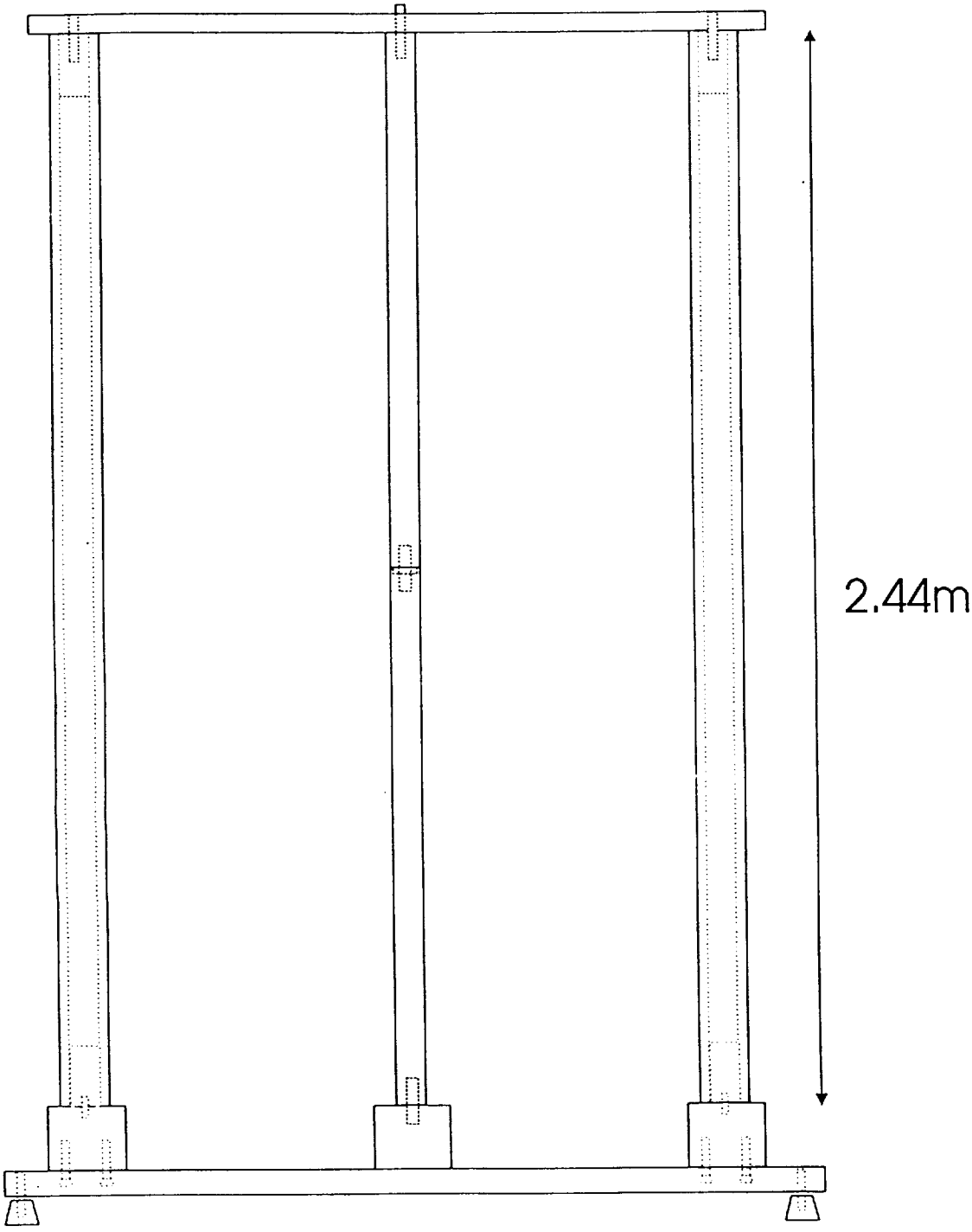

Front View

Shaft and Supports

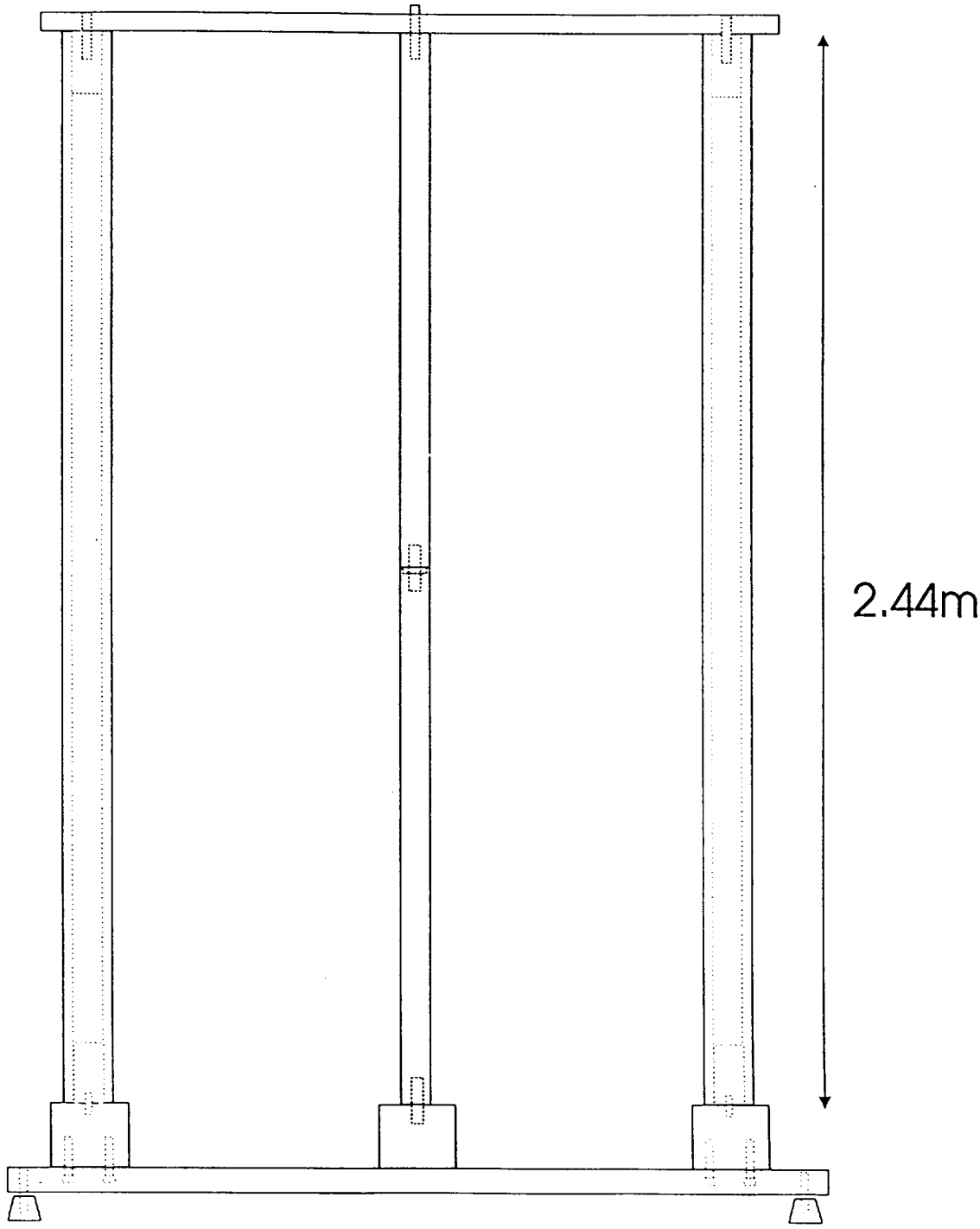

Front View

Structural Supports

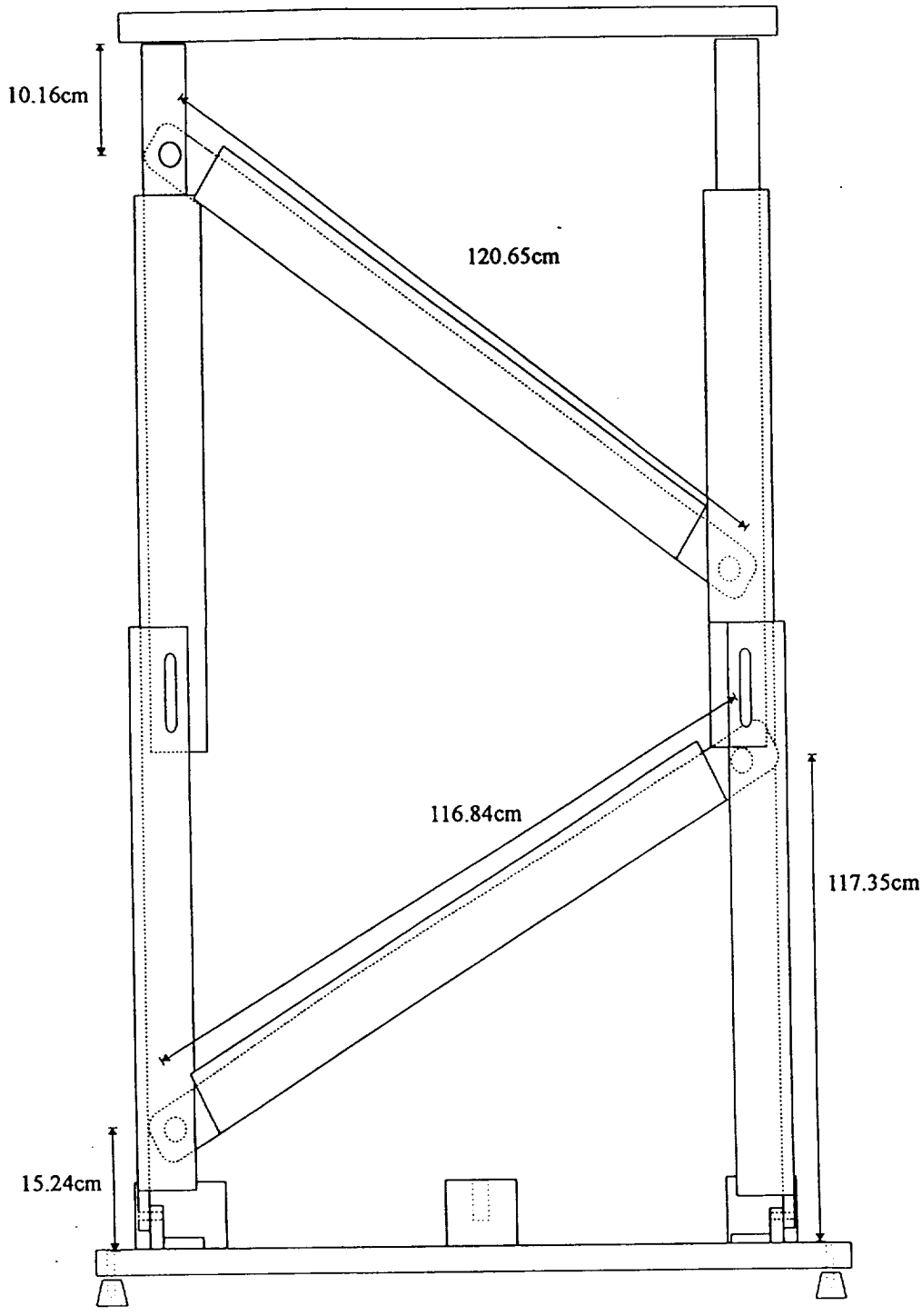

Front View

Shaft and Supports Rods

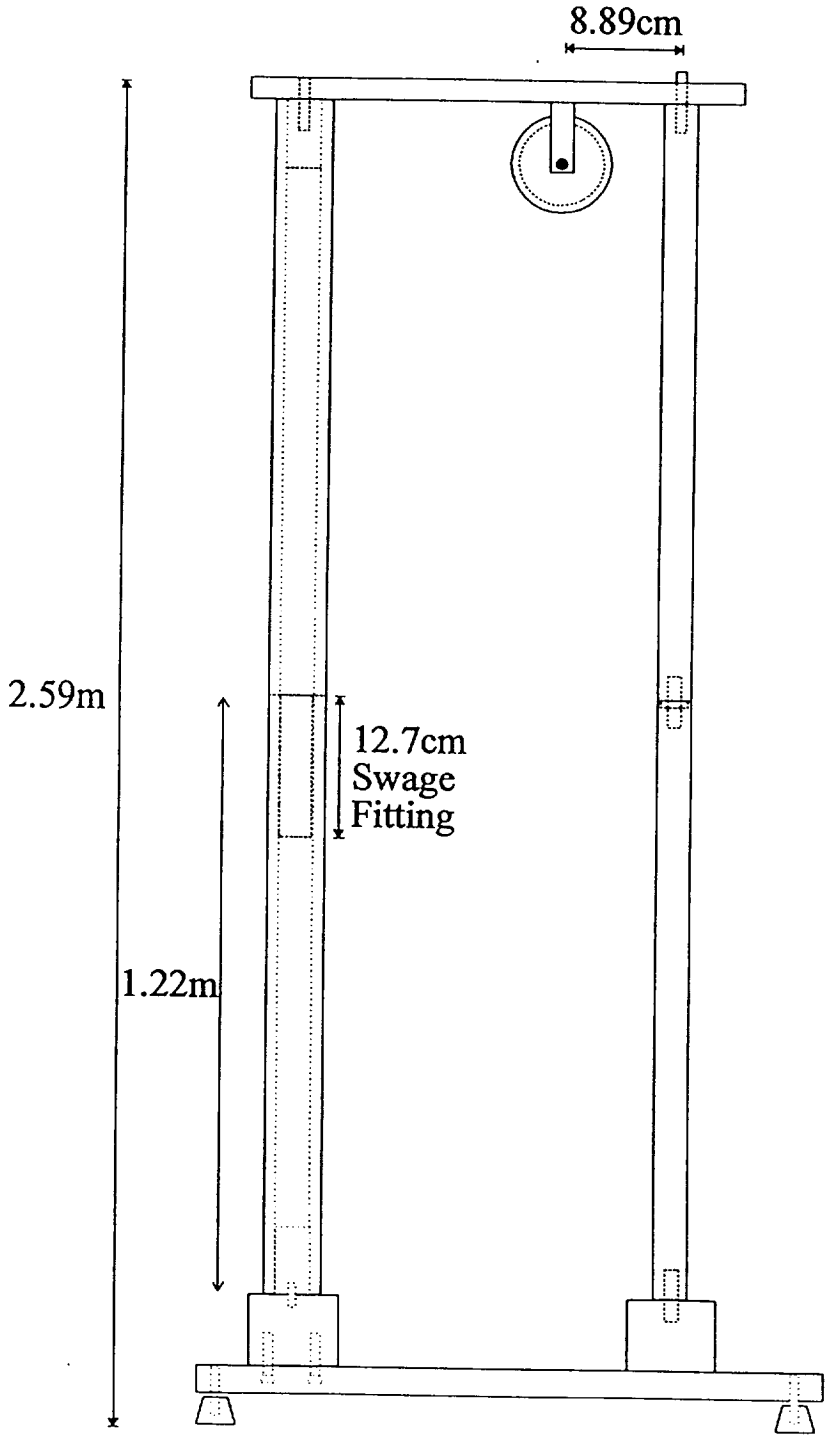

Side View

Stuctural Supports

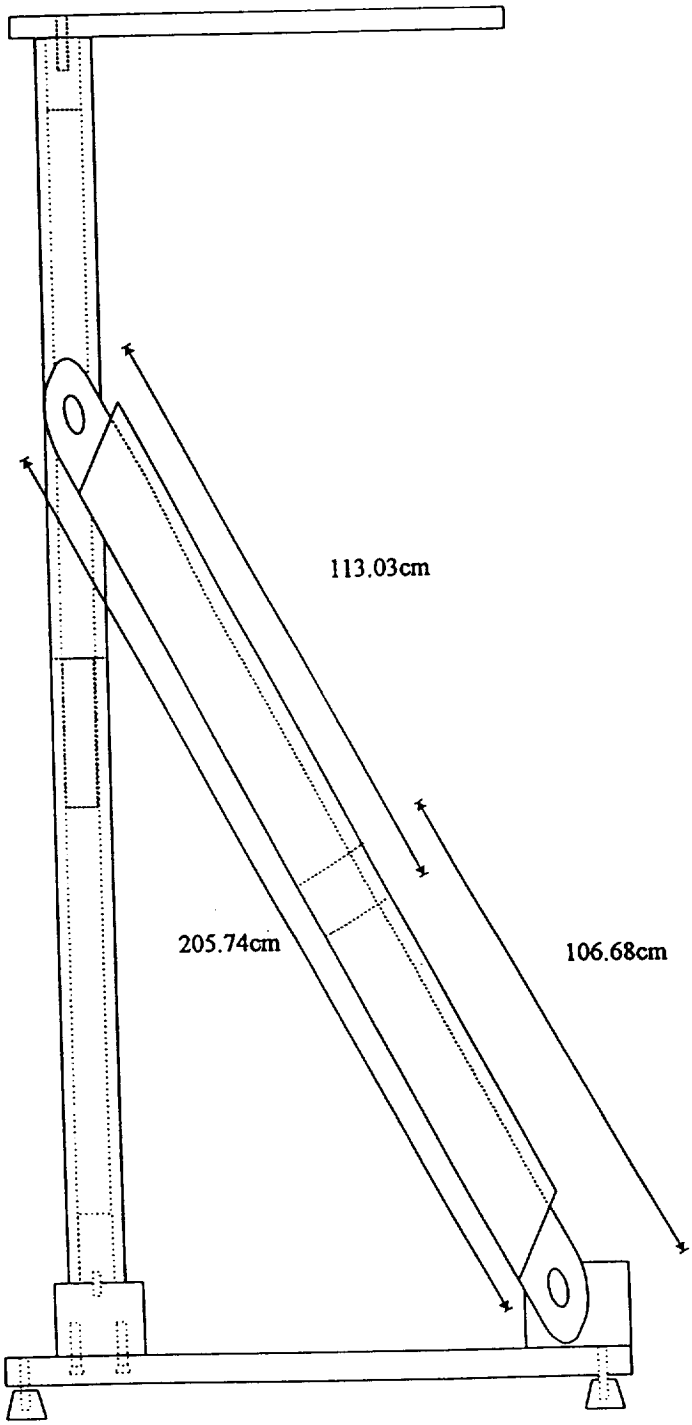

Side View

APPENDIX C

Organization Chart

The group that is responsible for micro gravity experimentation is the Micro gravity Science and Applications Division (MSAD). It is within the Office of Space Science and Applications (OSSA). MSAD is broken down into four Science Discipline Working Groups, studying Biotechnology, Combustion, Fluids and Transport Phenomena and Materials Science. The Mini-Drop Tower is sponsored by the Micro gravity Combustion Group.

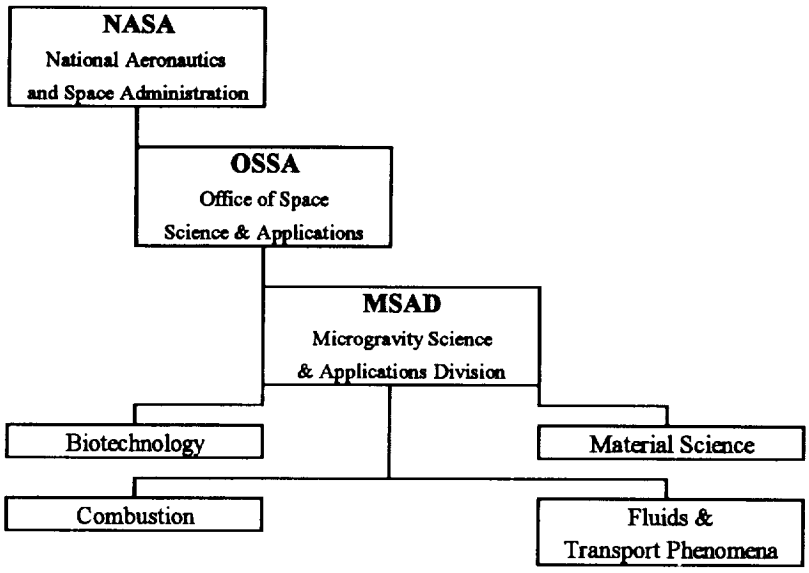

APPENDIX D

Drop Tower Payload Acceleration Data

Drop Accelerations
10 Foot Drop

Drop	x-pos.	time (s)	frame	Frame T.	Total T.	vel (in/s)	Accell(in/s2)	accell(ft/s2)
10-3	26.25	3	6	0.2	3.2	0	0	0
7:19	26.5	3	7	0.233333	3.233333	7.5	225	18.75
	27	3	8	0.266667	3.266667	15	225	18.75
	27.875	3	9	0.3	3.3	26.25	337.5	28.125
	28.95	3	10	0.333333	3.333333	32.25	180	15
	30.875	3	11	0.366667	3.366667	57.75	765	63.75
	33	3	12	0.4	3.4	63.75	180	15
	35.5	3	13	0.433333	3.433333	75	337.5	28.125
	38.5	3	14	0.466667	3.466667	90	450	37.5
	41.75	3	15	0.5	3.5	97.5	225	18.75
	45.5	3	16	0.533333	3.533333	112.5	450	37.5
	49.75	3	17	0.566667	3.566667	127.5	450	37.5
	54.25	3	18	0.6	3.6	135	225	18.75
	59.25	3	19	0.633333	3.633333	150	450	37.5
	64.5	3	20	0.666667	3.666667	157.5	225	18.75
	70.25	3	21	0.7	3.7	172.5	450	37.5
	76.25	3	22	0.733333	3.733333	180	225	18.75
	82.75	3	23	0.766667	3.766667	195	450	37.5
	89.75	3	24	0.8	3.8	210	450	37.5
	97	3	25	0.833333	3.833333	217.5	225	18.75
	104.5	3	26	0.866667	3.866667	225	225	18.75
	112.5	3	27	0.9	3.9	240	450	37.5
	120.75	3	28	0.933333	3.933333	247.5	225	18.75
							Average acell=	29.0625

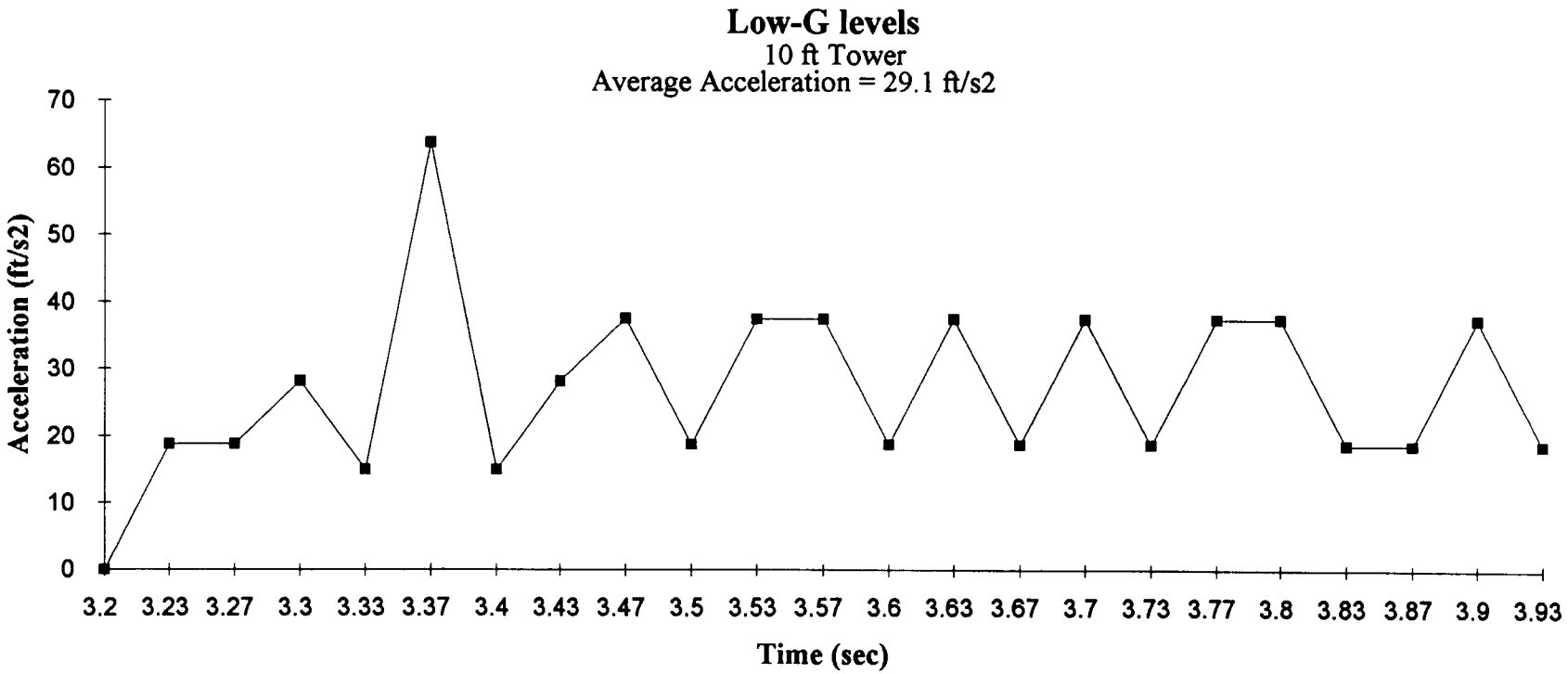
Low-G levels
10 ft Tower
Average Acceleration = 29.1 ft/s2
Acceleration (ft/s2)
70
60
50
40
30
20
10
0
3.2
3.23
3.27
3.3
3.33
3.37
3.4
3.43
3.47
3.5
3.53
3.57
3.6
3.63
3.67
3.7
3.73
3.77
3.8
3.83
3.87
3.9
3.93
Time (sec)

Drop Accelerations
8 Foot Tower

Drop	x-pos (in)	time(s)	frame	Frame T	Total T	vel(ft/s)	Accell(ft/s2)
8-6	51.5	7	15	0.50	7.50		
5:56s	51.5	7	16	0.53	7.53	0	0
	51.875	7	17	0.57	7.57	0.9375	28.125
	52.5	7	18	0.60	7.60	1.5625	18.75
	53.5	7	19	0.63	7.63	2.5	28.125
	54.875	7	20	0.67	7.67	3.4375	28.125
	56.75	7	21	0.70	7.70	4.6875	37.5
	59	7	22	0.73	7.73	5.625	28.125
	61.75	7	23	0.77	7.77	6.875	37.5
	64.75	7	24	0.80	7.80	7.5	18.75
	68.25	7	25	0.83	7.83	8.75	37.5
	72	7	26	0.87	7.87	9.375	18.75
	76.375	7	27	0.90	7.90	10.9375	46.875
	81	7	28	0.93	7.93	11.5625	18.75
	86.125	7	29	0.97	7.97	12.8125	37.5
	91.625	8	0	0.00	8.00	13.75	28.125
	97.5	8	1	0.03	8.03	14.6875	28.125
	103.625	8	2	0.07	8.07	15.3125	18.75
	110.25	8	3	0.10	8.10	16.5625	37.5
	117.25	8	4	0.13	8.13	17.5	28.125
	124.625	8	5	0.17	8.17	18.4375	28.125
	impact	8	6	0.20	8.20	-311.5625	-9900
						Average accell=	29.11184211

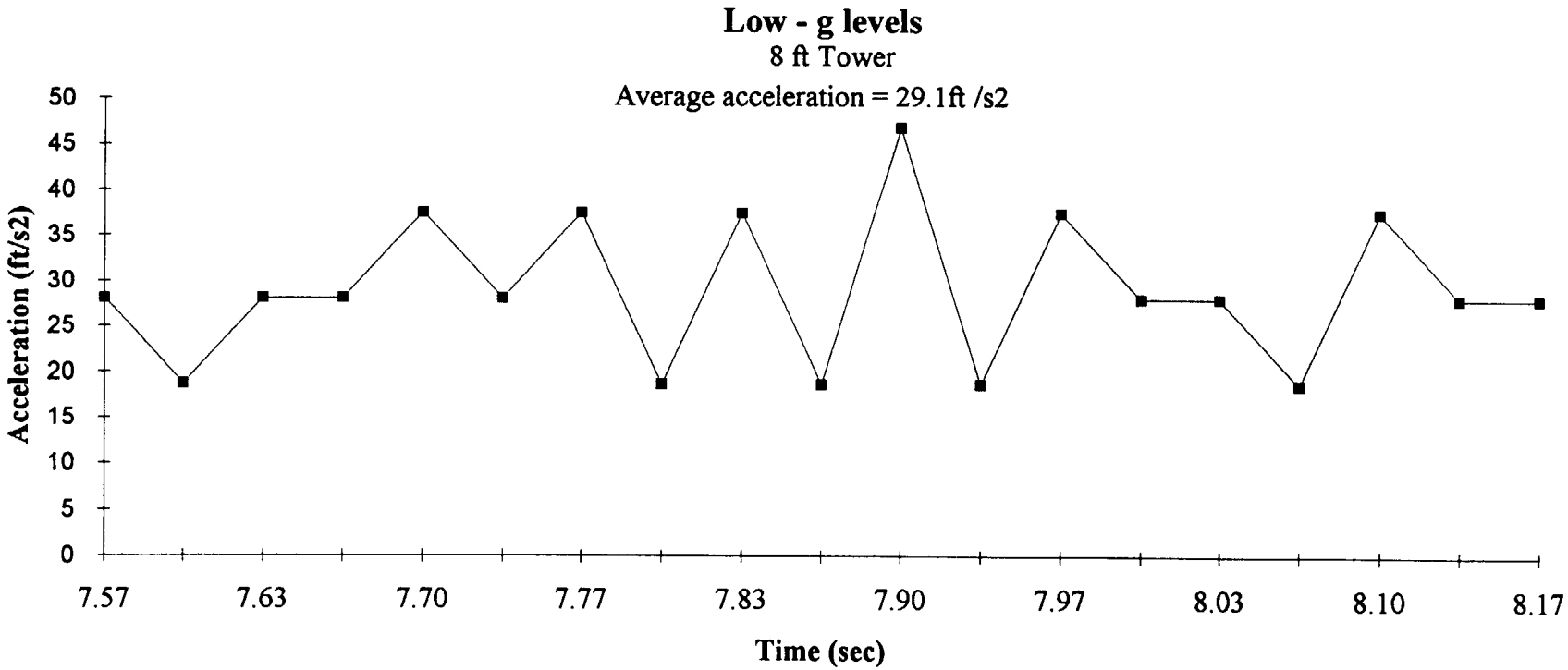
Low - g levels
8 ft Tower
Average acceleration = 29.1ft /s2
Acceleration (ft/s2)
50
45
40
35
30
25
20
15
10
5
0
7.57
7.63
7.70
7.77
7.83
7.90
7.97
8.03
8.10
8.17
Time (sec)

APPENDIX E

Instrument Specification - Accelerometer

MOTION
shock & vibration

PCB
PIEZOTRONICS

QUARTZ, LOW-IMPEDANCE, VOLTAGE-MODE
ACCELEROMETER
with built-in amplifier
Model 308B03

- high sensitivity (50mV/g); low noise (0.002g)
- rugged quartz element — shock protected
- low cost system — no external amplifier or special cable
- side connector; couples directly to readout
- high level (±5 volt), low impedance output (<100 ohm)
- signal unaffected by cable length or motion

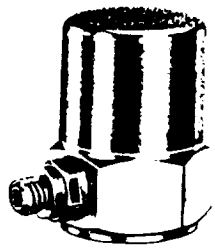

See Optional Model below Specifications.

Typical System Kit
Model K308B03
Includes Battery Power Unit, Cables and Accessories

Model 308B03 measures shock and vibration on machine tools, machinery, vibrators, impact testers, vehicles, trains, boats, buildings, bridges, containers and other structures.

Model 308B03, a modern, low-impedance, high-precision quartz accelerometer, routinely measures shock and vibratory motion in both laboratory and rough industrial environments. Containing a sensitive, proven quartz element and advanced, low-noise microelectronic circuitry, this precision instrument measures the acceleration aspect of vibratory motion to very low amplitudes and frequencies. Acceleration relates directly to force causing the motion.

To operate it you need only a low cost battery power/signal conditioner as shown below in the typical system. A complete line of low cost single and multi-channel power units with or without gain is available. True RMS meter monitors like the 487A05 and 487A06 with high set point also contain the power circuit for these accelerometers. The basic power circuit is now incorporated in many FFT analyzers.

Options include: ground isolation, welded hermetic seal, other sensitivities and a solder terminal adaptor, (Model 070A09) for ordinary 2-wire cable connections. See accessories sheet for adhesive and magnetic mounting bases.

SPECIFICATIONS: Model No.		308B03
Range (±5V output)	g	±100
Resolution	g	0.002
Sensitivity (±2%)	mV/g	50
Resonant Frequency	Hz	25000
Frequency Range (±5%)	Hz	1 - 3000
Frequency Range (±10%)	Hz	.7 - 6000
Discharge Time Constant	s	0.5
Linearity	%FS	1.0
Output Impedance	ohm	<100
Output Bias	V	9 to 12
Overload Recovery	μs	10
Transverse Sensitivity (max)	%	5
Strain Sensitivity	g/μin/in	0.05
Temperature Coefficient	%/°F	0.03
Temperature Range	°F	-100 to +250
Vibration (max)	g	±1000
Shock (max)	g	10000
Size (hex x height)	in	3/4 x 1.1
Weight	gm	55
Connector (side)	micro	10-32
Case Material		SS
Sealing		epoxy
Structure (isolated-compression)		upright
Excitation (constant current)	mA	2 to 20
Voltage to current regulator	VDC	+18 to 28
Optional Model: Hermetically sealed		308B11

Typical Systems: K308B03 battery power kit is shown below. Also available as GK308B03 with gain. Recharge and long life external battery pack options available.

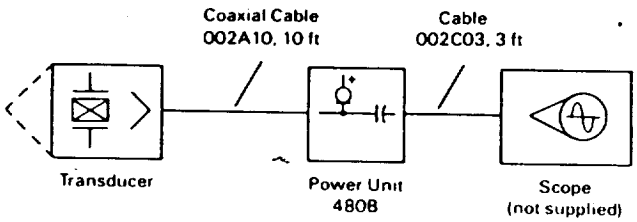

DIMENSIONS:

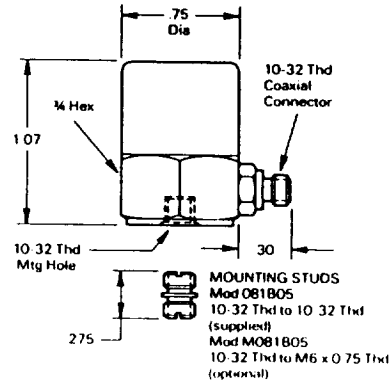

APPENDIX F

Payload Impact Decceleration Measurement

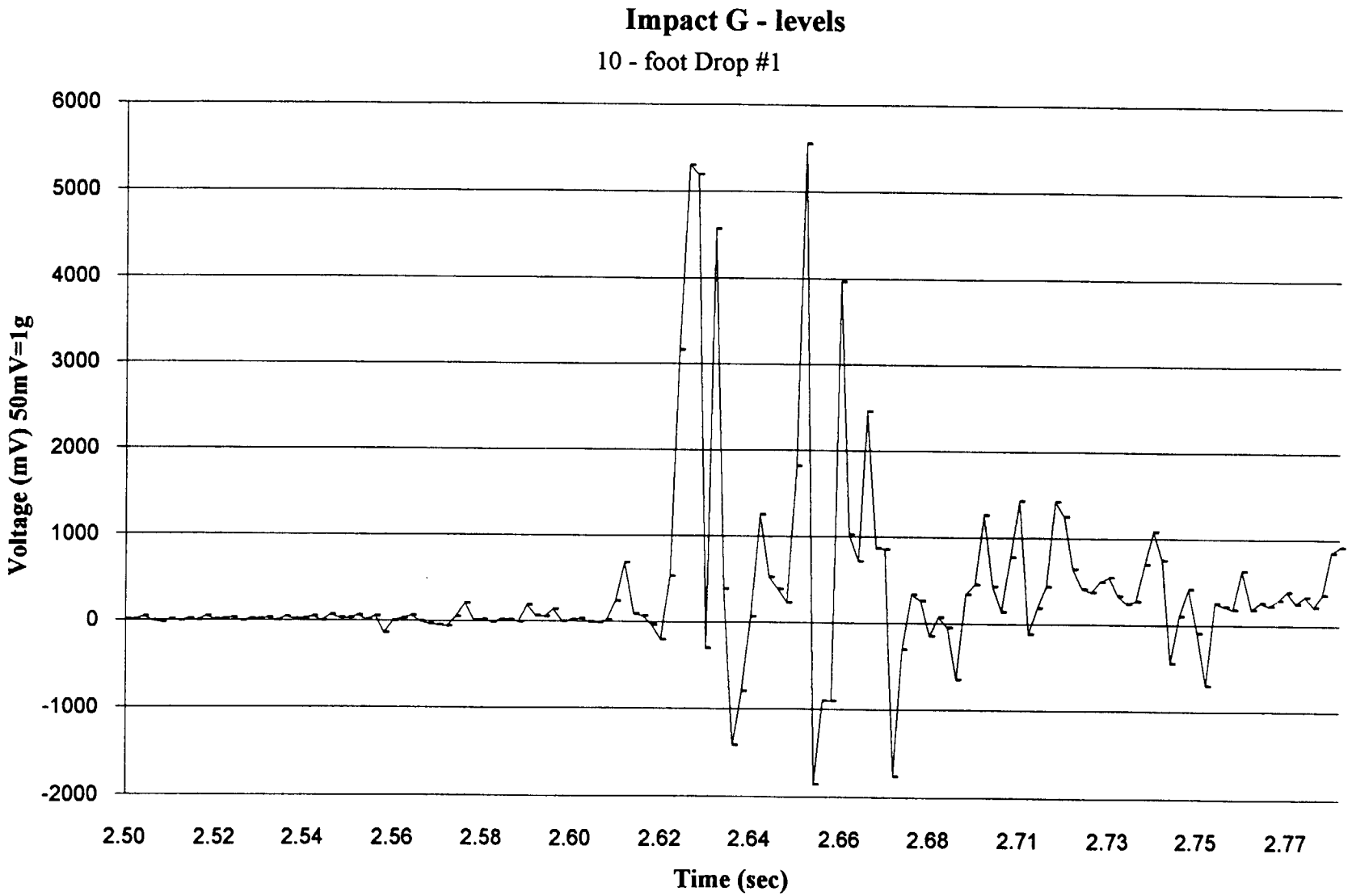
Impact G - levels
10 - foot Drop #1
Voltage (mV) 50mV=1g
6000
5000
4000
3000
2000
1000
0
-1000
-2000
2.50
2.52
2.54
2.56
2.58
2.60
2.62
2.64
2.66
2.68
2.71
2.73
2.75
2.77
Time (sec)

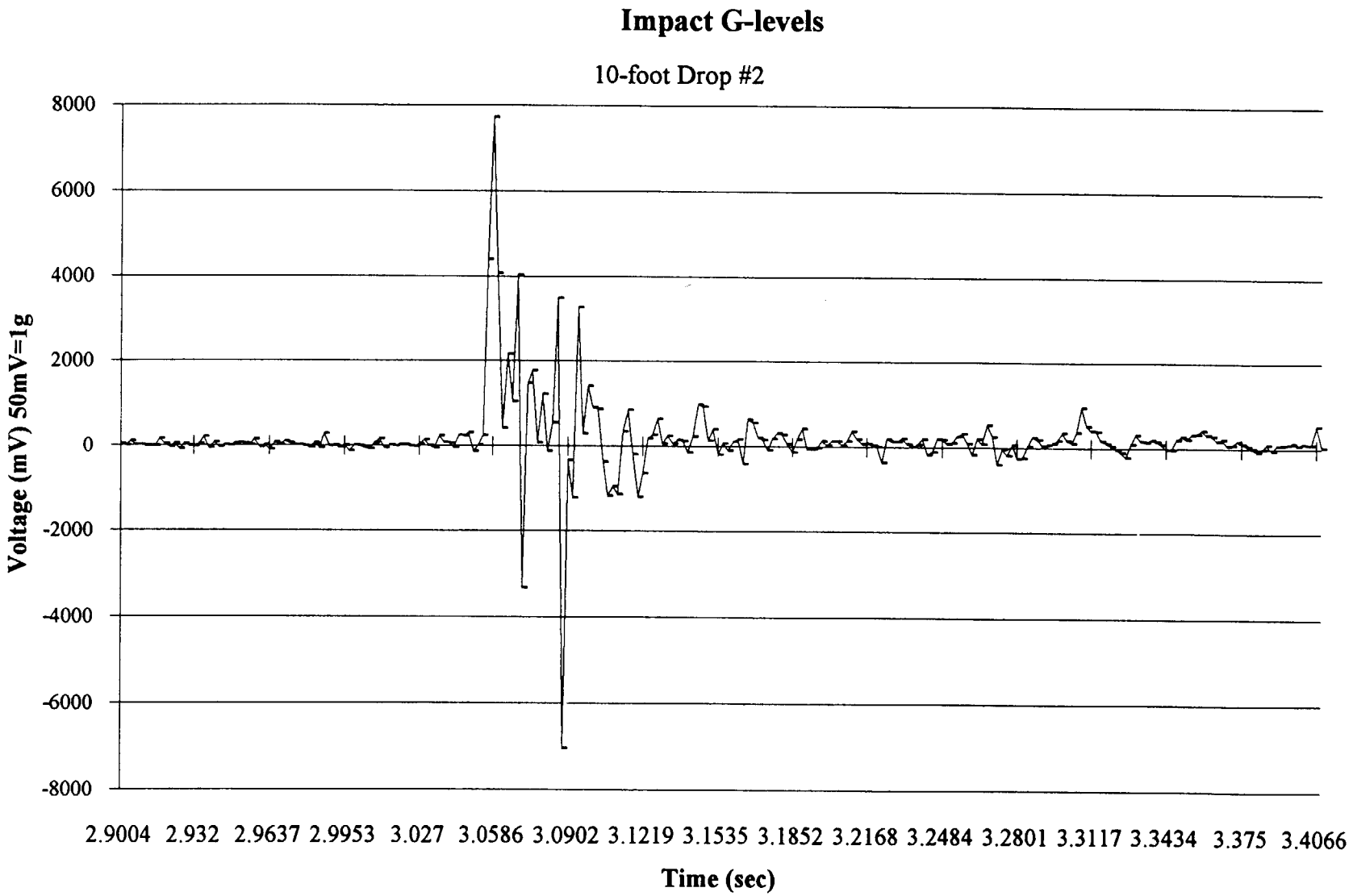
Impact G-levels
10-foot Drop #2
8000
6000
4000
2000
0
-2000
-4000
-6000
-8000
Voltage (mV) 50mV=1g
2.9004 2.932 2.9637 2.9953 3.027 3.0586 3.0902 3.1219 3.1535 3.1852 3.2168 3.2484 3.2801 3.3117 3.3434 3.375 3.4066
Time (sec)

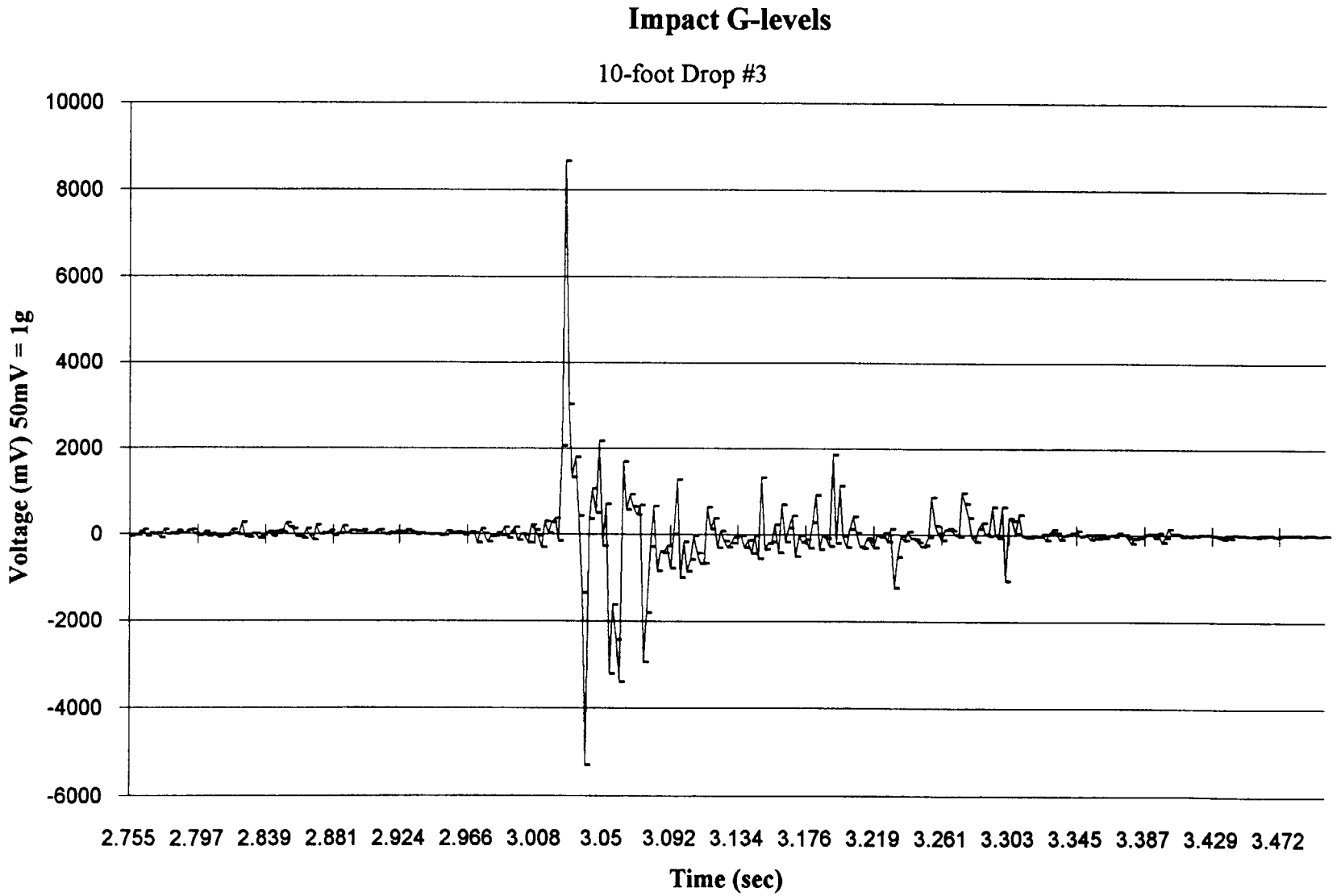
Impact G-levels
10-foot Drop #3
10000
8000
6000
4000
2000
0
-2000
-4000
-6000
Voltage (mV) 50mV = 1g
2.755 2.797 2.839 2.881 2.924 2.966 3.008 3.05 3.092 3.134 3.176 3.219 3.261 3.303 3.345 3.387 3.429 3.472
Time (sec)

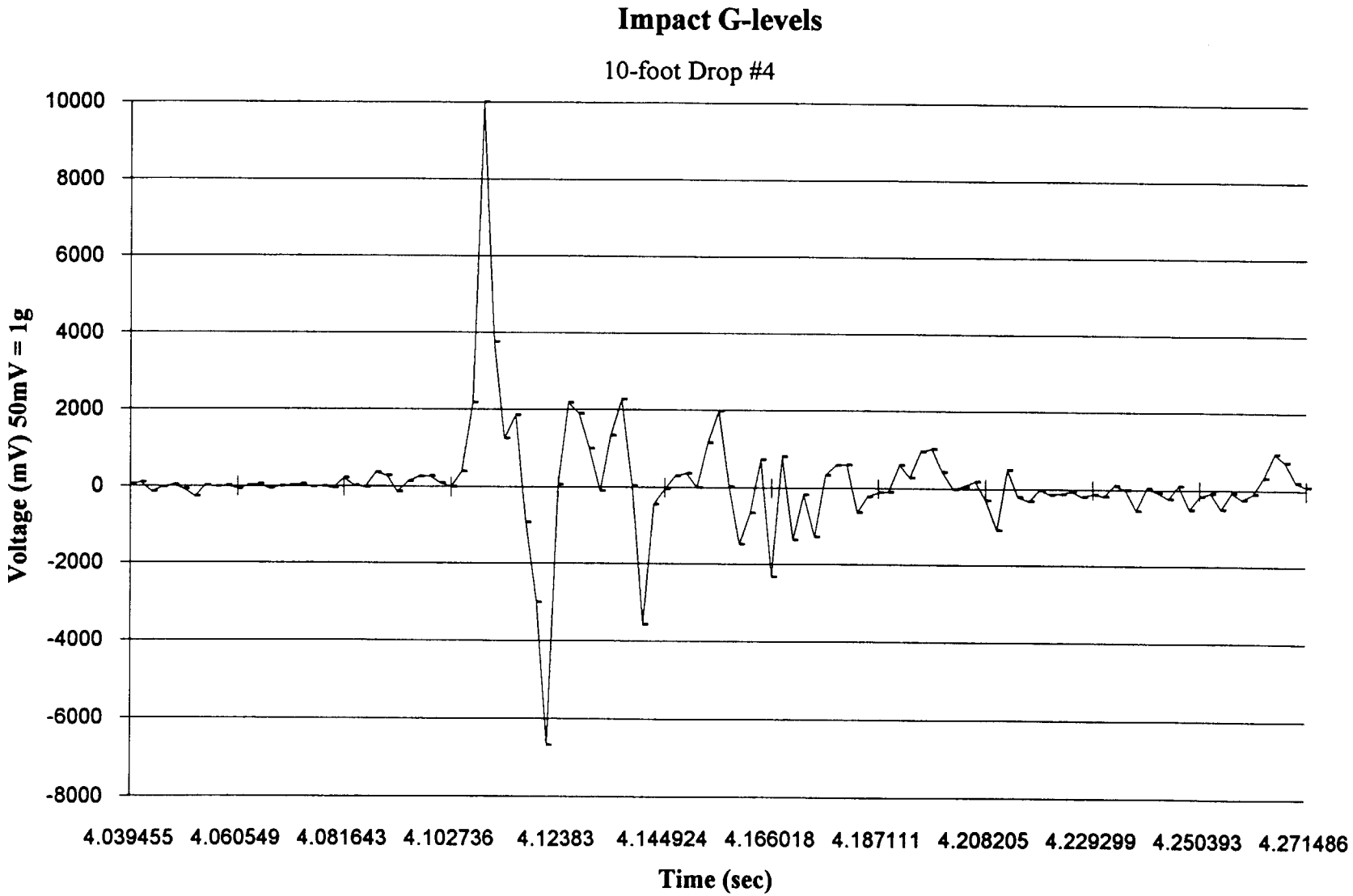
Impact G-levels
10-foot Drop #4
10000
8000
6000
4000
2000
0
-2000
-4000
-6000
-8000
Voltage (mV) 50mV = 1g
4.039455
4.060549
4.081643
4.102736
4.12383
4.144924
4.166018
4.187111
4.208205
4.229299
4.250393
4.271486
Time (sec)

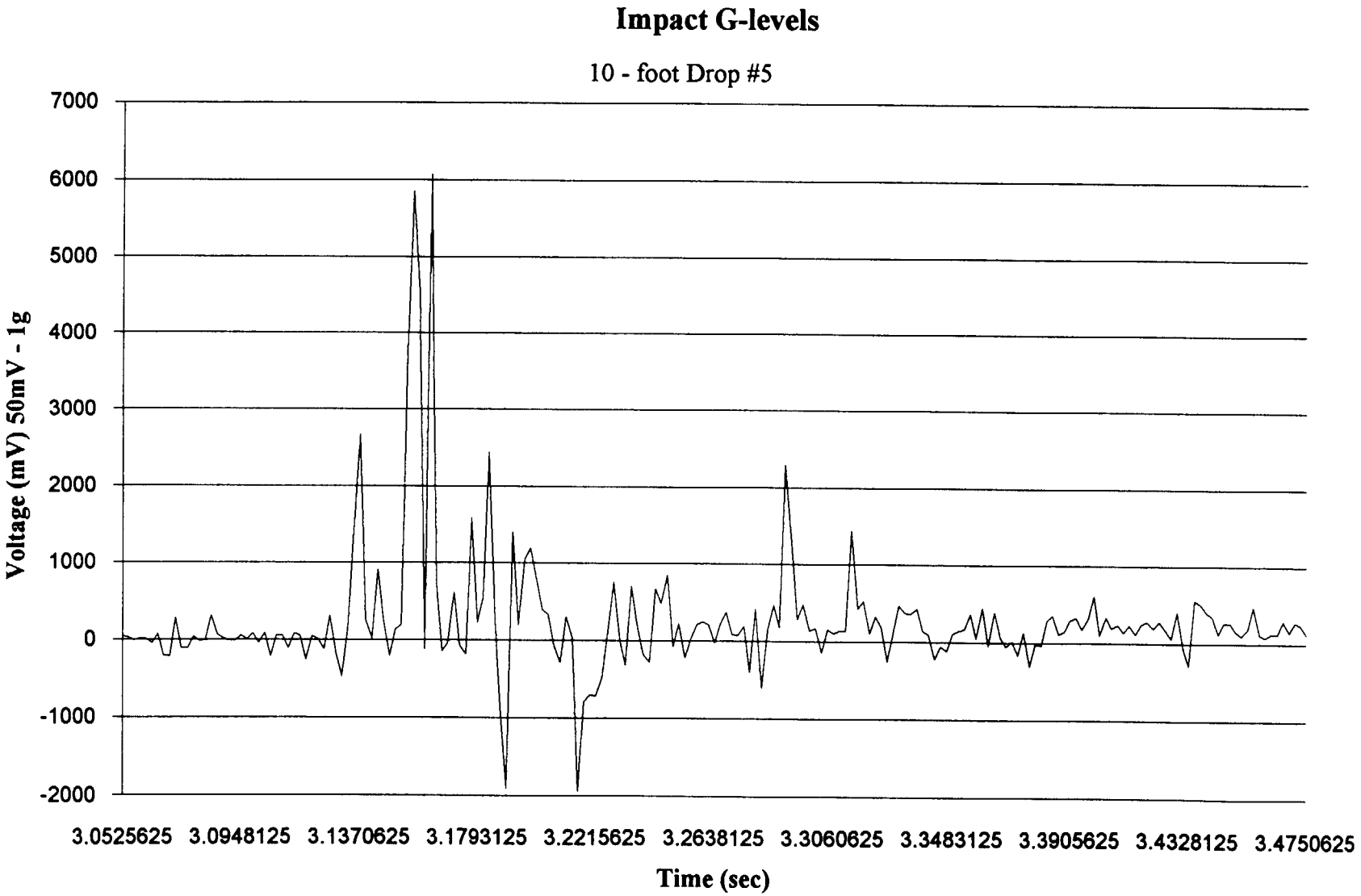
Impact G-levels
10 - foot Drop #5
7000
6000
5000
4000
3000
2000
1000
0
-1000
-2000
Voltage (mV) 50mV - 1g
3.0525625
3.0948125
3.1370625
3.1793125
3.2215625
3.2638125
3.3060625
3.3483125
3.3905625
3.4328125
3.4750625
Time (sec)

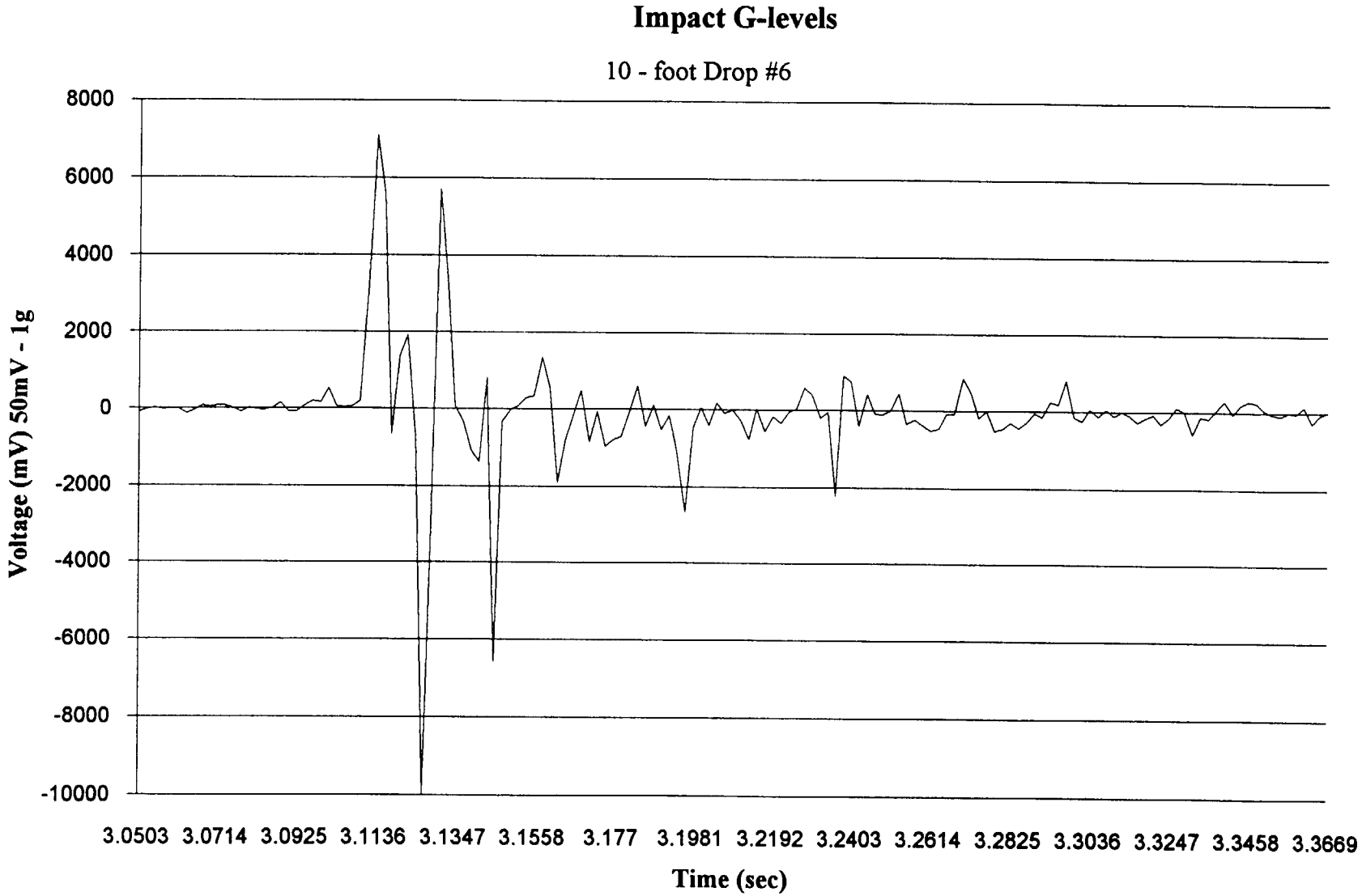
Impact G-levels
10 - foot Drop #6
8000
6000
4000
2000
0
-2000
-4000
-6000
-8000
-10000
Voltage (mV) 50mV - 1g
3.0503
3.0714
3.0925
3.1136
3.1347
3.1558
3.177
3.1981
3.2192
3.2403
3.2614
3.2825
3.3036
3.3247
3.3458
3.3669
Time (sec)

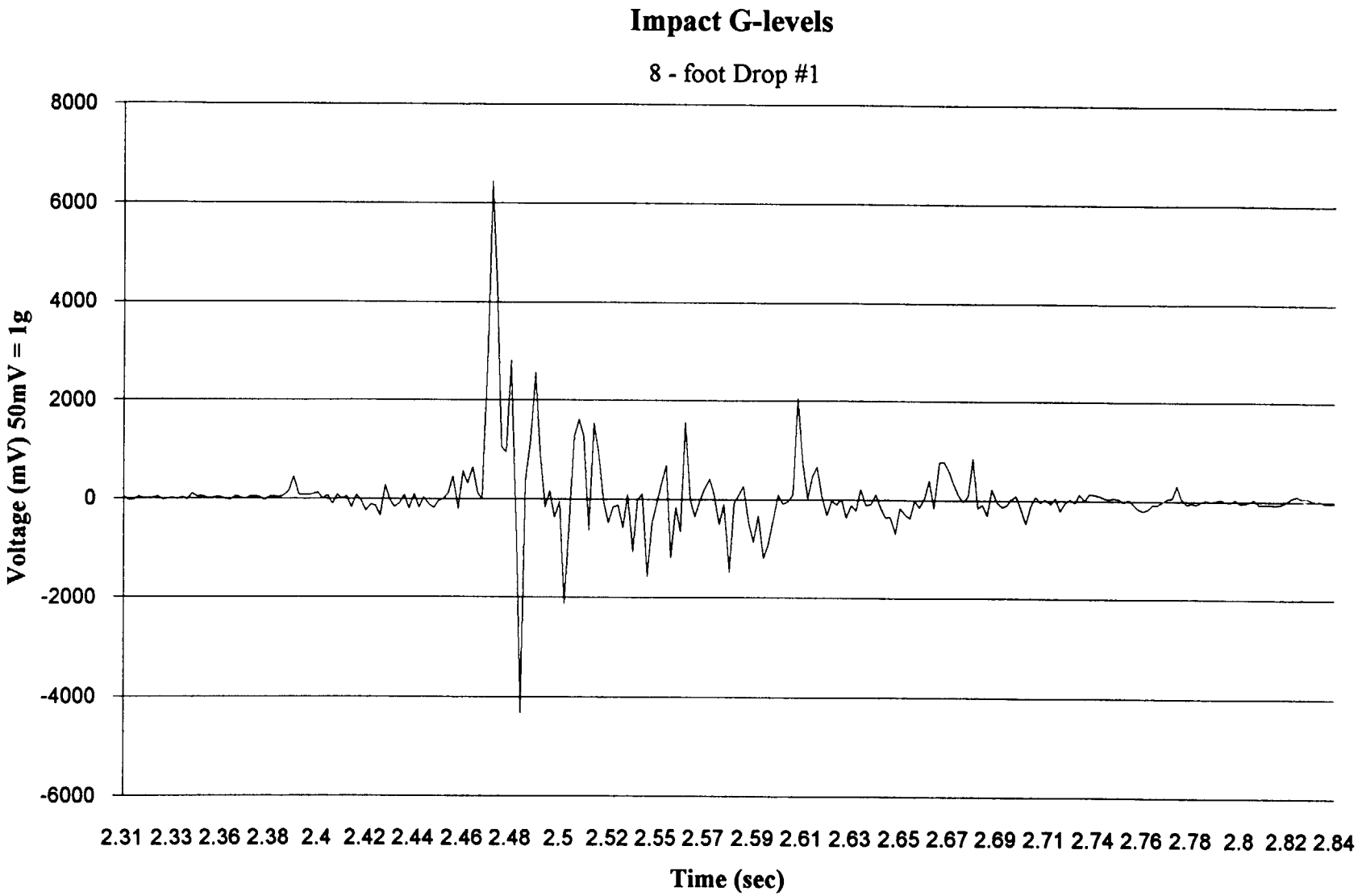
Impact G-levels
8 - foot Drop #1
8000
6000
4000
2000
0
-2000
-4000
-6000
Voltage (mV) 50mV = 1g
2.31 2.33 2.36 2.38 2.4 2.42 2.44 2.46 2.48 2.5 2.52 2.55 2.57 2.59 2.61 2.63 2.65 2.67 2.69 2.71 2.74 2.76 2.78 2.8 2.82 2.84
Time (sec)

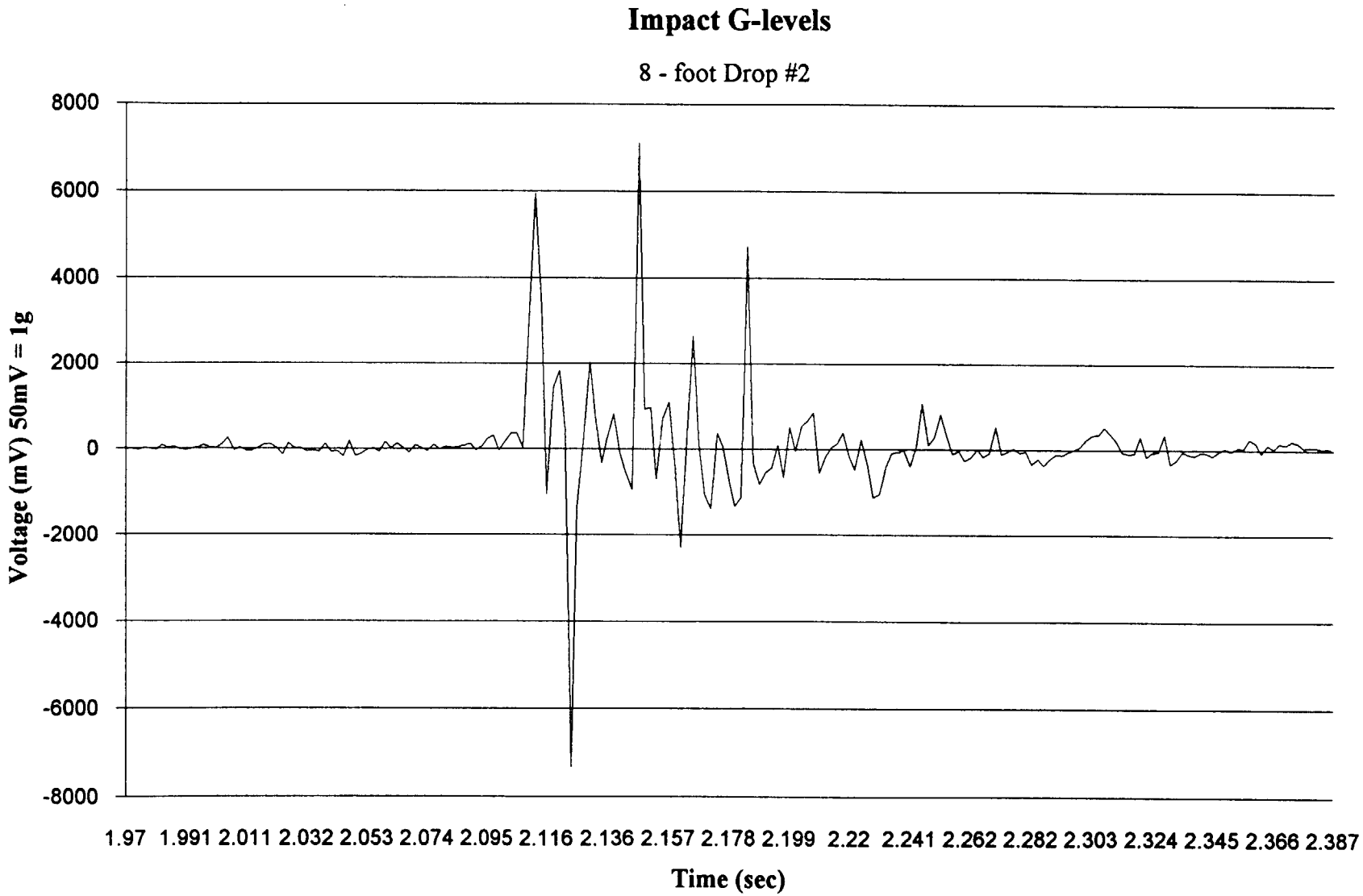
Impact G-levels
8 - foot Drop #2
8000
6000
4000
2000
0
-2000
-4000
-6000
-8000
Voltage (mV) 50mV = 1g
1.97 1.991 2.011 2.032 2.053 2.074 2.095 2.116 2.136 2.157 2.178 2.199 2.22 2.241 2.262 2.282 2.303 2.324 2.345 2.366 2.387
Time (sec)

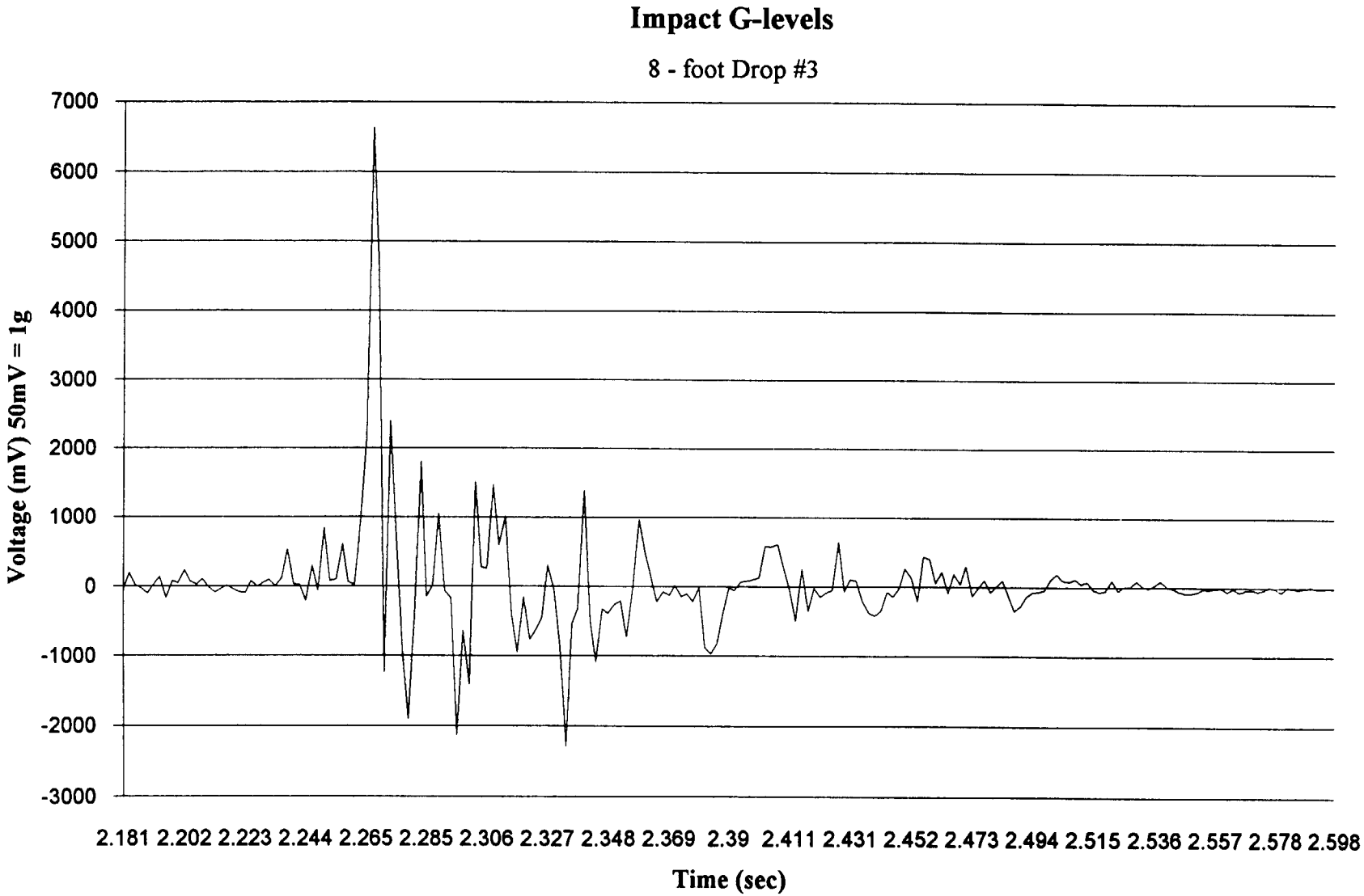
Impact G-levels
8 - foot Drop #3
Voltage (mV) 50mV = 1g
7000
6000
5000
4000
3000
2000
1000
0
-1000
-2000
-3000
2.181 2.202 2.223 2.244 2.265 2.285 2.306 2.327 2.348 2.369 2.39 2.411 2.431 2.452 2.473 2.494 2.515 2.536 2.557 2.578 2.598
Time (sec)

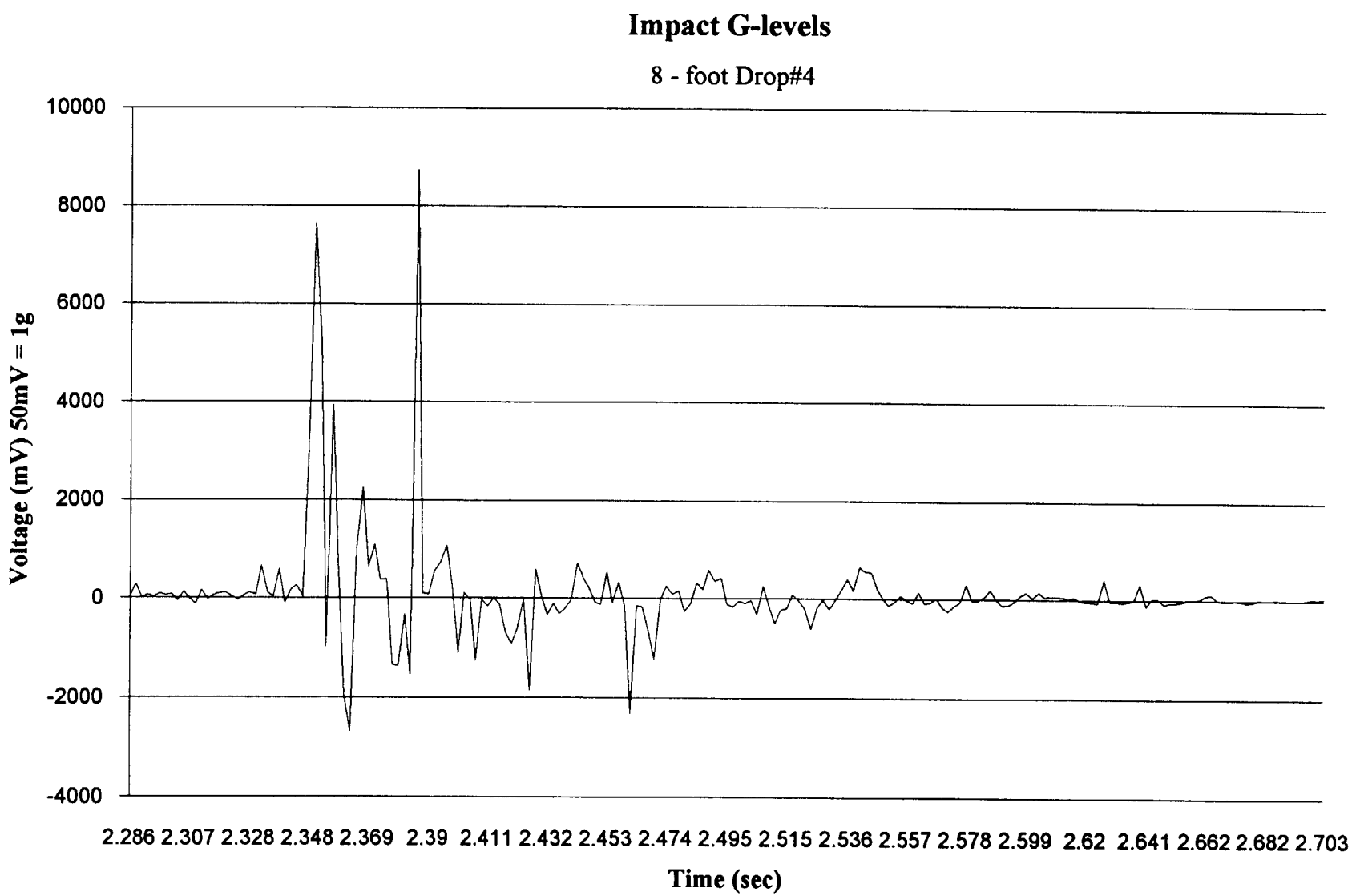
Impact G-levels
8 - foot Drop#4
10000
8000
6000
4000
2000
0
-2000
-4000
Voltage (mV) 50mV = 1g
2.286 2.307 2.328 2.348 2.369 2.39 2.411 2.432 2.453 2.474 2.495 2.515 2.536 2.557 2.578 2.599 2.62 2.641 2.662 2.682 2.703
Time (sec)

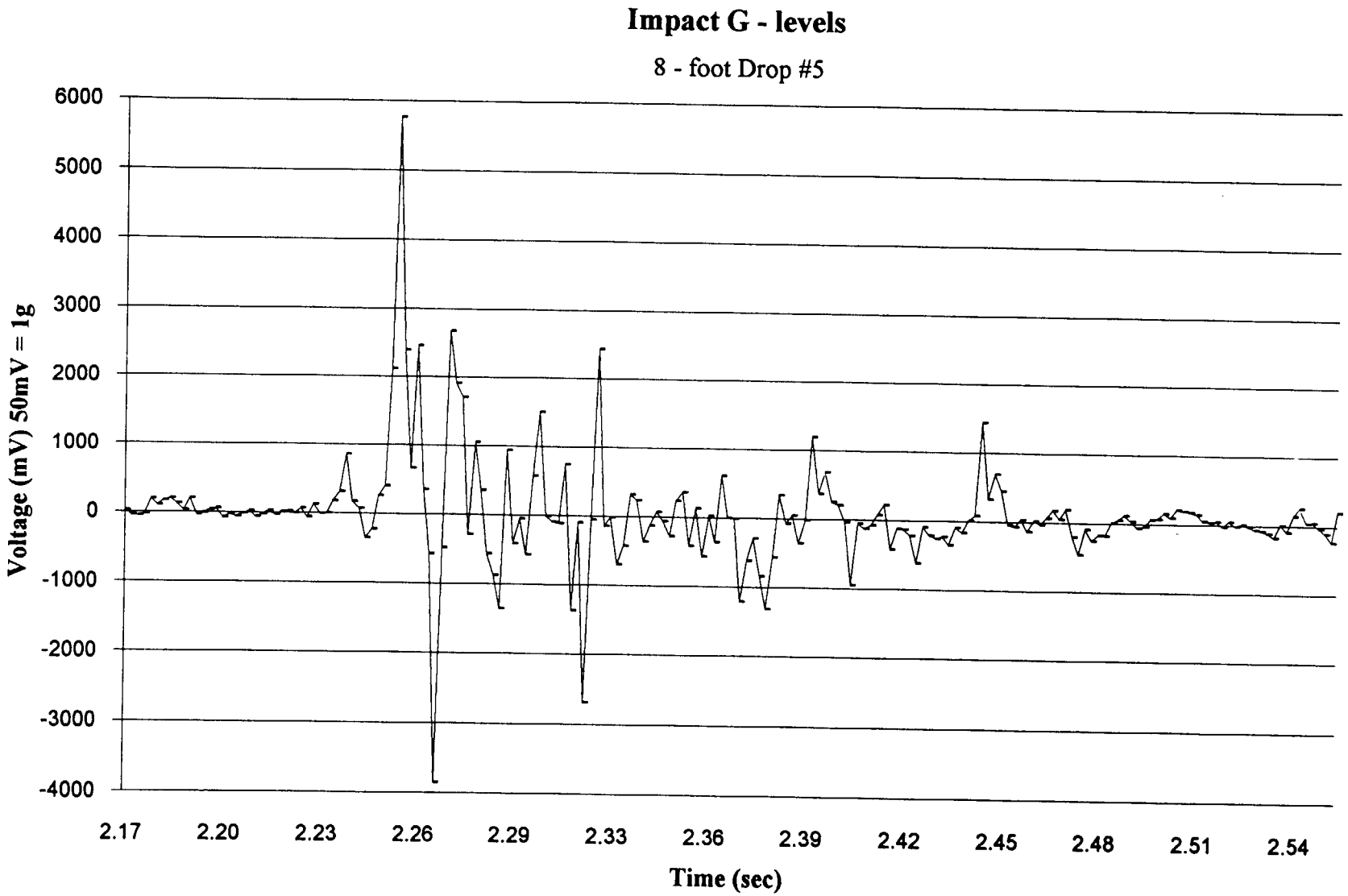
Impact G - levels
8 - foot Drop #5
Voltage (mV) 50mV = 1g
6000
5000
4000
3000
2000
1000
0
-1000
-2000
-3000
-4000
2.17
2.20
2.23
2.26
2.29
2.33
2.36
2.39
2.42
2.45
2.48
2.51
2.54
Time (sec)

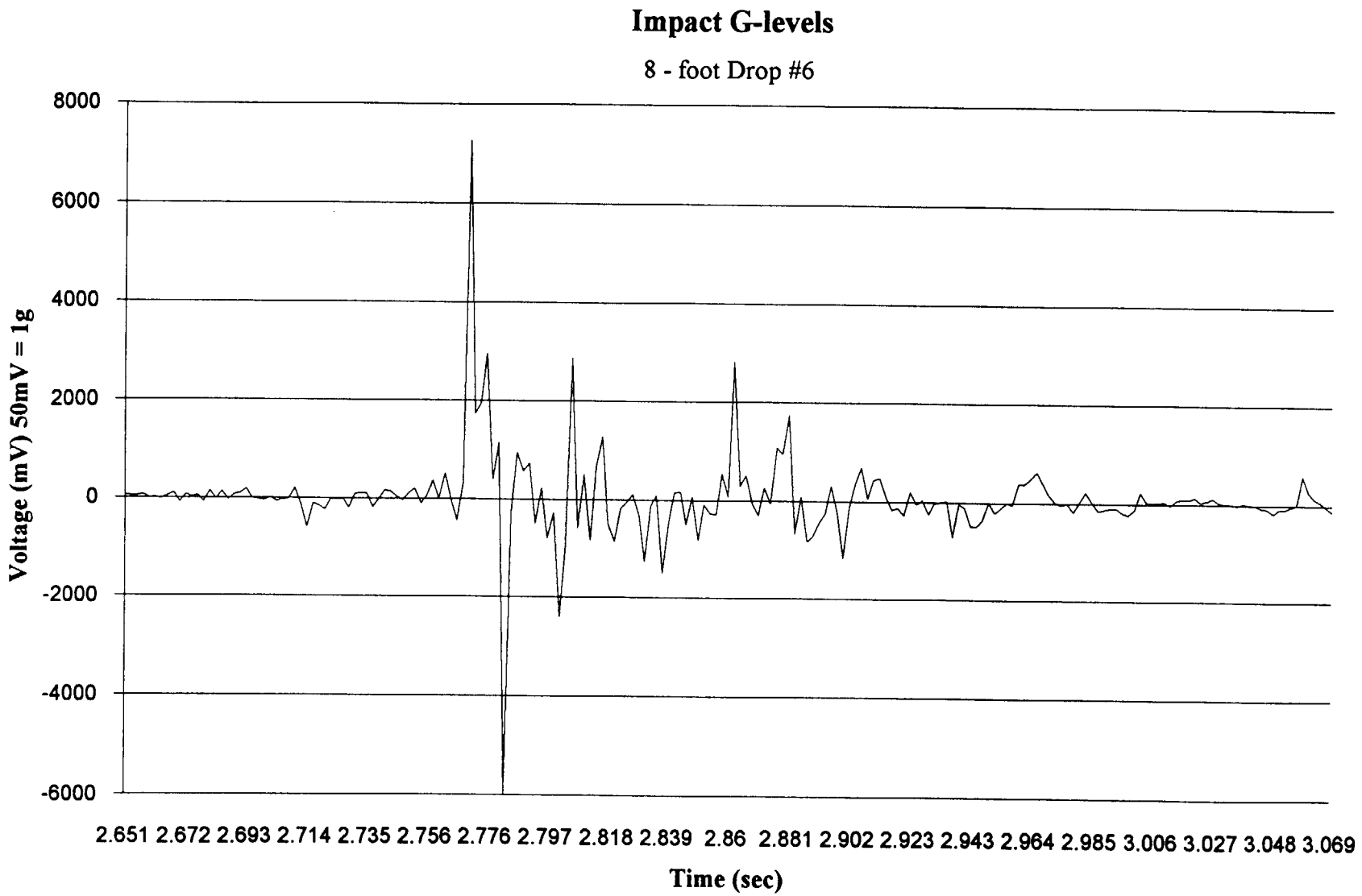
Impact G-levels
8 - foot Drop #6
8000
6000
4000
2000
0
-2000
-4000
-6000
Voltage (mV) 50mV = 1g
2.651 2.672 2.693 2.714 2.735 2.756 2.776 2.797 2.818 2.839 2.86 2.881 2.902 2.923 2.943 2.964 2.985 3.006 3.027 3.048 3.069
Time (sec)

APPENDIX G

Drop Tower Assembly Manual

Assembly Procedures

1. Place Base Plate in desired location for tower demonstration.

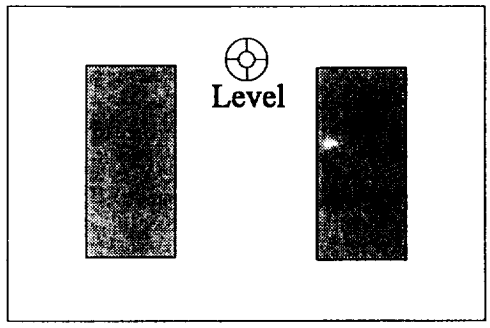

Base Plate

2. Level the base by adjusting the four rubber feet.
3. Locate two 4-foot support pole sections. They are connected by an angular support and the ends are not swaged.

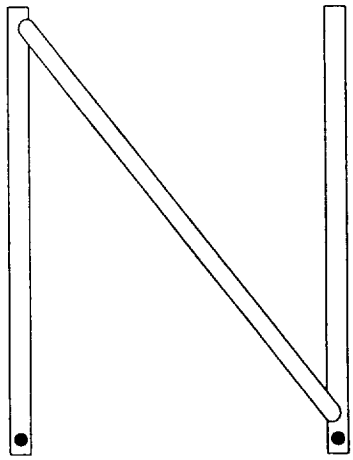

Support Poles and Angle Bracket

4. Spread the poles apart so that they are able to slide onto two pins at the rear of the base plate. The bottom of each support pole will have a drilled hole that corresponds to a hole in each pin.
5. Slide the poles onto the two pins. The angle bracket should face away from the center of the tower.

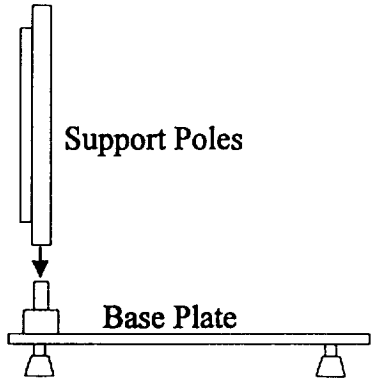

Base Plate and Support Pole Assembly

6. Align the holes in the Support Poles with the holes in the pins and insert a threaded bolt, securing it with a wing nut.
7. Locate the triangular top plate and lay it on the floor with the two pins and pulley facing up.

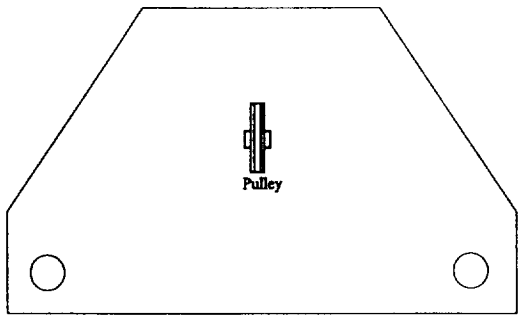

Top Plate

8. Locate the other 4-foot support pole sections. These will also be connected with an angular bracket, but the bottom of each pole will be swaged.
9. Spread this set of poles apart and slide the unswaged ends onto the pins that are mounted on the top plate. The angular support should face away from the plate.
10. Take the top plate and support pole assembly and slide the swaged ends of the support poles into the poles attached to the base plate.

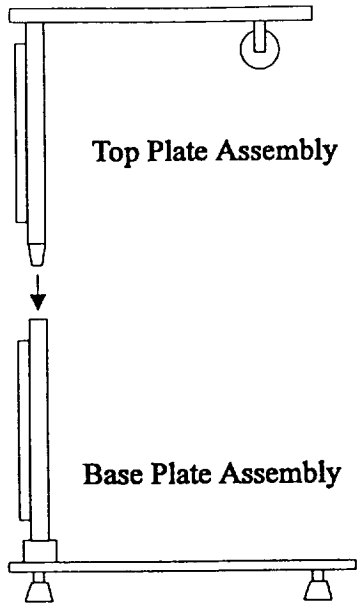

Top Plate and Base Plate Assembly

11. Align the holes in the joint of the support poles and insert a locking key. This will ensure that both poles are equal in height.

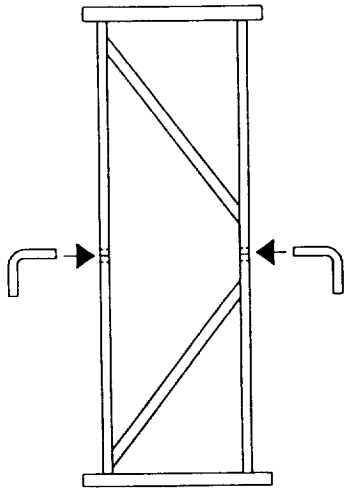

Insertion of locking pins into tower

12. Locate all of the pieces that will form the side angle braces, pictured below:

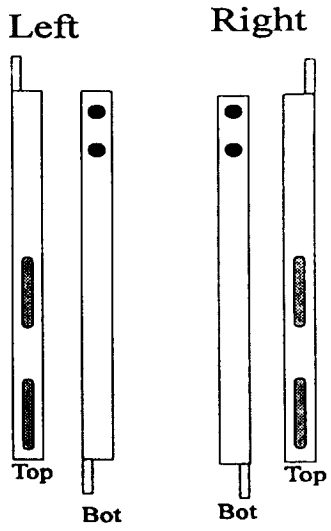

Side Angle Braces

13. To assemble the side braces, align the holes in the bottom piece with the milled groove in the top angle bracket and slide a screw through the milled slot, tightening it into the tapped holes on the bottom piece. An example of how to assembly the left support is given below:

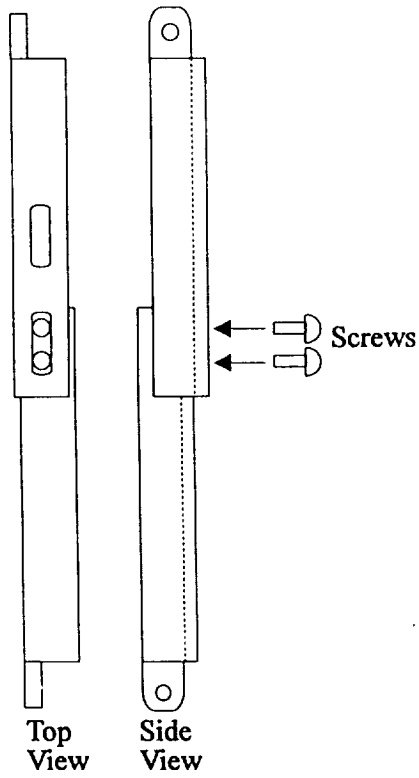

Construction of Side Angle Braces

14. Once the brackets have been assembled, they can be attached to the tower. The brace's bottom attaches to a small mount at the front of the base plate, while the brace's top attaches to a pre-drilled hole in the support poles.
15. Locate one 4-foot piece of the solid steel shaft. Screw it into the base's center block with a set screw.
16. Slide the temper-foam padding to the bottom of the shaft.
17. Place the drag shield and payload assembly onto the shaft and allow it slide to the bottom.

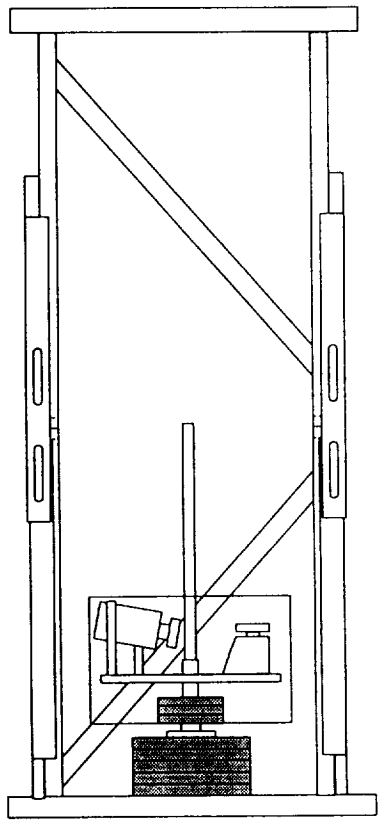

Drop Tower with Drag Shield and Experimental Platform

18. Locate the other 4-foot section of the steel shaft. Place set screws in both ends. Running one set screw through the hole in the top plate, screw the other end into the other shaft section. Once the shaft has been securely attached, screw a wing nut onto the top of the shaft, securing it to the top plate.

19. Run a rope through the pulley, and connect it to the hook on the experimental platform.
20. It is now possible to drop payloads.

NOTE:

To construct the ten or twelve foot sections, follow the same procedures, except in step 9, insert additional support trusses, and in step 18, insert additional shaft segments.

SECTION 2

COMPARATIVE SOOT DIAGNOSTICS EXPERIMENT DESIGN

by

Laurence J. Dallaire

Prepared, in part, as a Major Qualifying Project in
Mechanical Engineering Department
Worcester Polytechnic Institute
1993-94

Table Of Contents

Acknowledgments

I would like to thank the following people influence and support throughout this project:
Dr. David L. Urban, NASA Mentor
Prof. Vahid Motevalli, WPI Project Advisor
Dr. Howard Ross, WPI-NASA Project Coordinator

I would also like to thank the following people for their assistance:
Dr. Howard Pearlman
Jeff Goldmeer
Rick Smith
T. J. Marsden
Mike Pereira
Chris Toth
The entire Microgravity Combustion Group at LeRC

List of Figures

List of Tables

Chapter 1. Introduction

1.1 Background

Research into how fluids behave in micro gravity has been of interest since the beginning of the space program. Through the use of sounding rockets, airplanes, and drop towers such as the ones found at NASA's Lewis Research Center and Marshall Space Flight Center, scientists and engineers have been able to study the effects of micro gravity for very short periods of time. (NASA First U.S. Microgravity Laboratory, 1992) Drop towers may provide 2.2 or 5 seconds of low gravity, NASA planes flying a parabolic trajectory provide approximately 20 seconds, and sounding rockets provide about 15 minutes. (NASA Annual Report, 1992)

The first real opportunity to perform micro gravity research for extended periods of time came during the Apollo Program. While Mercury and Gemini allowed practical experience in the technical aspects of space flight, Apollo was the first to allow experiments in the fluid and materials science. Apollo later led to the Apollo-Soyuz test project and America's first space station, Skylab. (NASA First U.S. Microgravity Laboratory, 1992)

Advances in space flight capabilities and experimentation have taken place. These complexities, combined with the extended durations of missions, have increased risk of fires occurring in space. Thus, there is a greater need to develop fire safety measures in space.

Many approaches to fire safety in space applications have been taken over the years. The Space shuttle uses nine ionization type smoke detectors placed in its environmental control and life support system (ECLSS) ducts. (Friedman & Sacksteder, 1988) In an ionization detector, smoke particles enter a space between two electrodes, reducing ion mobility and causing a reduction

a space between two electrodes, reducing ion mobility and causing a reduction in current flow between them. (Custer & Bright, 1974) These smoke detectors each have an internal fan to increase airflow and improve reliability. These fans, and the location of the detectors inside air ducts, are designed to compensate for the fact that there is little or no natural convection to transport smoke in micro gravity. (Friedman & Sacksteder, 1988)

Plans for Space Station Freedom call for several photoelectric smoke detectors. These detectors operate using both light scattering and light obscuration principles. A beam of light is emitted from an LED and reflected back by a pair of mirrors. The returning beam of light is then checked by photocells for both the amount of obscuration and the amount of light scattered by smoke particles.

1.2 Motivation

Testing smoke detectors is important to help quantify the effectiveness of fire detection measures aboard both the Space Shuttle and Space Station Freedom. In order to test these smoke detectors, a special apparatus must be designed. The test apparatus designed in this project will be used for tests on earth, in the learjet, and finally on the next Spacelab mission as part of a Glovebox experiment. These tests will be used to compare the performance of both types of smoke detectors and detection characteristics of differing materials to be heated in different levels of gravity.

The Spacelab Glovebox is provided by the European Space Agency to enable crew members to handle materials that otherwise would have been impractical on an open Spacelab due to contamination of both experiment and Spacelab atmosphere. The facility has a closed area that prevents

contamination in the rest of the Spacelab facility. (NASA First US Microgravity Laboratory, 1992)

Chapter 2. Project Goals

2.1 Objective

The objective of this project was to design test samples and a holder to be used in the Comparative Soot Diagnostics Experiment that is part of the Glovebox program. The Comparative Soot Diagnostics Experiment will be used to test the ionization detectors currently in use on the Space Shuttles and those planned for use on Space Station Freedom. It will compare each type of detector's performance to both smoldering and pre combustion particles.

2.2 Design Specifications

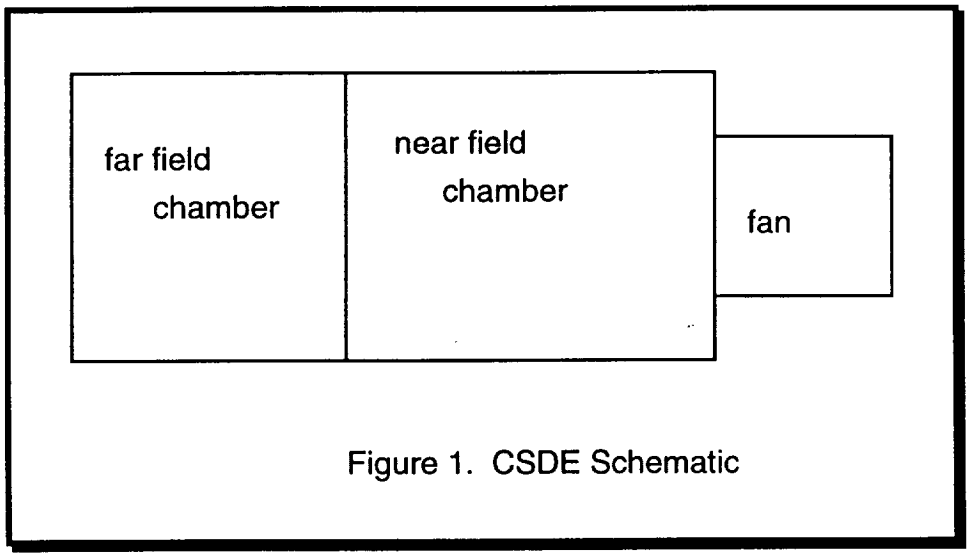

Figure 1. CSDE Schematic

The Comparative Soot Diagnostics Experiment (CSDE) consists of three parts: the fuel frame, the far field sub-assembly, and the near field sub-assembly. The near field sub-assembly consists of a sampling chamber containing the fuel frame downstream from a fan. This fan has a variable airflow

that may be set from 1 - 5 $^{cm}/_{sec}$. The interior cross sectional area of this section is 9,216 cm^2. The fan can supply a mass flow of between 10.86 and 54.3 $^{g}/_{sec}$ (See appendix C for the complete solution). Connected to it are two lasers, one upstream of the fuel frame and one downstream. These lasers will be used to measure mass loss and particle sizes given off by the burning sample.

The far field sub-assembly lies downstream of the near field sub assembly. It contains the Space Shuttle and Space Station Freedom smoke detectors that will be evaluated.

The fuel frame lies inside the near field sub-assembly. This piece will hold any samples that are to be heated. It is made of black Teflon, so it will not conduct electricity if wires are mounted to it. (See Figure 2.) The two fuel samples to be used in the CSDE are silicone rubber and Teflon wire insulation. Silicone rubber comes in a 2.2 mm thick rolled sheet. It must be cut into small strips to be tested. The Teflon wire is a 20 gauge wire that is 1.5 mm in diameter. It, too, must be cut to a small size in order to be tested.

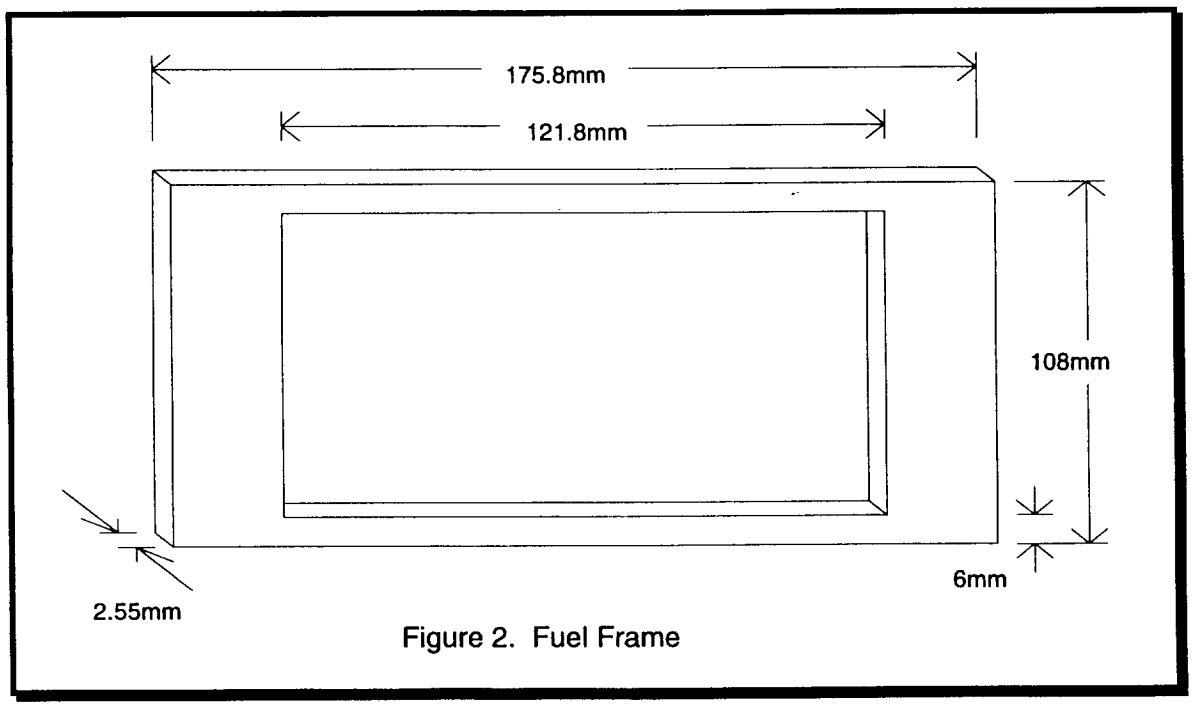

Figure 2. Fuel Frame

The design requirements are as follows:

- Must pyrolyze both a silicone rubber sample and a Teflon coated wire sample.
- Each sample must be heated to two different temperatures: one low to produce small, pre-combustion particles, and one high to produce larger, smoldering particles.
- Samples must generate particle loading of approximately 2 parts per million (ppm) by mass at the detectors (2 μg smoke per 1 g of air). This particle loading can be generated by achieving a mass loss rate of about 22 $\mu g/_{sec}$ in the sample in an air flow of 1 $^{cm}/_{sec}$. (See appendix C for sample calculations.)
- Test apparatus must fit into an existing fuel frame and test box.
- Heating element must require no more than 5V, 4A.
- Final apparatus must be made so that an astronaut can easily activate it.

Chapter 3. Procedure

3.1 Heating Characteristics of Various Wires

Temperature as a function of current in a bare heating wire had to be determined analytically and then verified experimentally. Various types of heating wires were found and their resistance per length was determined from the manufacturers' technical manuals. Types of wires considered and their resistances are listed in Table 1.

Table 1. Properties of Various Wire Types

Wire Type	Composition	Manufacturer's Resistance ($\Omega/_{cm}$)	Measured Resistance ($\Omega/_{cm}$)
20 gauge Nickel-Chromium	60% nickel 40% chromium	0.0208	--
22 gauge Nickel-Chromium	60% nickel 40% chromium	0.0361	--
24 gauge Nickel-Chromium	60% nickel 40% chromium	0.0528	--
26 gauge Nickel-Chromium	60% nickel 40% chromium	0.0844	--
30 gauge Kanthal	72.7% iron 22% chromium 5.3% aluminum	0.274	0.32

A very flexible heating element with a high resistance per unit length was desired. Kanthal fit this parameter far better than any other wire type considered, so other types of wire were excluded at this point. Actual resistance per length was later found experimentally during heating experiments of sample

materials.

The experimental setup consisted of a variable voltage power supply, a digital multimeter, thermocouples, and the different types of wire. (See Figure 3.)

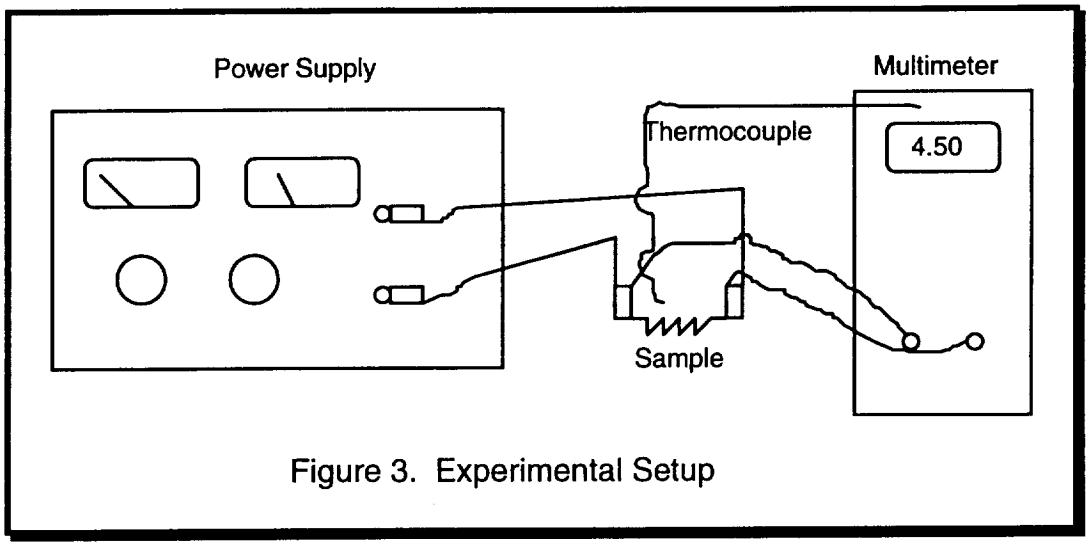

Figure 3. Experimental Setup

The power supply was first set to 5 V, the maximum level available from the Glovebox. Wires were then checked for temperatures at different currents. Melting temperatures for the 2 different alloys were also found. Kanthal will melt at about 1500^{o}C at 4 A.

3.2 Burning Characteristics of Samples

The first step in designing an apparatus to test smoke detectors was to find a sample size and temperature that would produce the desired particle loading of approximately 2 ppm by mass. There are several steps that must be taken to accomplish this.

Temperatures and heating rates to begin smoldering and pre combustion tests were estimated first. These temperatures were based chosen to be high enough to produce a mass loss, but low enough so that the experiment could be

controlled. The required temperature to begin testing for Teflon was estimated to be 300 - 400 ^{o}C. The temperature to begin testing for silicone rubber was estimated at 250 - 350 ^{o}C. These temperatures were arrived at based on previous experience with combustion experiments.

At this point in the project, all nickel-chromium alloys were ruled out of consideration for use as a heating wire. They could not generate enough heat per amp of current (550^{o}C @ 4 A in the smallest diameter). In addition, Kanthal was a much easier material to work with. The readily available diameter of 0.01" made it very easy to wrap around test samples.

The actual value for the resistance per unit length was then found for Kanthal heating wires. Several 10 cm lengths of Kanthal wire were cut and a 4.5 V potential was applied across them. The current passing through the wire, measured with a digital multimeter, was determined to be 1.4 A. Ohm's law was used to determine the resistance of the wire. This resistance was then divided by the length to determine resistance per unit length. The resulting value was determined to be 0.32 $\Omega/_{cm}$. A complete solution can be found in Appendix C.c.

Next, a model of the actual power supply was put together. This variable voltage supply had to be calibrated and its performance evaluated. It was found that this power supply only delivered 4.8 V at the alligator clips due to losses in the system. 5 V were applied at the input, 4.9 V were measured at the output, and 4.8 V were measured at the clips.

A problem was found initially in the power supply. At voltages less than 4.4 V at the alligator clips, the voltage would climb. The lower the voltage, the faster the climb. It would finally rest at about 4.7 V. This problem can be attributed to the transient heat dissipation in the system. It was solved by continuously monitoring and adjusting the output voltage of the circuit. Flight hardware will be more able to dissipate heat, so rising voltage is not anticipated.

The temperature as a function of current found in step two was used as a starting temperature for finding actual pre-combustion and smoldering characteristics of the two materials. The materials were heated under a hood using the same equipment as described in section 3.1 to determine temperature and heating rates of the materials. The major goal of this step was to determine the amount of contact between the wire and the sample to provide a satisfactory mass loss rate. This was done by weighing a sample, heating it for a timed interval, and then weighing it again. The balance used for weighing the samples was electronic and had a resolution of 0.01 mg. The total mass loss was divided by experiment duration to determine mass loss rate. Ten repetitions were done for each sample. The average of all ten repetitions was taken as the final result of the experiment. Final results were achieved by trial and error.

3.3 Method of Heating

In order to heat silicone rubber to generate small particles was a 7.5 cm heating wire wrapped around a sample of roughly 2.2 mm x 2.2 mm square cross section. The wire was wrapped in $5^1/_2$ turns around the sample with the turns spaced roughly 5 per cm of sample length.

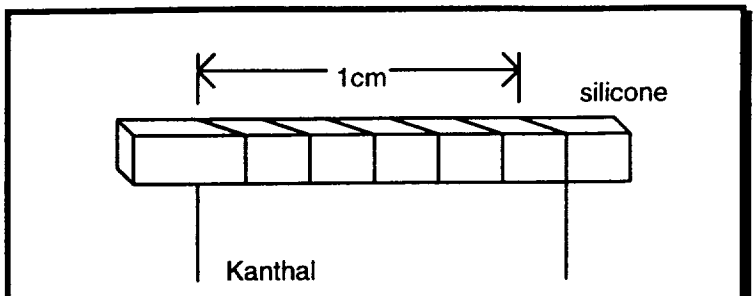

Figure 4. Low Temperature Test of Silicone

Teflon had to be heated to a higher temperature than silicone to attain an adequate mass loss rate. The geometry necessary to obtain 2 ppm smoke concentration was achieved by wrapping a 7 cm section of Kanthal wire around a piece of Teflon wire in $9^1/_2$ turns spaced 4 per centimeter. The sample length was 3 cm.

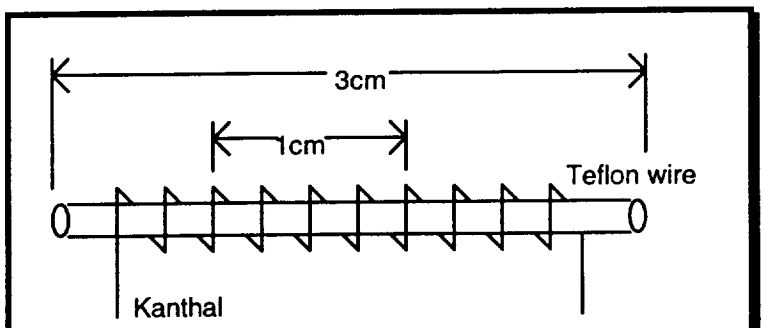

Figure 5. Low Temperature Test of Teflon

In order to obtain large particles from Teflon, samples had to be heated to a peak temperature of approximately 600 ^{o}C. This was achieved by coiling a 5 cm section of Kanthal around the sample one time only. Sample length did not seem to affect the results of high temperature tests of Teflon, which were the most easily repeatable in the entire project. (See appendix B.) This was probably because the narrow contact geometry allowed the Teflon wire to dissipate heat as an infinite fin at a relatively short (about 2 cm) length. The samples had to be bent during testing, however, to prevent the sample from

The samples had to be bent during testing, however, to prevent the sample from sliding down the heating wire. This would add an unnecessary source of error to this experiment by allowing a larger area of Teflon to be heated.

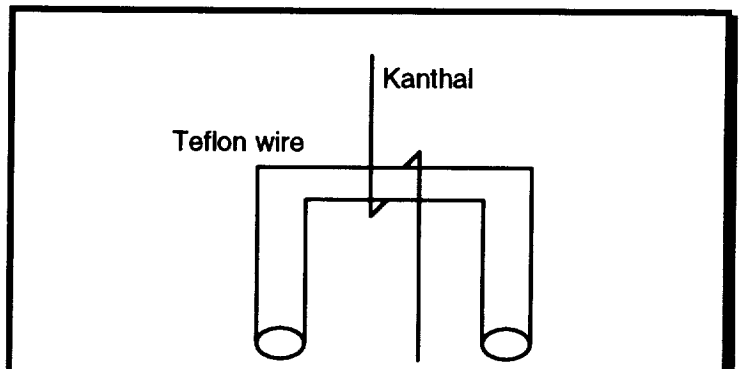

Figure 6. High Temperature Test of Teflon

High temperatures were achieved in silicone samples by wrapping a 5 cm length of Kanthal around a sample in a single coil.

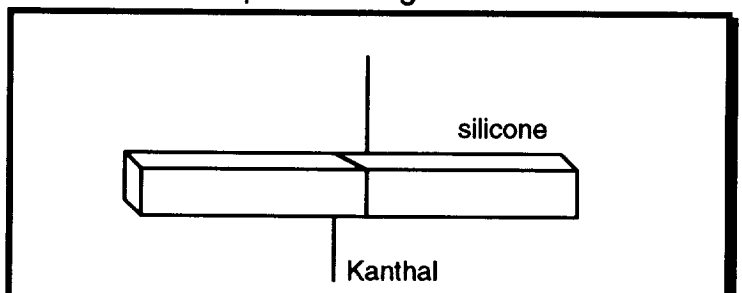

Figure 7. High Temperature Test of Silicone

Temperatures in all samples were measured using thermocouples. The heads of the thermocouples were placed in close proximity to both the heating wire and the sample so that temperatures could be measured as accurately as possible.

Chapter 4. Results

4.1 Experimental Results

At lower temperatures, both silicone and Teflon showed no visible smoke or residue. It appeared that all samples softened and slightly melted, leaving grooves where the heating wire had been in contact with the sample. At higher temperatures, both samples showed visible signs of charring. In Teflon, very faint smoke could be seen at 580 ^{o}C if the sample was examined closely during heating. After heating was finished, slight discoloration and residue could be seen on the sample. At about 450 ^{o}C, it turned to ash and large amounts of smoke were visible.

4.1.1 Low Temperature Test of Silicone Rubber

A voltage of 3V was applied across the Kanthal wire, resulting in a current of 1.3A. Power was 3.9 W. The calculated current was 1.25 A, very close to the experimental (See appendix C.d for calculations.) The sample was then heated for 60 seconds. During heating, the sample temperature rose slowly until it reached a peak temperature of 350^{o}C. It was weighed again to determine the mass lost while heated. Mass loss was then divided by the time to determine the mass loss rate. The final mass loss rate achieved in this experiment was $22^{\mu g}/_{sec}$ with a standard deviation of $5.83^{\mu g}/_{sec}$. A summary of this data can be found in Appendix B.

4.1.2 Low Temperature Test of Teflon Wire

A problem was encountered during testing concerning the repeatability of the experiments. It was found that the length of the sample wire must be held constant in order to maintain the same mass loss rate for a given voltage. This was found to be caused by the Teflon sample acting as a heat sink or fin. Longer sample wires heated up slower to a lower temperature than shorter ones. This phenomenon was not encountered in the silicone samples, probably because silicone has a much lower thermal conductivity value than Teflon. Silicone rubber has a thermal conductivity of 0.00019 $^{W}/_{mK}$, while Teflon has a value of roughly 4.5 $^{W}/_{mK}$. (Touloukian, 1970) This would allow the silicone sample to be treated as an infinite fin at a shorter length.

A 3 cm sample length was decided upon for two reasons. First, some part of the sample should protrude from the ends of the Kanthal coil in order to reduce end effects. A 3 cm sample should protrude sufficiently to allow for this. Second, long pieces of wire conduct too much heat away from the sample, causing a slower heating rate that makes mass loss rates too non-linear. While some non-linearity due to heating is unavoidable, it is desirable to minimize this effect.

A voltage of 4.35 V was applied across the Kanthal wire, resulting in a current of 1.9 A. This is very close to the expected value of 1.94 A. (See Appendix C.d for solution.) Power was 8.27 W through the entire length of Kanthal. The sample was then heated for 60 seconds. During heating, the sample heated slowly until it reached a peak temperature of 470 ^{o}C. The final mass loss rate achieved in this experiment was 20 $^{\mu g}/_{sec}$ with a standard deviation of 5.19 $^{\mu g}/_{sec}$. A summary of the data can be found in Appendix A.

4.1.3 High Temperature Test of Teflon Wire

A voltage of 4.5 V was applied across the Kanthal wire, resulting in a current of 2.8 A. Power was 12.6 W. The expected current was 2.81 A, extremely close to the experimental value. (See Appendix C.d for solution.) The sample was then heated for 30 seconds. This shorter heating period was necessary due to the nature of the Teflon wire. At a mass loss rate of 22 $\mu g/_{sec}$, the Kanthal will melt through the Teflon insulation in about 30 - 40 seconds. At this point, there is no longer in direct contact between Kanthal and Teflon, and mass loss rate decreases. During heating, the sample temperature increased rapidly until it reached a peak temperature of 600 ^{o}C. The final mass loss rate achieved in this experiment was 23 $\mu g/_{sec}$ with a standard deviation of 2.58 $\mu g/_{sec}$. A summary of the data can be found in Appendix A.

4.1.4 High Temperature Test of Silicone Rubber

Silicone behaved much more spectacularly at high temperatures than Teflon. At about 450 ^{o}C, smoke was observed and the material began to turn to ash. This effect became more pronounced as temperature increased. Mass loss rate increased and smoke and ash formation became significant. At about 650 ^{o}C, silicone samples ignited and continued to burn on their own after the heating source was turned off. This behavior meant that the temperature of the silicone had to be kept down to avoid ignition and loss of control of the experiment.

Control was accomplished as follows: A 3.35 V potential was applied across the Kanthal wire, resulting in a current of 2.1 A. This value was fairly

close to the expected value of 2.09 A. (See Appendix C.d for solution.) This geometry produced a peak temperature of approximately 470 ^{o}C after rapid heating.

The behavior of silicone at higher temperatures resulted in a slightly higher mass loss rate in silicone rubber than in other samples. The final mass loss rate achieved in this experiment was $27^{\mu g}/_{sec}$ with a standard deviation of $8.19^{\mu g}/_{sec}$. A summary of this data can be found in Appendix A.

A summary of the data obtained in all four tests is in Table 2.

Table 2. Test Data

Sample	Mass Loss Rate	Standard Deviation
Teflon @low T	20 $\mu g/_{sec}$	5.19 $\mu g/_{sec}$
Teflon @high T	23 $\mu g/_{sec}$	2.58 $\mu g/_{sec}$
Silicone @low T	22 $\mu g/_{sec}$	5.83 $\mu g/_{sec}$
Silicone @high T	27 $\mu g/_{sec}$	8.19 $\mu g/_{sec}$

4.2 Prediction of Power Required @ $1^{cm}/_{sec}$

4.2.1 Explanation of Calculation Method

It was necessary to predict the power that will be required to generate the desired mass loss rates in a 1 $^{cm}/_{sec}$ airflow. This was attempted using a simple energy balance for each sample type. The energy balance, assuming steady state, was:

$$q_{total} = q_l + q_w + q_s \qquad \text{(Eq. 1)}$$

where q_{total} is the total heat lost from the sample and the heating wire, q_l is the heat lost by the legs of Kanthal wire leading to the sample, q_w is the heat lost by the part of the Kanthal wire not in contact with the sample, and q_s is the heat lost by the sample. See Figure 8. for a schematic.

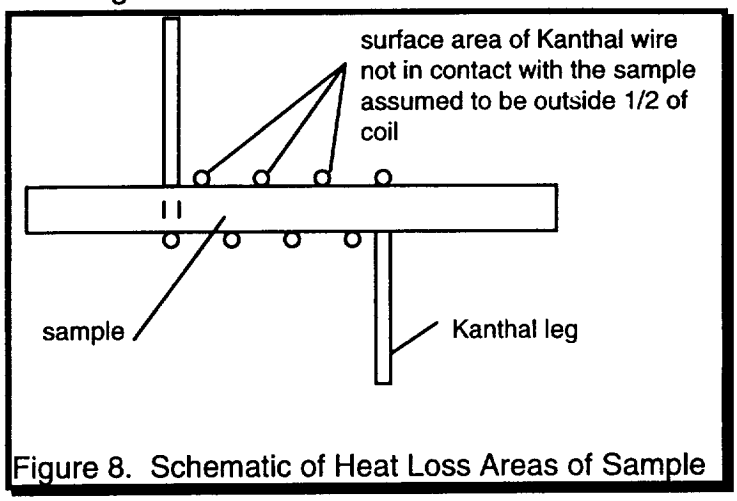

Figure 8. Schematic of Heat Loss Areas of Sample

The total heat lost should be equal to power lost through the wire. This equation was solved for $P = VI$ and the heat loss terms. The heat loss terms were:

$$q_l = h_l A_w \Delta T + \varepsilon_w A_w \sigma (T_w^4 - T_\infty^4) \qquad \text{(Eq. 2)}$$

$$q_s = h_s A_s \Delta T + \varepsilon_s A_s \sigma (T_s^4 - T_\infty^4) \qquad \text{(Eq. 3)}$$

$$q_w = \frac{h_w A_w \Delta T}{2} + \varepsilon_w \frac{A_w}{2} \sigma (T_w^4 - T_\infty^4) \qquad \text{(Eq. 4)}$$

where h_l, h_s, h_w are the convective heat transfer coefficients of the respective regions, A_w is the surface area of the Kanthal wire, ε_w is the emissivity of the Kanthal wire, σ is the Boltzman constant, T_w is the temperature of the Kanthal wire, T_∞ is the ambient temperature, A_s is the surface area of the sample, ε_s is the emissivity of the sample, and T_s is the temperature of the sample. The heat

transfer coefficient, h must be calculated separately for each heat loss term because Reynold's numbers will be different for each. Reynold's number will vary not only because of changing velocity, but also because of changing geometries from region to region on a sample.

The method of calculation was to use an analytical relationship to solve for the heat lost at all known air velocities. The analytical relationship was then used to predict heat losses at several other velocities in order to generate a plot of air velocity versus heat loss. The analytical relationships used were found in Holman, 1990. All calculations were done using software by MathSoft, Inc. Sample calculations for each test at 50 $^{cm}/_{sec}$ may be found in Appendices B.a through B.d. These curves of predicted heat loss were then compared to measured values of power through the experimental sample. These plots may be found in Figures 9 through 12.

4.2.2 Comparison of Calculations vs. Observations in Teflon at Low Temperature

In the plot of Teflon at low temperature, the two sets of data can be seen to diverge as air flow decreases. See Figure 9. Calculated heat loss is only 5% lower than the measured value at 50 $^{cm}/_{sec}$, but the difference grows to 29% at 15 $^{cm}/_{sec}$. The analytical relationship predicted a value for heat loss that is very close to the measured power through the system. This divergence at lower airflows negates the possibility of predicting needed power at these lower air velocities. This prediction, while probably too low, was 3.66 W. There are tow possible reasons for this divergence. Either the analytical relationship needs to

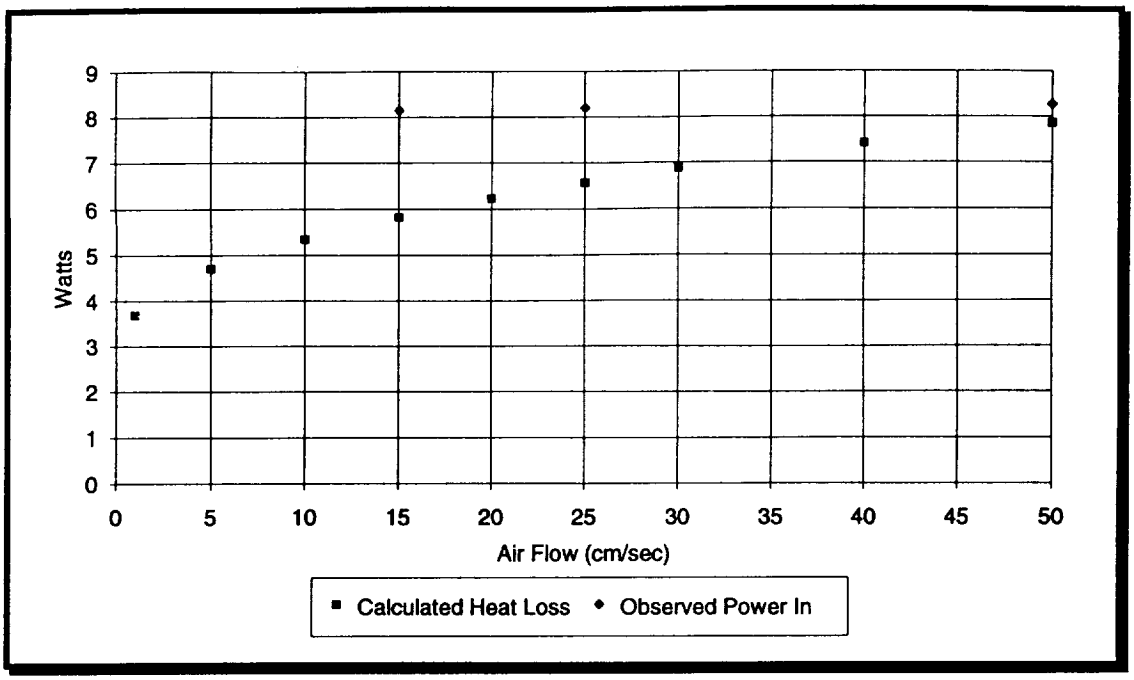

Figure 9. Calculated vs. Observed Heat Loss in Teflon at Low Temperature

be improved, or inaccurate measurements were taken during testing. A combination of both factors is most likely, with modeling problems contributing more than inaccurate measurement.

There are several improvements that may be considered in the model. First, conductive heat losses from the Kanthal wire to the metal connectors, used to hold them to the test power source, may be included. For these cases the conductive losses were deglected neglected since they were typically 5% of the other losses. While they were probably small, they could improve the model slightly.

Another possible source of error in the model may be the actual relationship used. While the downward trend of the curve in calculated heat loss as airflow decreases was encouraging, as this was to be expected, the entire curve may have been off because of the extremely low Reynold's number flow (as low as 0.01 for air velocities of 1 $^{cm}/_{sec}$) that may occur across some areas of

the sample. This relationship, $^{hd}/_{kf} = C \cdot Re^{n} \cdot Pr^{1/3}$, used values for coefficients C and n that are tested to flows only as low as Re=0.4.

Another problem with the model may have been its application to such a complex shape as the sample. Reynold's numbers used in calculations were found by estimating the shape of the sample with Kanthal wire coiled around it as a cylinder. While this was a fair estimate, it was not exact.

Inaccurate measurements may have been caused by several things. First, the leads from the multimeter were difficult to hold in an exact location during heating. Also, the multimeter may have been slightly out of calibration.

4.2.3 Comparison of Calculations vs. Observations in Teflon at High Temperature

The analytical predictions of heat loss in Teflon at high temperature were in much greater disagreement with observed power than were those in the low power tests (see Figure 10). The calculated value for heat loss was 72% lower than the measured value at 50 $^{cm}/_{sec}$ and the difference increased, until it was 79% lower at 15 $^{cm}/_{sec}$. This large disagreement negates the usefullness of the model to predict a power requirement at 1 $^{cm}/_{sec}$. Reasons for this larger disagreement were probably the same as for the low temperature test, but conduction may have played a greater role in this case. The higher temperature in the Kanthal heating wire would have led to more conductive losses to the connector.

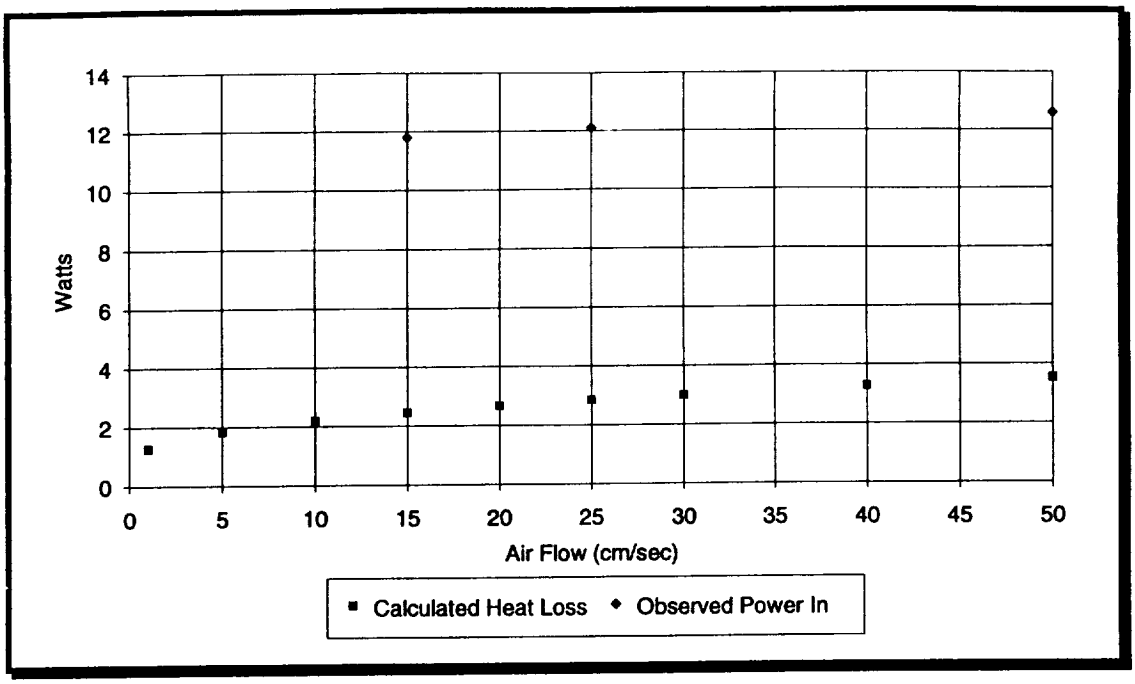

Figure 10. Calculated vs. Observed Heat Loss in Teflon at High Temperature

4.2.4 Comparison of Calculations vs. Observations in Silicone at Low Temperature

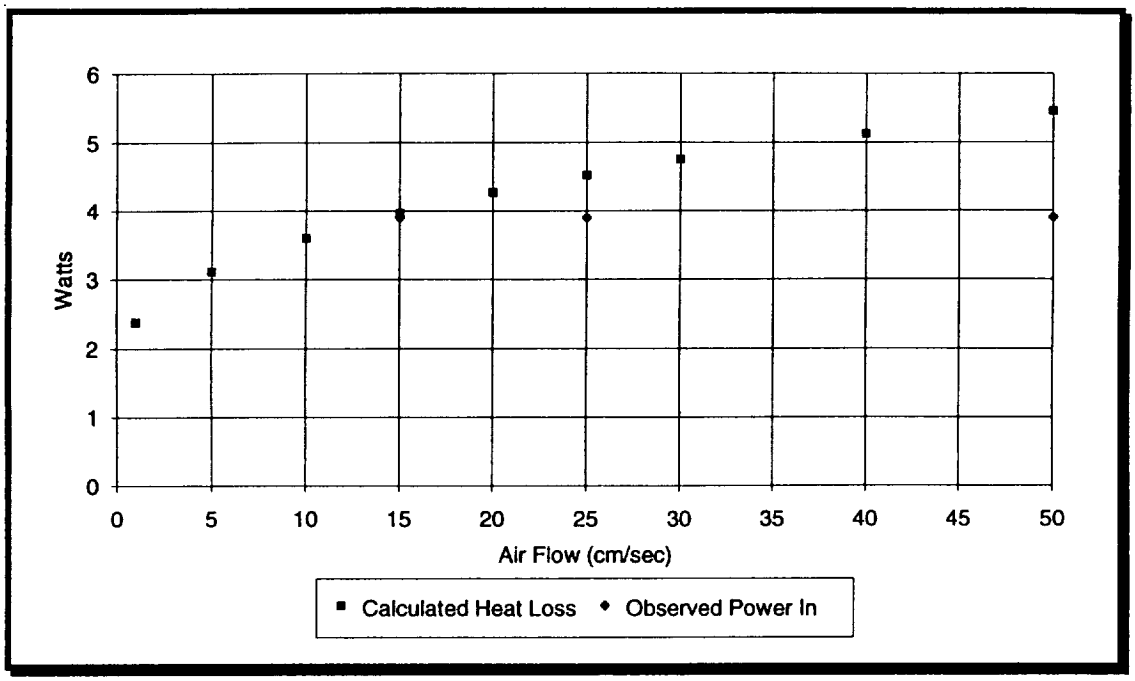

Figure 11. Calculated vs. Observed Heat Loss in Silicone at Low Temperature

The agreement between calculated and observed values in silicone at low temperature was interesting. There was some difference between the two at 50 $^{cm}/_{sec}$, but this difference was negligible (about 1%) at 15 $^{cm}/_{sec}$. Here, a value of 3.97 W was calculated for heat loss, while a value of 3.9 W was observed for power input (see Figure 11). The zero slope of the plot for observed power was probably due to an inability to measure very small differences in voltage and current with the multimeter. This plot would probably have good agreement with minor improvements in modeling and measurement technique as described above. The predicted value for power required at 1 $^{cm}/_{sec}$, while probably slightly low, was 2.38 W.

4.2.5 Comparison of Calculations vs. Observations in Silicone at High Temperature

The disagreement between calculated heat loss and observed power in was also high in silicone at high temperature samples. This difference became greater as air flow decreased. The calculated heat loss was 64% lower than measured at 50 $^{cm}/_{sec}$, and nearly 74% lower at 15 $^{cm}/_{sec}$. While this difference was not as great as in Teflon at high temperature, it is still too great for the analytical model to be accurate in predicting power required at 1 $^{cm}/_{sec}$. However, the difference between measured and calculated values is roughly constant, so this constant could be applied to the calculated value at 1 $^{cm}/_{sec}$ to get an estimate of required power. This same method could be used in Teflon at high temperature.

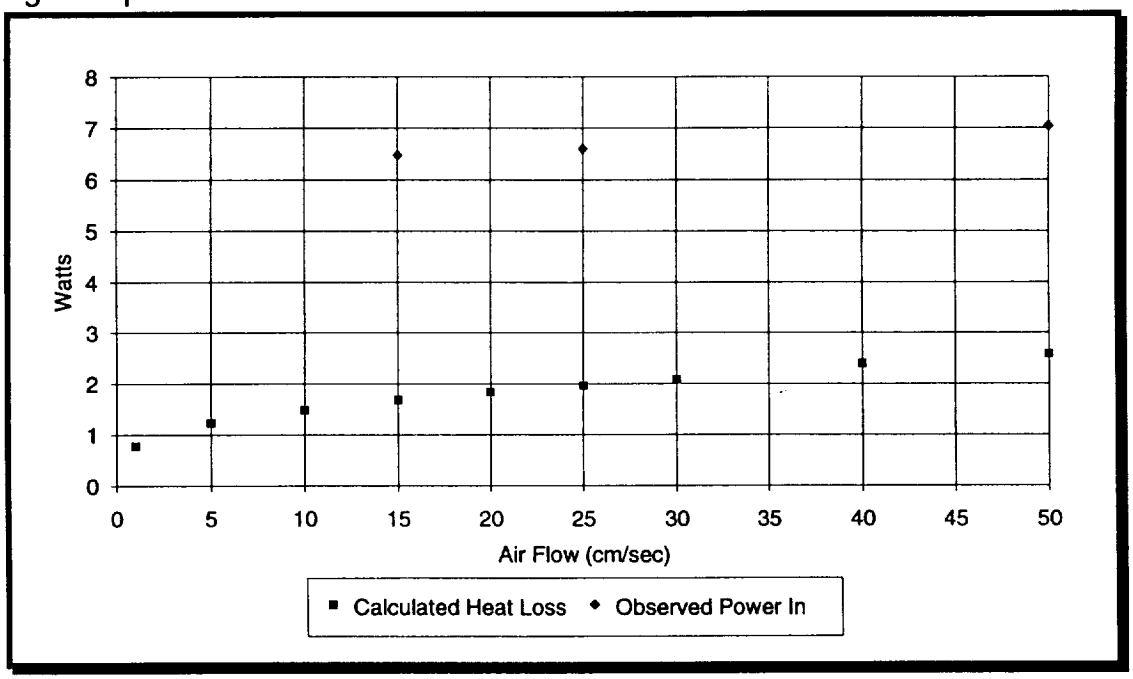

Figure 12. Calculated vs. Observed Heat Loss in Silicone at High Temperature

Chapter 5 Fuel Frame Design

After all experiments were performed, fuel frames were designed. These fuel frames fit into the existing near field sub-assembly and accommodate existing power leads. There will be little force on the package as it is launched because it will be a flat piece packed in foam, so the holder does not need to be very strong. Simple safety wire and commercial wire connectors provide sufficient support.

5.1 Frame for Low Temperature Test of Teflon

The fuel frame for low temperature tests of Teflon was by far the simplest to design. The small wire sample needed no support other than the Kanthal heating wire. The Kanthal was fixed to a male copper electrical connector at each end. These connectors were exactly 7cm apart. These connectors, in turn, were mated to a female connector attached to the Teflon frame. The connectors were attached at 1.25cm from each side of the midpoint of the upstream side of the frame using a common epoxy. See Figure 13.

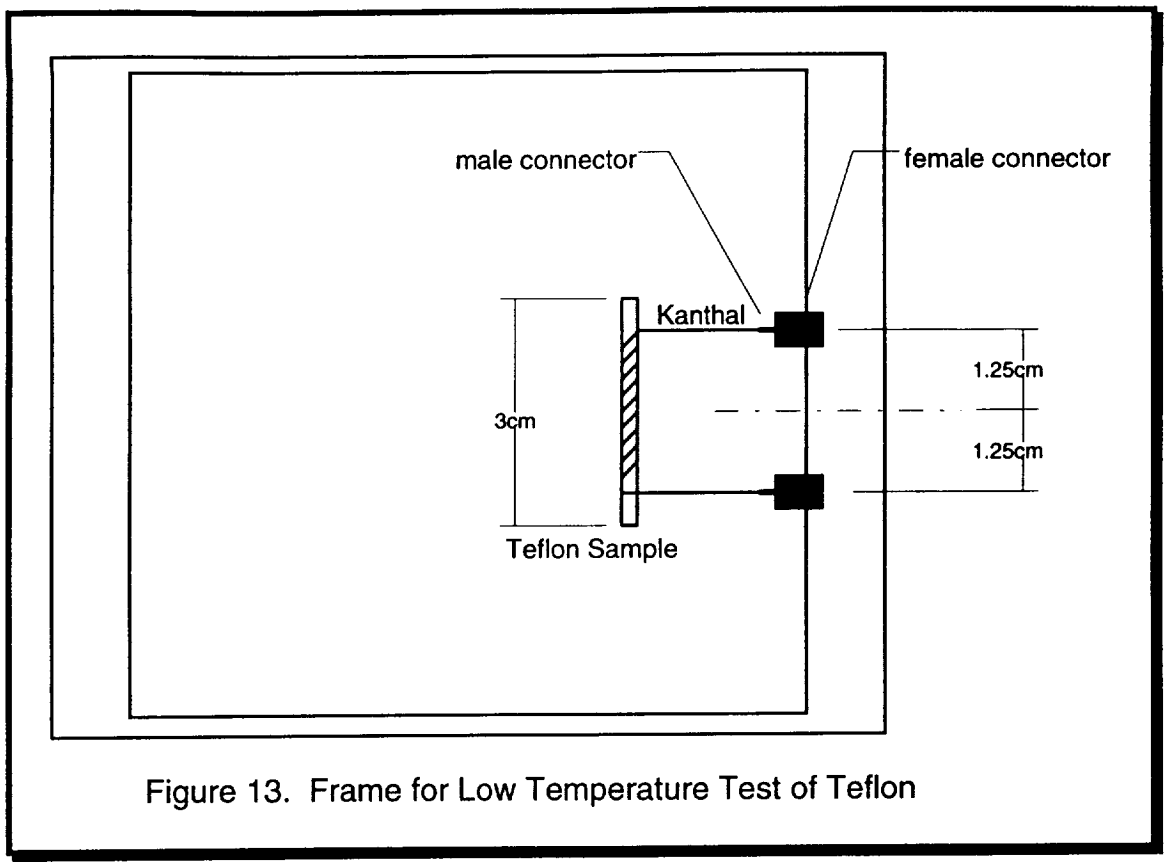

Figure 13. Frame for Low Temperature Test of Teflon

5.2 Frame for High Temperature Test of Teflon

The fuel frame for high temperature tests of Teflon required much more support than the low temperature frame. This extra support was necessary in order to prevent the sample from sliding or breaking free of the Kanthal heating wire. This extra support was simply provided by using a sample long enough to reach the ends of the frame. As shown in Figure 14, the sample was then placed down the long axis of the frame through two holes drilled in the sides of the frame and tied there. The Kanthal heating wire was connected to two copper male connectors as above, with the proper length of wire exposed. A 20 gauge wire is used to connect the Kanthal wire to female connectors attached to the sides.

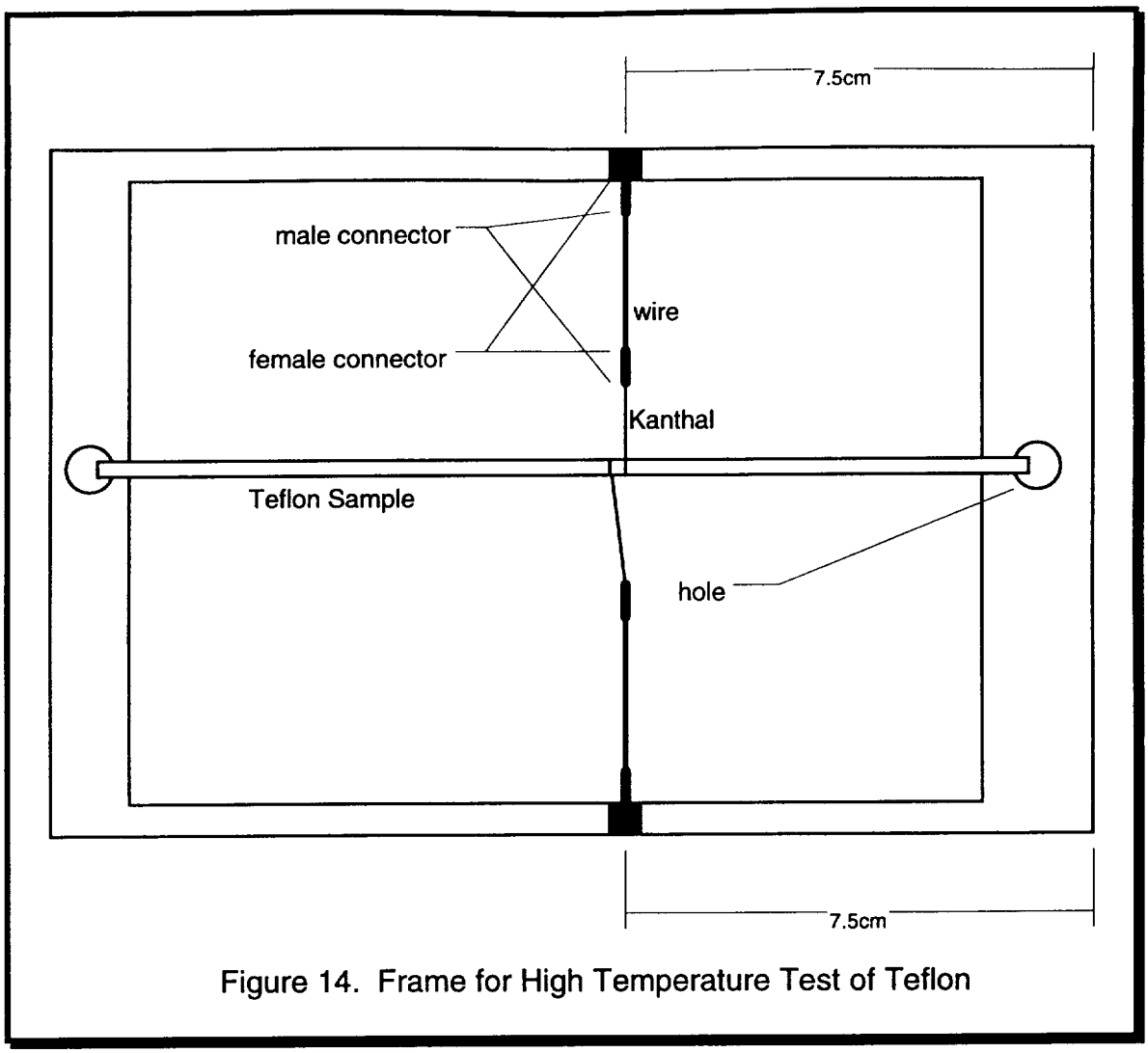

Figure 14. Frame for High Temperature Test of Teflon

5.3 Frame for Low Temperature Test of Silicone

The fuel frame for low temperature tests of silicone is similar to that for Teflon at low temperature in that it does not need any support other than the Kanthal heating wire. The only real difference between the two is the placement of the female connectors. These connectors must be placed only 0.6 cm from the midpoint of the fuel frame. This is to ensure that the Kanthal heating wire touches the sample in an even manner. See Figure 15. Conceivably, both silicone and Teflon could use the same holder for high temperatures. Care

should be taken, however, that the Kanthal wires leading from the female connectors are not bent at too much of an angle so that the contact geometry of the sample is affected.

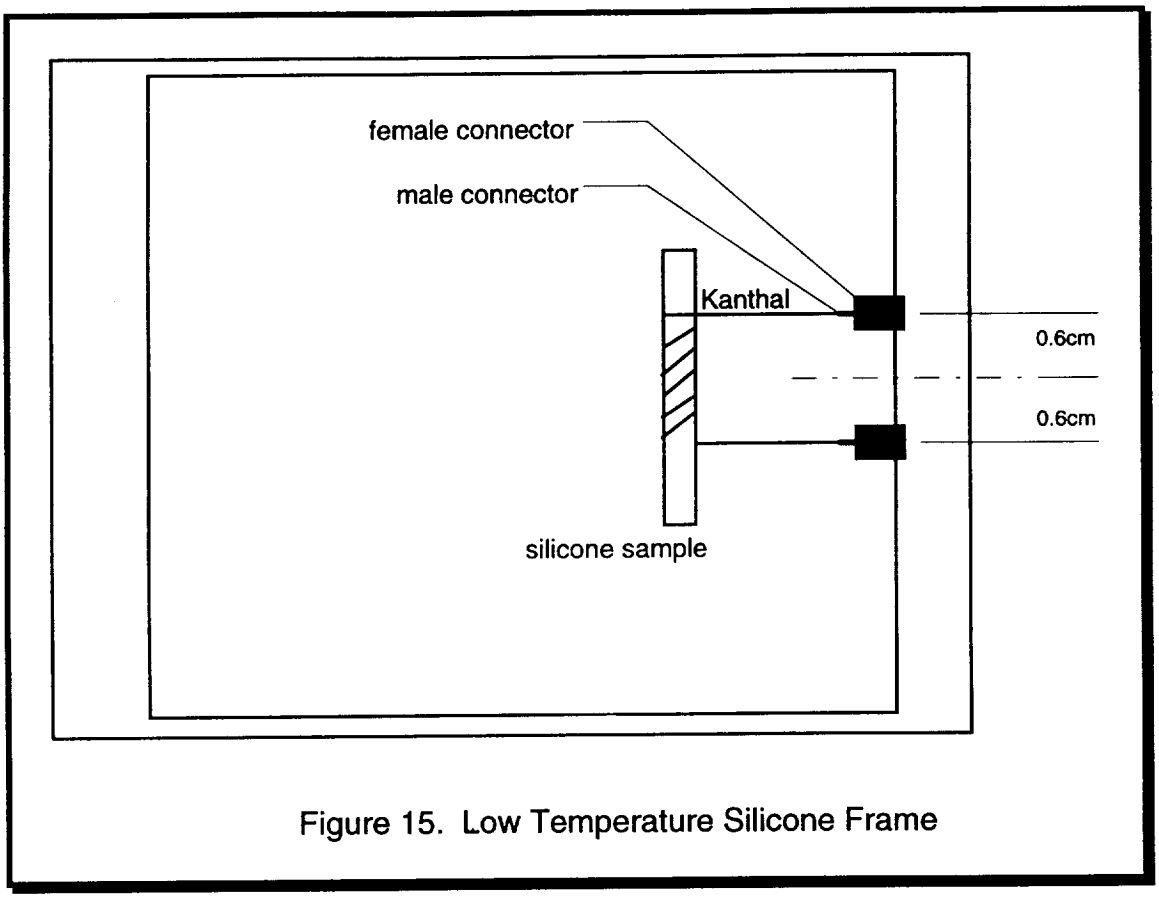

Figure 15. Low Temperature Silicone Frame

5.4 Frame for High Temperature Test of Silicone

The high temperature silicone frame is similar to the high temperature Teflon frame in that the sample required some support to prevent it from sliding or breaking free of the Kanthal heating element. See Figure 16. This support is obtained by piercing the sample at either end with two steel safety wires. The wires are bent into hooks where they pass through the sample so that they will not slip out. These safety wires should be long enough so that they may be tied

through holes drilled through the fuel frame.

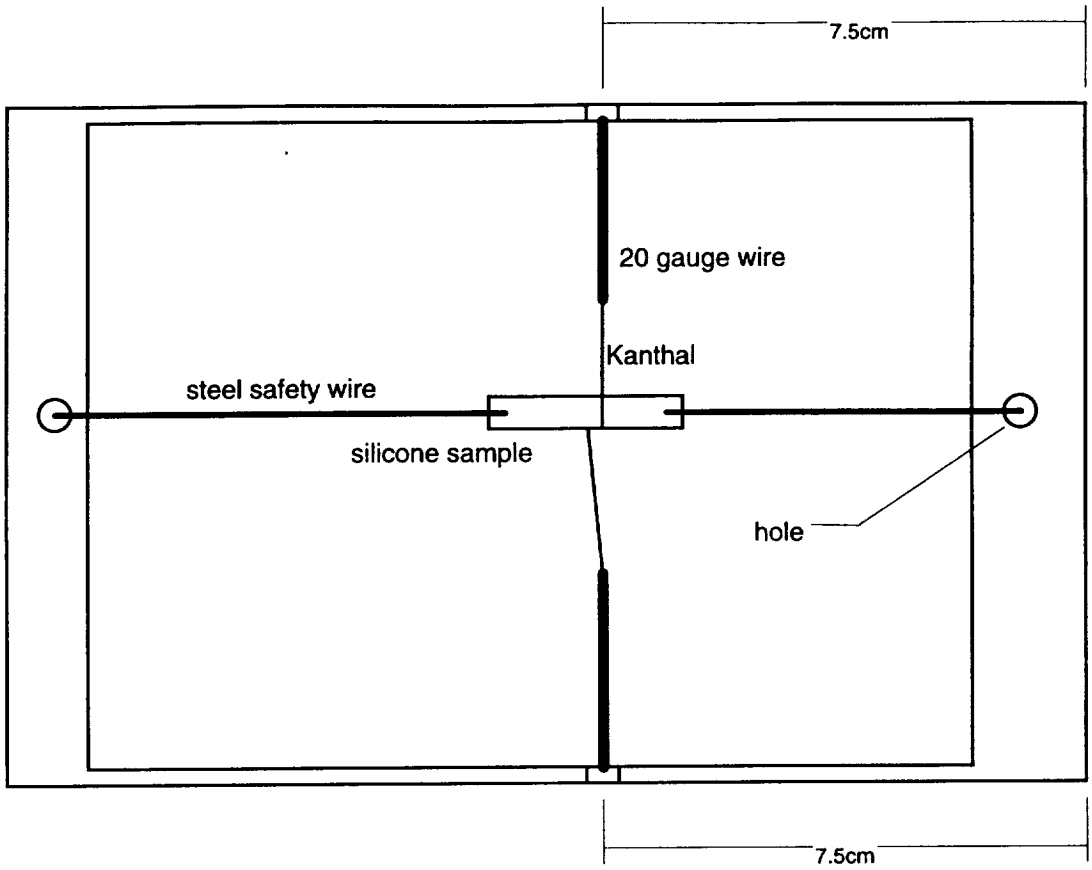

Figure 16. Frame for High Temperature Test of Silicone

Chapter 6 Conclusions and Future Projects

After the fuel frames are constructed and all hardware for the near and far field portions of the Comparative Soot Diagnostics Experiment are completed, NASA will test this apparatus using the actual smoke detectors. Any flaws must be corrected after testing.

It was found that all four sample types required different power levels, contact geometries, and fuel frames. The low temperature samples were designed to minimize temperature while maximizing contact area at a constant mass loss rate. These samples required low power and needed multiple coil contact geometries. Neither of the low temperature samples required support beyond the Kanthal heating element. Both high temperature samples were designed to maximize temperature while minimizing contact area at a constant mass loss rate. They required higher power levels than the low temperature samples. Their single coil contact geometries also necessitated the use of additional support in their fuel frames.

Future work in this area could include many projects. A versatile fuel frame may be developed to hold many different sample types. Better relationships for analytical prediction of voltage should also be found. Methods of sample preparation could be developed to ensure consistent samples. Also, many different materials and smoke detectors could be tested.

References

Custer, R. L. and Bright, R. G.; 1974; "Fire Detection: State of the Art," Cleveland: Aerospace Safety and Research and Data Institute

Friedman, R. and Sacksteder, K.; 1988; "Fire Behavior and Risk Analysis in Spacecraft," NASA TM-100944

Gorur, R. S. et. al.; 1988; "The AC. and DC. Performance of Polymeric Insulating Materials Under Accelerated Aging in a Fog Chamber," *IEEE Trans. Power Delivery.*

Holman, J. P.; 1990; *Heat Transfer,* McGraw Hill; USA

Holman, J. P.; 1989; *Experimental Methods For Engineers,* McGraw Hill; USA

Kanthal; 1990; *Kanthal Handbook of Resistance Heating Alloys For Appliances and Heaters*; Ljungforetagen, Orebro; Sweden

MathSoft, Inc.; 1986 - 1992; *Mathcad Version 3.1,* MathSoft, Inc.

NASA; 1992; "Microgravity Science and Applications Program 1992 Annual Report,"

NASA; 1992; "The First United States Microgravity Laboratory," U.S. Government Printing Office

OMEGA Engineering; 1992; *Omega Temperature Measurement Handbook and Encyclopedia*; Omega Engineering Inc.; USA

Touloukian, E.; 1970; *Thermophysical Properties of Matter, Volumes 2 and 4,* Plenum Press, USA

Urban, D; personal conversations with L. J. Dallaire, 1 June - 25 July, 1993

A. Appendix A
Experimental Data

A.a Low Temperature Test of Teflon @50$^{cm}/_{sec}$

m_1(g)	m_2(g)	Δm(g)	rate ($^{\mu g}/_{sec}$)	% difference	mean rate ($^{\mu g}/_{sec}$)
0.2574	0.2565	0.0009	15.0	-30.23%	21.5
0.261	0.2599	0.0011	18.3	-14.73%	
0.2552	0.2541	0.0011	18.3	-14.73%	std dev ($^{\mu g}/_{sec}$)
0.2683	0.2673	0.001	16.7	-22.48%	5.18
0.2599	0.2585	0.0014	23.3	8.53%	
0.2563	0.2553	0.001	16.7	-22.48%	
0.2577	0.2563	0.0014	23.3	8.53%	
0.2442	0.2425	0.0017	28.3	31.78%	
0.2023	0.2009	0.0014	23.3	8.53%	
0.1976	0.1957	0.0019	31.7	47.29%	

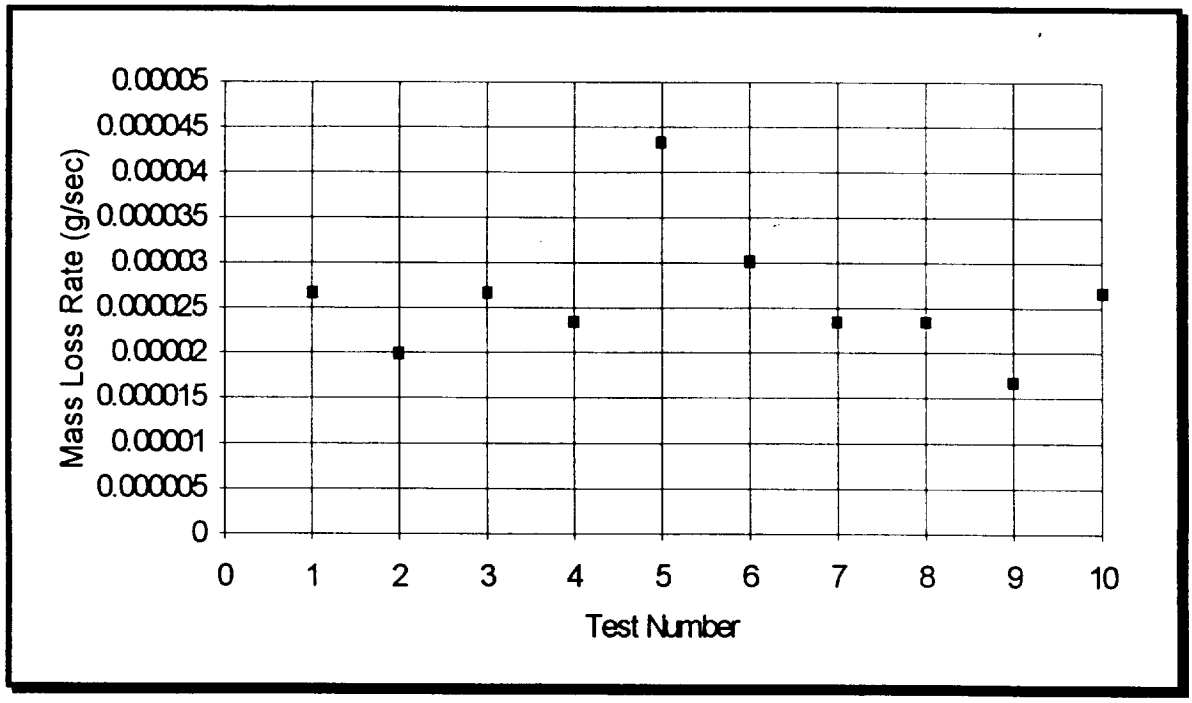

A.b High Temperature Test of Teflon @50$^{cm}/_{sec}$

m_1(g)	m_2(g)	Δm(g)	rate($^{\mu g}/_{sec}$)	% difference	mean rate ($^{\mu g}/_{sec}$)
0.2125	0.2119	0.0006	20.0	-14.29%	23.3
0.205	0.2044	0.0006	20.0	-14.29%	
0.2177	0.2169	0.0008	26.7	14.29%	std dev ($^{\mu g}/_{sec}$)
0.2277	0.2271	0.0006	20.0	-14.29%	2.58
0.216	0.2153	0.0007	23.3	0.00%	
0.2059	0.2052	0.0007	23.3	0.00%	
0.2242	0.2234	0.0008	26.7	14.29%	
0.2053	0.2046	0.0007	23.3	0.00%	
0.2063	0.2055	0.0008	26.7	14.29%	
0.1944	0.1937	0.0007	23.3	0.00%	

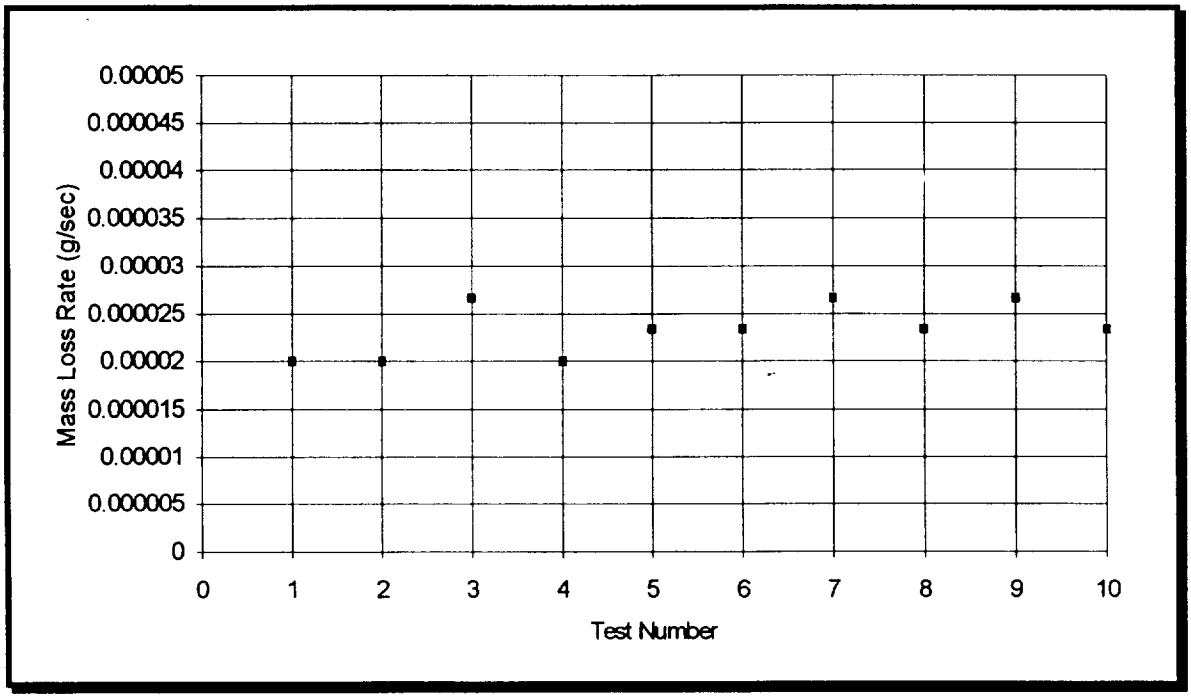

A.c Low Temperature Test of Silicone @50$^{cm}/_{sec}$

m_1	m_2	Δm	rate($^{\mu g}/_{sec}$)	% diff.	mean rate ($^{\mu g}/_{sec}$)
0.2014	0.2004	0.001	16.67	-26.47%	22.7
0.1924	0.191	0.0014	23.33	2.94%	
0.1998	0.1982	0.0016	26.67	17.65%	std dev ($^{\mu g}/_{sec}$)
0.1817	0.1806	0.0011	18.33	-19.12%	5.83
0.1819	0.1808	0.0011	18.33	-19.12%	
0.1812	0.1804	0.0008	13.33	-41.18%	
0.1722	0.1703	0.0019	31.67	39.71%	
0.1895	0.1881	0.0014	23.33	2.94%	
0.1945	0.1926	0.0019	31.67	39.71%	
0.1746	0.1732	0.0014	23.33	2.94%	

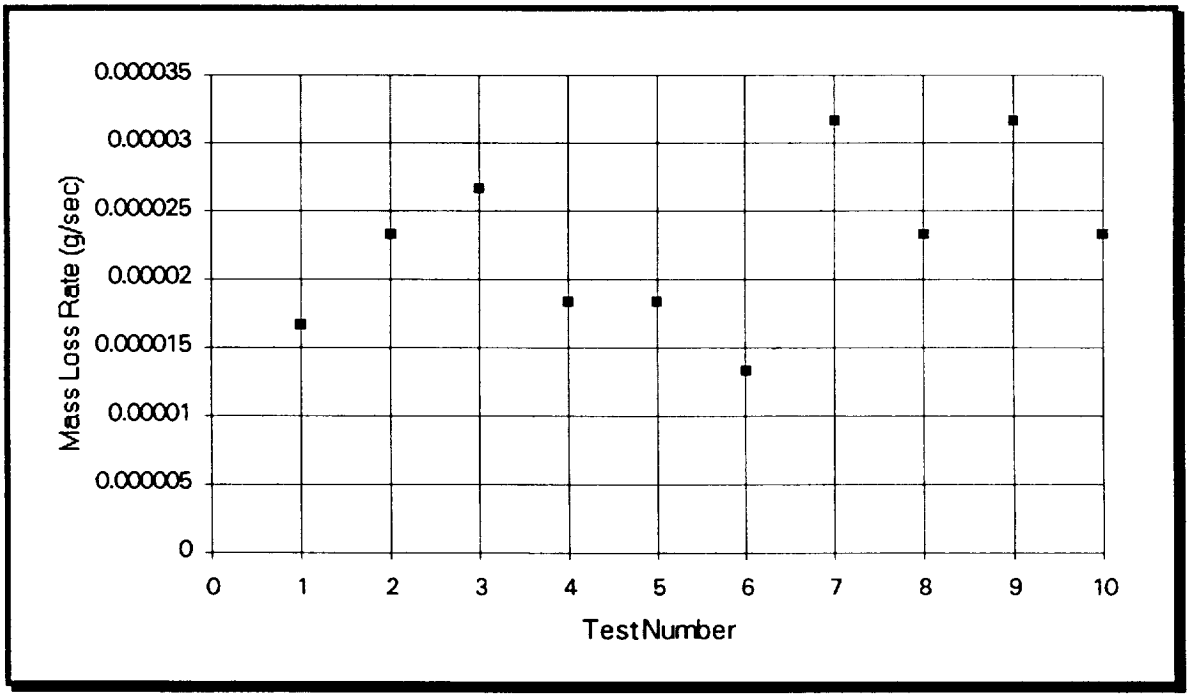

A.d High Temperature Test of Silicone @50$^{cm}/_{sec}$

m_1(g)	m_2(g)	Δm(g)	rate($^{\mu g}/_{sec}$)	% difference	mean rate ($^{\mu g}/_{sec}$)
0.2096	0.2075	0.0021	35	30.09%	27.0
0.267	0.2654	0.0016	26.7	-0.88%	
0.2684	0.2665	0.0019	31.7	17.70%	std dev ($^{\mu g}/_{sec}$)
0.2583	0.2569	0.0014	23.3	-13.27%	8.19
0.2507	0.2494	0.0013	21.7	-19.47%	
0.2664	0.2657	0.0007	11.7	-56.64%	
0.2759	0.2736	0.0023	38.3	42.48%	
0.2642	0.2629	0.0013	21.7	-19.47%	
0.2704	0.2684	0.002	33.3	23.89%	
0.2624	0.2612	0.0012	20.0	-25.66%	

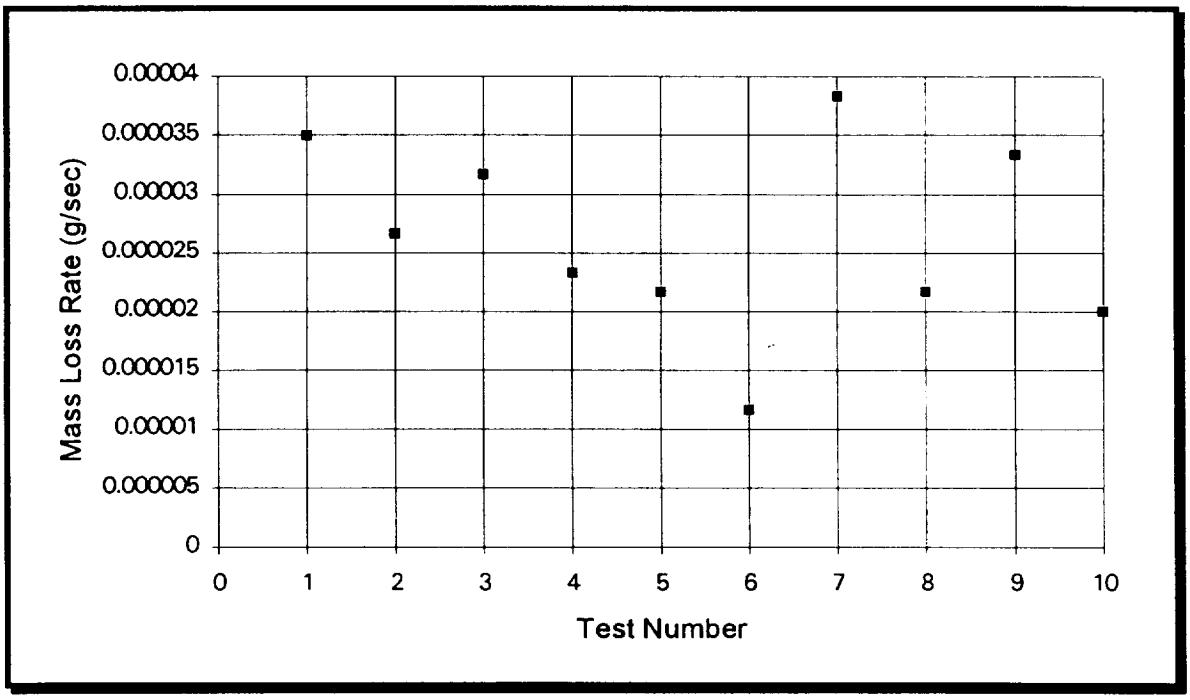

B. Appendix B
Complete Soolutions To Heat Transfer Calculations Using Mathcad

B.a Low Temperature Test ot Teflon Calculations

The losses from the legs of Kanthal wire leading to the sample may be found by:

$\mu := 2.7 \cdot 10^{-5}$ kg/m*s $\rho := 0.7$ $v := 0.5$ m/s $d := 0.005$ m

$\Delta T := 450$ K $\varepsilon := .9$ $\sigma := 5.669 \cdot 10^{-8}$ $Tw := 743$ K $To := 293$ K

$k := 0.041$ W/m*k $Pr := 0.68$

$$Re := \frac{\rho \cdot v \cdot d}{\mu}$$

$Re = 64.815$

$$r := \frac{\left(\frac{0.01}{2.54}\right)}{100}$$

$r = 3.937 \cdot 10^{-5}$ m

$C := 0.683$ $n := 0.466$

$$h := \frac{C \cdot k \cdot Re^{n} \cdot Pr^{\frac{1}{3}}}{d}$$

$h = 34.407$ W

$A := \pi \cdot 2 \cdot r \cdot (2 \cdot d)$

$A = 2.474 \cdot 10^{-6}$ m2

$ql := h \cdot A \cdot \Delta T + \varepsilon \cdot A \cdot \sigma \cdot (Tw^4 - To^4)$

$ql = 0.076$ W

The heat loss from the Kanthal wire not in contact with the sample may be found as follows:

$l := 0.06$

$$d := \frac{\left(\frac{0.01}{2.54}\right)}{100}$$

$d = 3.937 \cdot 10^{-5}$ m

$$Re := \frac{\rho \cdot v \cdot d}{\mu}$$

$Re = 0.51$

$C := 0.989$ $n := 0.330$

$$h := \frac{C \cdot k \cdot Re^{n} \cdot Pr^{\frac{1}{3}}}{d}$$

$h = 725.405 \quad W/m2*K$

$A := \pi \cdot d \cdot l$

$A = 7.421 \cdot 10^{-4} \quad m2$

$$qw := \frac{h \cdot A \cdot \Delta T}{2} + \varepsilon \cdot \frac{A}{2} \cdot \sigma \cdot (Tw^4 - To^4)$$

$qw = 1.268 \quad W$

The heat lost from the sample itself is:

$d := 1.5 \cdot 10^{-3} m \quad l := 0.03 \ m$

$$Re := \frac{\rho \cdot v \cdot d}{\mu}$$

$Re = 19.444$

$C := 0.911 \quad n := 0.385$

$$h := \frac{C \cdot k \cdot Re^{n} \cdot Pr^{\frac{1}{3}}}{d}$$

$h = 68.638 \quad W/m2*K$

$A := \pi \cdot d \cdot l$

$A = 1.414 \cdot 10^{-4} \quad m2$

$qs := h \cdot A \cdot \Delta T + \varepsilon \cdot A \cdot \sigma \cdot (Tw^4 - To^4)$

$qs = 6.512 \quad W$

The total heat lost by the sample and Kanthal wire, which must equal the power through the wire is:

$Qtotal := ql + qw + qs$

$P := Qtotal$

$P = 7.855 \quad W$

B.b High Temperature Test of Teflon Calculations

The losses from the legs of Kanthal wire leading to the sample may be found by:

$\mu := 2.95 \cdot 10^{-5}\ kg/m*s$ $\rho := 0.61$ $v := 0.5\ m/s$ $l := 0.045\ m$

$\Delta T := 580\ K$ $\varepsilon := .9$ $\sigma := 5.669 \cdot 10^{-8}$ $Tw := 873\ K$ $To := 293\ K$

$k := 0.045\ W/m*K$ $Pr := 0.680$

$$d := \frac{\left(\frac{0.01}{2.54}\right)}{100}$$

$d = 3.937 \cdot 10^{-5}\ m$

$$Re := \frac{\rho \cdot v \cdot d}{\mu}$$

$Re = 0.407$

$C := 0.989$ $n := 0.330$

$$h := \frac{C \cdot k \cdot Re^{n} \cdot Pr^{\frac{1}{3}}}{d}$$

$h = 738.915\ W/m2*K$

$A := \pi \cdot d \cdot l$

$A = 5.566 \cdot 10^{-6}\ m2$

$ql := h \cdot A \cdot \Delta T + \varepsilon \cdot A \cdot \sigma \cdot (Tw^4 - To^4)$

$ql = 2.548\ W$

The heat loss from the Kanthal wire not in contact with the sample may be found as follows:

$l := 0.005\,m$

$$Re := \frac{\rho \cdot v \cdot d}{\mu}$$

$Re = 0.407$

$C := 0.989 \quad n := 0.330$

$$h := \frac{C \cdot k \cdot Re^{n} \cdot Pr^{\frac{1}{3}}}{d}$$

$h = 738.915 \quad W/m2*K$

$A := \pi \cdot d \cdot l$

$A = 6.184 \cdot 10^{-7} \quad m2$

$$qw := h \cdot \frac{A}{2} \cdot \Delta T + \varepsilon \cdot \frac{A}{2} \cdot \sigma \cdot (Tw^{4} - To^{4})$$

$qw = 0.142 \quad W$

The heat lost from the sample itself is must be found using the relationship for an infinite fin, as the length of the sample not covered by the Kanthal approximates this. Radiation will be approximated by the average temperature of the fin and computed over the length of the fin:

$d := 1.5 \cdot 10^{-3}\ m$ $Per := 4.7 \cdot 10^{-3}\ m$ $Axc := 1.77 \cdot 10^{-6}\ m^2$

$Tend := 294\ K$ $Tave := 583\ K$ $ksample := 4.5$ $m := \sqrt{\frac{h \cdot Per}{ksample \cdot Axc}}$

$Re := \frac{\rho \cdot v \cdot d}{\mu}$

$Re = 15.508$

$C := 0.911$ $n := 0.385$

$h := \frac{C \cdot k \cdot Re^{n} \cdot Pr^{\frac{1}{3}}}{d}$

$h = 69.052\ W/m2*K$

$A := \pi \cdot \left(\frac{d}{2}\right)^2$ $\theta o := Tw - To$

$A = 1.767 \cdot 10^{-6}\ m^2$

$qs := \sqrt{h \cdot Per \cdot k \cdot A} \cdot \theta o + \varepsilon \cdot Afin \cdot \sigma \cdot (Tave^4 - To^4)$

$qs = 0.343\ W$

$\frac{Tend - To}{Tw - To} - \exp((-m \cdot x))$

$x := \frac{-\ln\left[\frac{-(Tend - To)}{(-Tw + To)}\right]}{m}$

$x = 0.01\ m$

$Afin := x \cdot Per$

The total heat lost by the sample and Kanthal wire, which must equal the power through the wire is:

$Qtotal := ql + qw + qs$

$P := Qtotal$

$P = 3.033\ W$

B.c Low Temperature Test of Silicone Calculations

The losses from the legs of Kanthal wire leading to the sample may be found by:

$\mu := 2.48 \cdot 10^{-5}\,m$ $\rho := 0.78$ $V := 0.5\,m/s$ $d := 0.005\,m$ $l := 0.02\ m$

$\Delta T := 330\,K$ $\varepsilon := .9$ $\sigma := 5.669 \cdot 10^{-8}$ $Tw := 623\,K$ $To := 293\,K$

$k := 0.038\ W/m*K$ $Pr := 0.683$

$$Re := \frac{\rho \cdot V \cdot d}{\mu}$$

$Re = 78.629$

$$r := \frac{\left(\frac{0.01}{2.54}\right)}{100}$$

$r = 3.937 \cdot 10^{-5}$ m

$C := 0.683$ $n := 0.466$

$$h := \frac{C \cdot k \cdot Re^{n} \cdot Pr^{\frac{1}{3}}}{d}$$

$h = 34.945$ W/m2*k

$A := \pi \cdot 2 \cdot r \cdot 2 \cdot d$

$A = 2.474 \cdot 10^{-6}$ m2

$ql := h \cdot A \cdot \Delta T + \varepsilon \cdot A \cdot \sigma \cdot (Tw^{4} - To^{4})$

$ql = 0.047$ W

The heat loss from the Kanthal wire not in contact with the sample may be found as follows:

$$l := 0.065\,m \qquad d := \frac{\left(\frac{0.01}{2.54}\right)}{100}$$

$$d = 3.937 \cdot 10^{-5}\,m$$

$$Re := \frac{\rho \cdot v \cdot d}{\mu}$$

$$Re = 0.619$$

$$C := 0.989 \qquad n := 0.330$$

$$h := \frac{C \cdot k \cdot Re^{n} \cdot Pr^{\frac{1}{3}}}{d}$$

$$h = 717.642 \quad W/m2*K$$

$$A := \pi \cdot d \cdot l$$

$$A = 8.04 \cdot 10^{-6} \quad m2$$

$$qw := h \cdot \frac{A}{2} \cdot \Delta T + \varepsilon \cdot \frac{A}{2} \cdot \sigma \cdot (Tw^{4} - To^{4})$$

$$qw = 0.981 \quad W$$

The heat lost from the sample itself is:

$d := 2.2 \cdot 10^{-3}\,m \quad l := 0.02m$

$$Re := \frac{\rho \cdot v \cdot d}{\mu}$$

$Re = 34.597$

$C := 0.911 \quad n := 0.385$

$$h := \frac{C \cdot k \cdot Re^{n} \cdot Pr^{\frac{1}{3}}}{d}$$

$h = 54.227 \quad W/m2*K$

$A := 4 \cdot d \cdot l$

$A = 1.76 \cdot 10^{-4} \quad m2$

$qs := h \cdot A \cdot \Delta T + \varepsilon \cdot A \cdot \sigma \cdot (Tw^4 - To^4)$

$qs = 4.436 \quad W$

The total heat lost by the sample and Kanthal wire, which must equal the power through the wire is:

$Qtotal := ql + qw + qs$

$P := Qtotal$

$P = 5.464 \quad W$

B.d High Temperature Test of Silicone Calculations

The losses from the legs of Kanthal wire leading to the sample may be found by:

$\mu := 2.7 \cdot 10^{-5}$ kg/m*s $\rho := 0.69$ kg/m3 $v := 0.5$ m/s $l := 0.045$ m

$\Delta T := 450$ K $\varepsilon := .9$ $\sigma := 5.669 \cdot 10^{-8}$ $Tw := 743$ K $To := 293$ K

$k := 0.041$ W/m*k $Pr := 0.680$

$$d := \frac{\left(\frac{0.01}{2.54}\right)}{100}$$

$d = 3.937 \cdot 10^{-5}$ m

$$Re := \frac{\rho \cdot v \cdot d}{\mu}$$

$Re = 0.503$

$C := 0.989$ $n := 0.330$

$$h := \frac{C \cdot k \cdot Re^{n} \cdot Pr^{\frac{1}{3}}}{d}$$

$h = 721.969$ W/m2*K

$A := \pi \cdot d \cdot l$

$A = 5.566 \cdot 10^{-6}$ m2

$ql := h \cdot A \cdot \Delta T + \varepsilon \cdot A \cdot \sigma \cdot (Tw^4 - To^4)$

$ql = 1.893$ W

The heat loss from the Kanthal wire not in contact with the sample may be found as follows:

$l := 0.005\,m$

$$Re := \frac{\rho \cdot v \cdot l}{\mu}$$

$Re = 63.889$

$C := 0.683 \quad n := 0.466$

$$h := \frac{C \cdot k \cdot Re^{n} \cdot Pr^{\frac{1}{3}}}{d}$$

$h = 4.34 \cdot 10^{3} \quad W/m2*K$

$A := \pi \cdot d \cdot l$

$A = 6.184 \cdot 10^{-7} \quad m2$

$$qw := h \cdot \frac{A}{2} \cdot \Delta T + \varepsilon \cdot \frac{A}{2} \cdot \sigma \cdot (Tw^{4} - To^{4})$$

$qw = 0.609 \quad W$

The heat lost from the sample itself is must be found using the relationship for an infinite fin, as the length of the sample not covered by the Kanthal approximates this Radiation will be approximated by using the average temperature of the fin over the length of the fin

d := 1.3·10^-3 m Axc := 4.84·10^-6 m2

P := 4.4·10^-3 m Tend := 294 K

ksample := 19·10^-4 W/m*K

$$m := \sqrt{\frac{h \cdot P}{ksample \cdot Axc}}$$

$$Re := \frac{\rho \cdot v \cdot d}{\mu}$$

Re = 19.167

$$\frac{Tend - To}{Tw - To} - \exp((-m \cdot x))$$

C := 0.911 n := 0.385

$$x := \frac{-\ln\left[\frac{-(Tend - To)}{(-Tw + To)}\right]}{m}$$

x = 1.341·10^-4

$$h := \frac{C \cdot k \cdot Re^{n} \cdot Pr^{\frac{1}{3}}}{d}$$

Afin := x·P

h = 68.259 W/m2*K

$$A := \pi \cdot \left(\frac{d}{2}\right)^{2}$$

θo := Tw - To

A = 1.767·10^-6 2

qs := $\sqrt{h \cdot P \cdot k \cdot A}$·θo + ε·Afin·σ·(Tw^4 - To^4)

qs = 0.075 W

The total heat lost by the sample and Kanthal wire, which must equal the power through the wire is.

Qtotal := ql + qw + qs

P = Qtotal

P = 2.577 W

B.e List of Symbols Used in Mathcad

A	area	ql	heat lost by Kantal legs
Afin	radiative area of fin	qs	heat lost by sample
Axc	cross sectional area of fin	qw	heat lost by Kanthal
C	constant found in Holman, 1990	Re	Reynold's number
d	diameter	Tave	average temperature of fin
h	convective coefficient	Tend	temperature at end of effective radiative portion of fin
k	thermal conductivity of air	To	ambient temperature
ksample	thermal conductivity of sample	Tw	temperature of Kanthal wire
l	length	v	velocity
n	exponent found in Holman, 1990	x	length of radiative portion of fin
P	power	ε	emissivity
Per	perimeter	μ	viscosity
Pr	Prandtl number	σ	Boltzmann's constant

C. Appendix C
Calculations

C.a Determination of Mass Flow Through Sample Chamber

$$\dot{v} = A\vec{v} \qquad \text{(C.a-1)}$$

where $\dot{v}$ is the volumetric flow rate,

A is the cross sectional area normal to the flow,

and $\vec{v}$ is the velocity of the flow

$A = 9216 cm^2$, $\quad \vec{v} = 1 {}^{cm}/_{sec}$

substituting int (C.a-1) we have:

$$\dot{v} = (9216 {}^{cm}/_{sec})(1 cm^2)$$
$$= 9216 {}^{cm^3}/_{sec}$$

$$m = \rho_{air}\dot{v} \qquad \text{(C.a-2)}$$

where m is the mass flow rate,

and ρ_{air} is the density of air

$\rho_{air} = 0.001178 {}^{g}/_{cm^3}$ at $20^o C$ (Holman, 1990)

substituting into (C.a-2), we have:

$$m = (0.01178 {}^{g}/_{cm^3})(9216 {}^{cm^3}/_{sec})$$
$$= 10.86 {}^{g}/_{sec}$$

C.b Determination of Correct Mass Loss Rate

$$2\,ppm = 0.000002\,m$$

$$= (0.000002)(10.86\,g/sec)$$

$$= .0000217\,g/sec$$

$$= 21.7\,\mu g/sec$$

C.c Determination of Actual Resistance per Length

$$R = \frac{V}{i} \qquad \text{(D.c-1)}$$

where R is the resistance of the wire,
V is the voltage across the wire,
and i is the current through the wire

$$\omega = \frac{R}{l} = \frac{\frac{V}{i}}{l} \qquad \text{(D.c-2)}$$

where ω is the resistance per unit length of Kanthal and l is its length. The measured values of V, i, and l are then substituted into (D.c-2).

$$\omega = \frac{\frac{4.5V}{1.4A}}{10cm}$$

$$= .32\,\Omega/cm$$

C.d Determination of Current Through Different Contact Geometries

$R = \omega l$

where R is the resistance of the wire,

ω is the resistance per unit length of the wire,

and l is the length of the wire

$$i = \frac{V}{R} = \frac{V}{\omega l}$$

where i is the current passing through the wire

For the low temperature silicone sample,

$V = 3V,\ l = 7.5cm,\ \omega = 0.32\,\Omega/_{cm}$

so, substituting into (D.d-2), we have

$$i = \frac{3V}{(0.32\,\Omega/_{cm})(7.5cm)} = 1.25A$$

For the low temperature Teflon sample,

$V = 4.35V,\ l = 7cm,\ \omega = 0.32\,\Omega/_{cm}$

substituting into (D.d-2), we have

$$i = \frac{4.35V}{(0.32\,\Omega/_{cm})(7cm)} = 1.94A$$

For the high temperature Teflon sample,

$V = 4.5V,\ l = 5cm,\ \omega = 0.32\,\Omega/_{cm}$

so, substituting into (D.d-2), we have

$$i = \frac{4.5V}{(0.32\,\Omega/_{cm})(5cm)} = 2.81A$$

For the high temperature silicone sample,

$V = 3.35V,\ l = 5cm,\ \omega = 0.32\,\Omega/_{cm}$

so, substituting into (D.d-2), we have

$$i = \frac{4V}{(0.32\,\Omega/_{cm})(5cm)} = 2.09A$$

SECTION 3

SOLID STATE LASER POWER MEASUREMENT SYSTEM

by

Christopher A. Toth

Prepared, in part, as a Major Qualifying Project in
Electrical Engineering Department
Worcester Polytechnic Institute
1993-94

Table of Contents

Acknowledgements

I would like to thank the following people for their aid in the completion of this Major Qualifying Project

Professor R. James Duckworth
Professor Vahid Motevalli

The NASA Lewis Research Center
The NASA LeRC Microgravity Group
Dr. Randy Vander Wal
Dr. Howard Pearlman
Bill Yanis
Dr. Paul Greenberg
Dr. Devon Griffin
Dr. Karen Weiland

T.J. Marsden
L.J. Dallaire
Mike Pereira

Joe Provo
Ed Preble
Jason Makofsky

List of Figures

Chapter 1

Introduction

This Major Qualifying Project involved the design of detection circuitry to measure relative power signals from a laser system for a better understanding of the fluctuations of the laser power and for normalization of experimental signals as a function of the laser power intensity. Lasers are used in combustion experiments at the National Aeronautics and Space Administration's (NASA) Lewis Research Center (LeRC), and in most of the experiments, the results are related to the laser power intensity. To measure the laser beam and not to effect the experiment, a relative measurement of

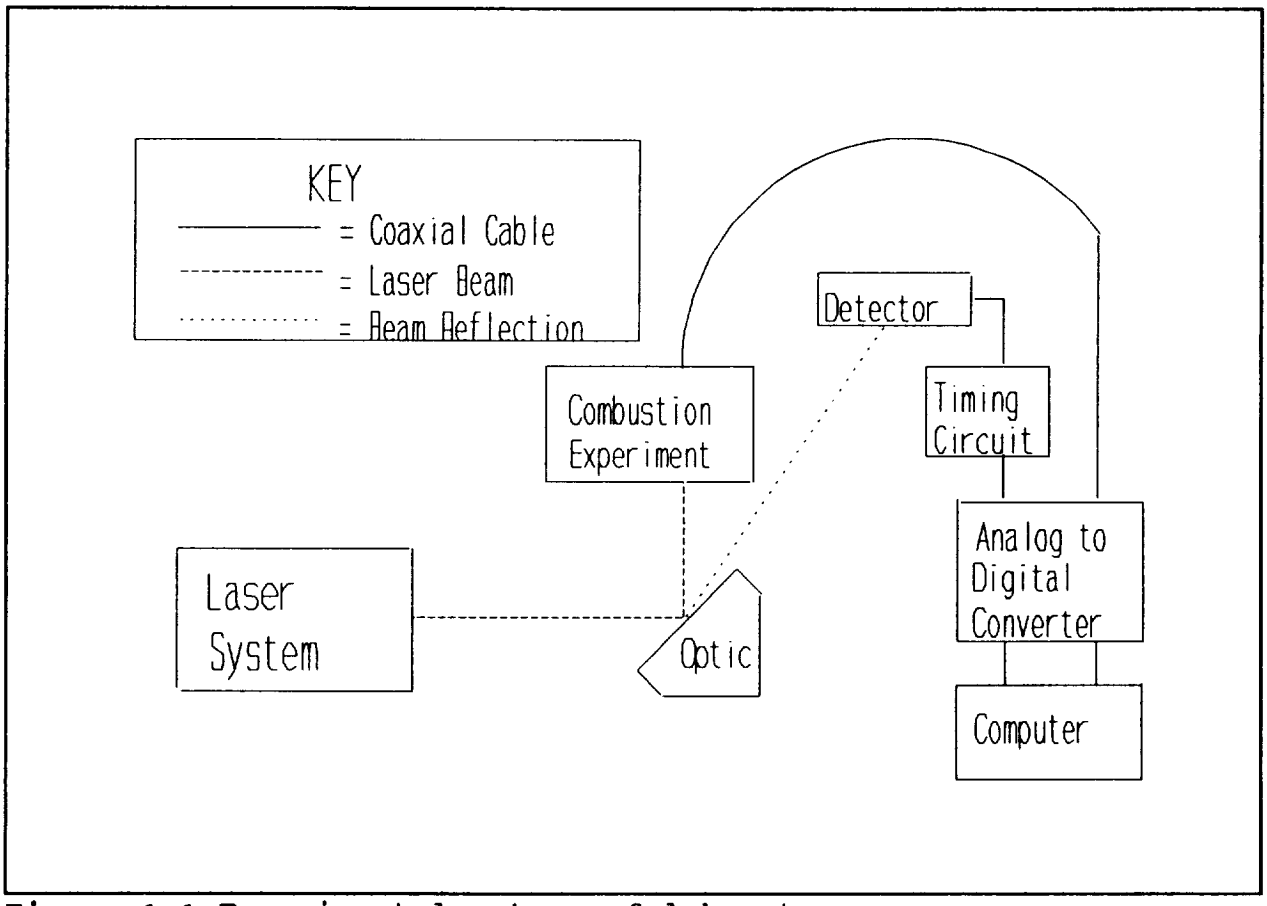

Figure 1.1 Experimental set up of laboratory

the beam can be taken from reflections of the laser along the beam path. The measurements are then digitized and sent to a computer for storage (Fig. 1.1). For example, during an experiment to measure flame temperature, the detector circuit would catch the beam reflection from the optic of the flame experiment and send a power measurement to the computer so the results can be studied as a function of the laser power intensity.

1.1 Microgravity Research

Research conducted by the Microgravity Science and Applications Division is designed to investigate gravity's effects everyday happenings, such as flame spread, crystal growth, and many other phenomena [NASA, 1992] in which gravity is often overlooked. For example, in microgravity, crystals grow much larger and more uniform than in full gravity. Because of NASA's proposed space stations and laboratories, microgravity projects, however simple they might seem, must be conducted to ensure safety in space and to get an understanding of how things will react to microgravity; everything from electrical characteristics in wire to how flames spread are some phenomena being studied to bring this knowledge to the stations.

Lasers are used in the combustion experiments to measure soot particles, species concentrations in flames, flame temperatures, ionization rates, etc.[Vander Wal, 1993] Laser diagnostic techniques are used in developing the microgravity experiments and for analysis. For those experiments, the magnitude of the laser

pulses needs to be known to help normalize those signals as a function of power. The goals of this MQP were to chose a detector to monitor the laser power and to design an appropriate set of circuitry showing the laser performance. Also, the detection design had to be portable and small enough to fit in the experimental package.

With microgravity experiments, the size of the experiment is of great importance. Because of the location of the experiments, all packages must be of a predetermined size, depending on where it was to be conducted. This causes any component of the experiment to be as small as possible.

1.2 Laser Research

The laser is an instrument; it is not perfect and it will not always give the same exact pulses. The laser has tolerances, like any other instrument. In almost every use of lasers, the beam gets filtered or directed by optics. When a beam strikes an optic, a portion of the beam is reflected away. Reflection of the beam is determined by the angle the beam strikes the optic. When measuring the reflected beam, the reflection's magnitude is directly proportional to the original beam power, giving a relative measure. The original pulse might have a drop in intensity, so, therefore, the reflection will as well. Measuring the reflected beam shows the laser variance, and with that information the error in many experiments can be minimized, yielding better results.

When using pulsed lasers, researchers need to measure the

reflection of the pulses accurately. Some lasers give high power pulses which would burn out ordinary luminance meters, if the meter could even register the pulses. The beams are not always visible; many are in the infrared and ultraviolet spectrums. Also, with high speed pulses, most meters can not to work fast enough to pick up a beam lasting for microseconds, sometimes many magnitudes less. Commercial models of pulse detectors are available, but at a high cost, with some of the least expensive models costing well into the thousands of dollars. A system was needed to send the power measurements to the existing data acquisition equipment so the experimental results could be studied later.

Two of the most common detectors for measurements of laser pulses are pyroelectric detectors and photodiodes. Aside from the principles of detection, they both function as diodes with similar internal operations. As either the photodiode or pyroelectric detector begins to operate, gaps develop in the detector's material, allowing electron flow through the device. In laser pulse measurements, both detectors are applicable, but proper usage must be employed.

After choosing a detector, the signal produced needs to be sent to the acquisition equipment in order to normalize the combustion experiments as a function of the laser intensity. With the power measurements and combustion experiments conducted simultaneously, the experiments can be studied as a function of the laser power. As the laser power varies, the result of the variance can be seen in the other experiments.

The following chapters discuss the hardware used for detecting the laser pulses (Chapter 2), the pros and cons of each detector (Chapter 2), the employment of the device to detect the laser (Chapter 3), how to modify the signal for digitization (Chapter 3), and the performance of the circuit in the laboratory (Chapter 4).

Chapter 2

Photodiodes and Pyroelectric Detectors

Photodiodes and pyroelectric detectors measure light above, below, and in the visible spectrum. Photodiodes measure the light intensity, with the response depending on the wavelength and the intensity of the light, while pyroelectric detectors respond to a temperature change due to the change of the light intensity, independent of the wavelength.

Both of these detectors types function the same as diodes; as light strikes the sensing element (the photodiode), or the incident radiation on the element changes (the pyroelectric detector), gaps start to appear in the material and cause electron flow through the layers. This flow of electrons through the material creates the

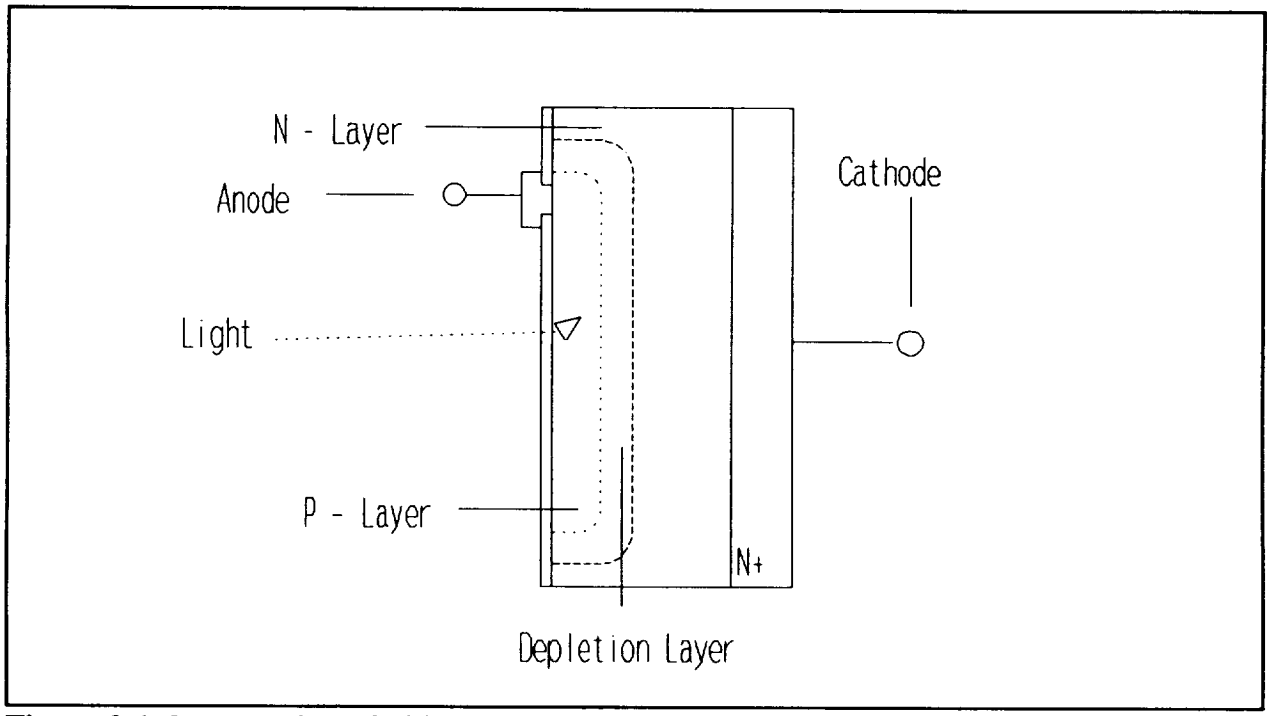

Figure 2.1 Cross section of Silicon Photodiode [Hamamatsu, 1991]

current in the device.(Fig. 2.1)

There are three basic variables to consider when choosing a pyroelectric detector or photodiode. Different detectors exist, widely ranging in purpose, all with the same basic options; (1) the window on the detector, (2) the sensing element itself, and, if needed, (3) additional electronics to be included in the detector package.

On the detector package, the sensing element rests in the casing, suspended below the sides of the package covered by a window (option 1). The window on the front of the detector protects the sensing element from damage, but windows can also be used to filter some wavelengths of light. The windows have to be kept clean, otherwise the incoming light gets altered and poor results are obtained.

For the sensing element (option 2) on the photodiodes, the proper device must be chosen because of its wavelength sensitivity or the element might not detect the light. The photodiodes are useful for systems with known wavelength, with small variances in wavelength, or where the wavelength is constant. Almost all photodiodes operate in the visible light spectrum and have a limited response outside of that range depending on the material used for the element.

Pyroelectric detectors are made with many arrangements of the sensing element.(Fig. 2.2) The elements come in single or double element packages, and if a double element package is used, it can be arranged differently. The main advantage of the single element

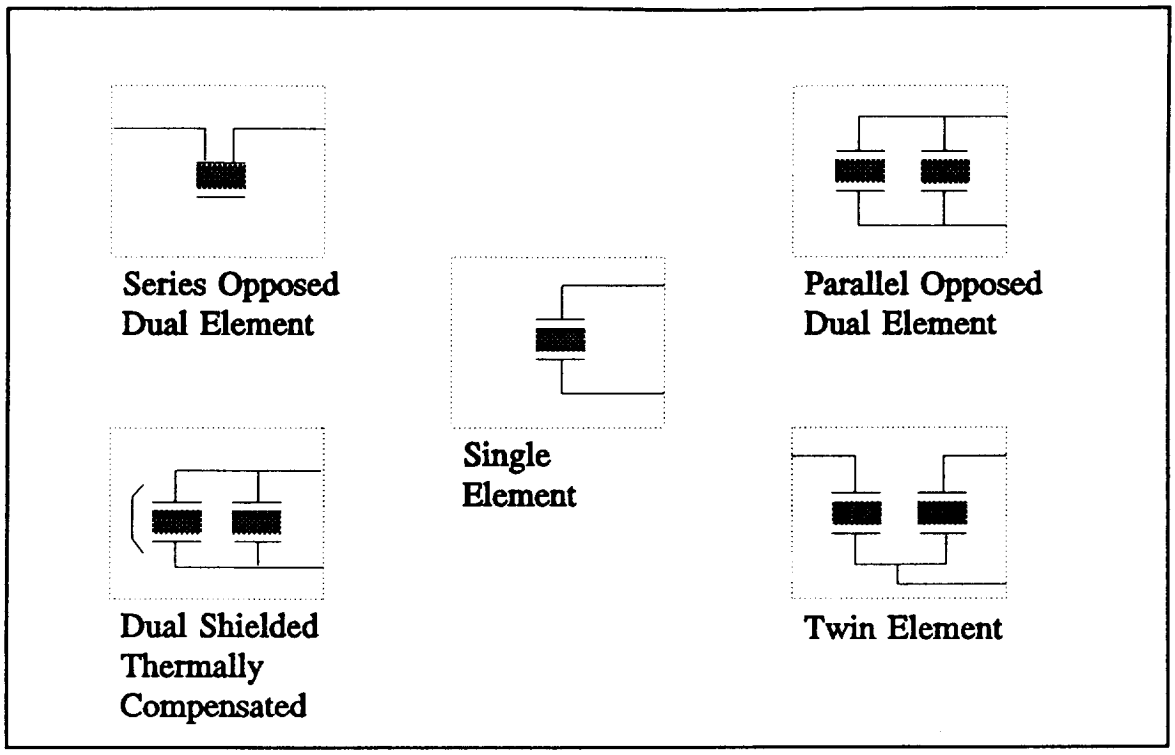

Figure 3.2 Arrangement of pyroelectric crystals [Cima, 1992]

is its low noise capabilities. With the dual element, the configuration of the elements in the housing is varied according to usage. The parallel configuration increases the field of view, and the series intensifies an area's sensitivity. An additional option on the single element detector is to have the element resting on the case rather than suspended, turning the case into a heat sink for the detector. This makes the detector an ideal laser detector because of the large changes in energy the detector faces.

The materials used for these elements vary depending on the usage of the circuit. Depending on what light is being measured, a certain material could be preferred over another, because of thermal properties, the Voltage-Current characteristics over certain operation ranges, or some other criteria. For example, for

laser detection purposes, a Lithium Tantalate Pyroelectric Detector could be used because of the good thermal properties of the material [Cima, 1988], while a Silicon photodiode would be good because of its wide spectral range.

The third option used in detector selection is whether or not additional electronics are to be included in the package. For home or commercial usage, the detectors come with electronics already included for specific implementations, e.g. motion detectors, fire detection systems, or climate control. With some uses, such as high power lasers, the circuitry is safer outside of the detector package. With lasers, the sensor will face major temperature changes in short amounts of time, so additional electronics inside the detector package would also be affected by those changes.

The next sections discuss the types of detectors and their operations in more detail. While being similar in some respects, the devices have various properties which make the two different. Also discussed is which detector was used for the experiments and why.

2.1 Photodiode Operation

With photodiodes, a Silicon Photodiode would be acceptable for laser detection because of the wide spectral response, from around 190 nm up to about 1100 nm. Laser systems typically produce a spectral range of about 200-900 nm. Other types of photodiodes exist but their spectral range is not as vast. GaAsP and GaP photodiodes can measure the low end of the needed spectrum, but

most cut out at about 700 nm, leaving the higher wavelengths undetected.

For photodiodes, the term responsivity is used to measure the

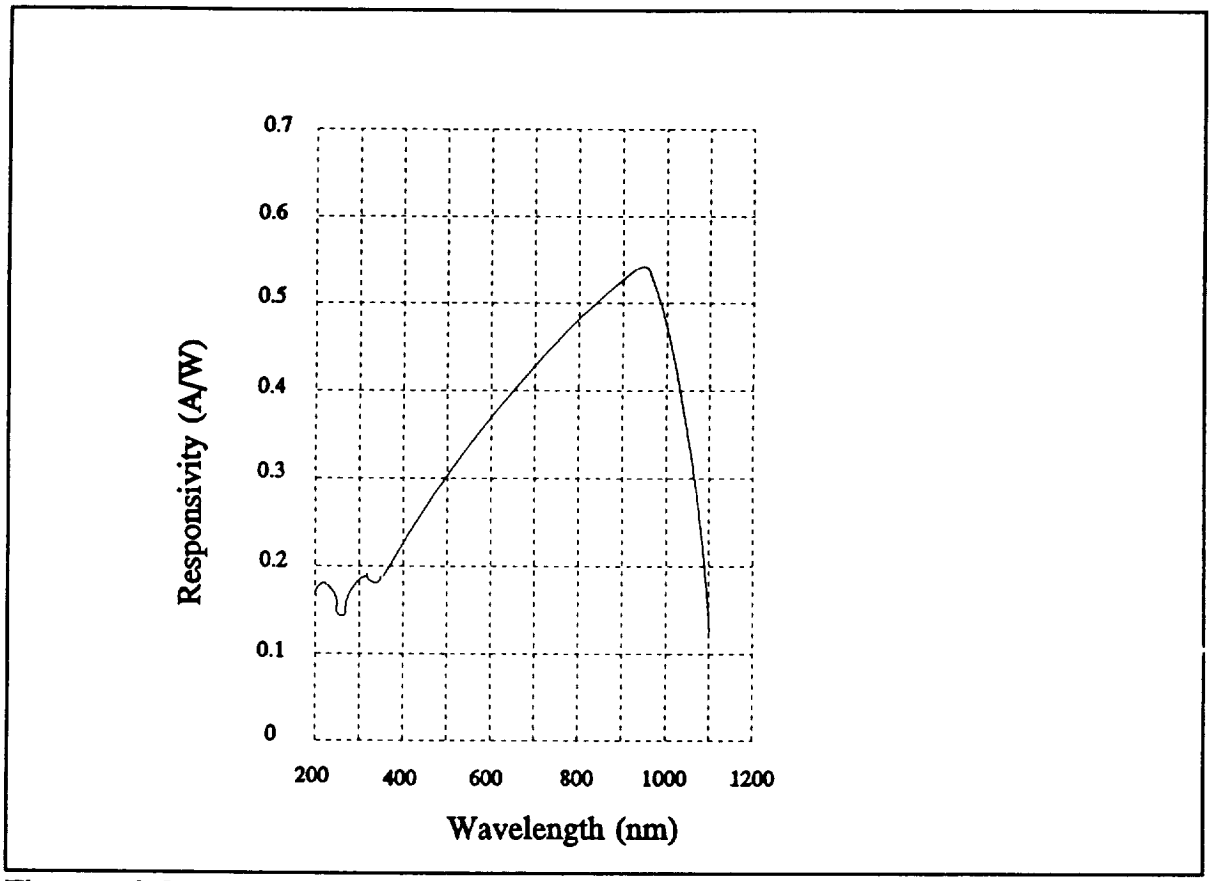

Figure 2.3 Responsivity curve for Silicon Photodiode showing wavelength dependence[Centronic, 1989]

sensitivity to light; the ratio of the photocurrent to incident light. Each type of photodiode has a unique response to the light, depending on the wavelength. (Fig. 2.3)

With the photodiode, the current out of the diode, I_p, is a

$$I_P = \frac{V_{IN}}{R_L} \qquad 2.1$$

function of the load resistance, R_L, and input voltage, V_{IN}. With the current now known, the intensity of the beam, P, in Watts, is a function of the responsivity of the detector, R_I, which varies with wavelength, and photodiode current, I_p.

$$P=\frac{I_P}{R_I} \qquad 2.2$$

The intensity of the beam is the power dissipated.[Hamamatsu, 1991]

2.2 Pyroelectric Detector Operation

Calculations for the pyroelectric detector are a little more complicated. Depending on the usage of the detector, laser detection especially, the calculations change because of the external electronics. The sensitivity of the pyroelectric detectors to temperature is also referred to as its responsivity, either current (Amperes per Watt) or voltage (Volts per Watt). The current responsivity, a mechanical constant stated by the manufacturer is related to the material being used for the sensing element and the separation of the electrodes on the device, totally independent of the wavelength of the beam.

$$R_I=\frac{\tau}{d} \qquad 2.3$$

[τ = material parameter, d = separation of electrodes]

With lasers, the voltage responsivity, R_v, is a function of the

current responsivity, R_I, and the effective impedance of the circuitry used in with the detector, Z_{eff}, a function of the modulation rate of the beam.

$$Z_{eff}=\frac{R_L}{\sqrt{1+R_L C_D \omega^2}} \qquad 2.4$$

[C_D = capacitance of the detector, w = $2\pi f$]
[R_L = load resistance]

With the effective impedance found, the voltage responsivity is now found by the effective impedance and the current responsivity, [Cima, 1992]

$$R_V=Z_{eff}R_I \qquad 2.5$$

After the initial power is measured, another power could be measured to find details about the different laser pulses. With this type of calculation needed, many of the previous calculations are unnecessary, with all of the constants cancelling out.

To start, the powers of both pulses are found (Eqs 2.6 & 2.7), then divided to get the ratio of the powers. For a relative

$$P_1=\frac{V_1}{R_V} \qquad 2.6$$

$$P_2=\frac{V_2}{R_V} \qquad 2.7$$

measurement, dividing equation 2.6 by equation 2.7 cancels out the responsivities, giving

$$\frac{P_1}{P_2}=\frac{V_1}{V_2} \qquad 2.8$$

This relative power calculation works only if the same detector is used for both measurements. If two different detectors were used simultaneously, measuring the beam reflections at different points, the responsivities between the two units are different. So the division of equation 2.6 by equation 2.7, substituting Eqs 2.4 and 2.5 gives

$$\frac{P_1}{P_2}=\frac{R_f R_L}{\sqrt{1+R_L C_{D1}\omega^2}} * \frac{\sqrt{1+R_L C_{D2}\omega^2}}{R_f R_L} * \frac{V_1}{V_2} \qquad 2.9$$

The load resistances cancel, and the ratio cancels down to

$$\frac{P_1}{P_2}=\frac{\sqrt{1+R_L C_{D2}\omega^2}}{\sqrt{1+R_L C_{D1}\omega^2}} * \frac{V_1}{V_2} \qquad 2.10$$

While this expression gives a different value for the power ratio, depending on the values of the detector, the difference might be negligible, making the first fraction of equation 2.10 equaling very close to 1, so the final ratio will once again be

$$\frac{P_1}{P_2}=\frac{V_1}{V_2} \qquad 2.11$$

This ratio shows that the change in the power of the beam is

directly proportional to the change in voltage out of the detector.

2.3 Device Selection

The output voltage of the photodiodes and pyroelectric detectors is directly proportional to the power measured because the responsivities of the detectors are constant in this usage. Furthermore, since the goal of this project was to measure relative powers, the direct relationship of the voltages out of the detector is all that was needed to find the variance between the laser pulses, or shots.

For choosing the device to use, while the photodiode circuit seems better because of its simplicity, it does not have the best range of operation. Another goal of this project was to have the detector compatible to many laser systems. The photodiode's wavelength sensitivity limits the amount of systems which it could be used on while the pyroelectric detector operates independent of the wavelength, therefore, the pyroelectric detector was best for this application.

For this project, an Eltec 420M3 Pyroelectric Detector was chosen and the circuit for amplification of the detector signal had to be designed, along with the circuit to allow for the digitization of the detector pulse. The next chapter decides between the operation mode of the detector and how to make the signal compatible for the digital conversion.

Chapter 3

Detector Operation and Circuitry

For this experiment, the detector, when placed in the path of the beam reflection, needed to send the signal for data acquisition. A circuit had to be designed to take the detector response, amplify it, and send the signal to the acquisition equipment. There were two approaches to this method: first was to implement the detector as a current source using operational

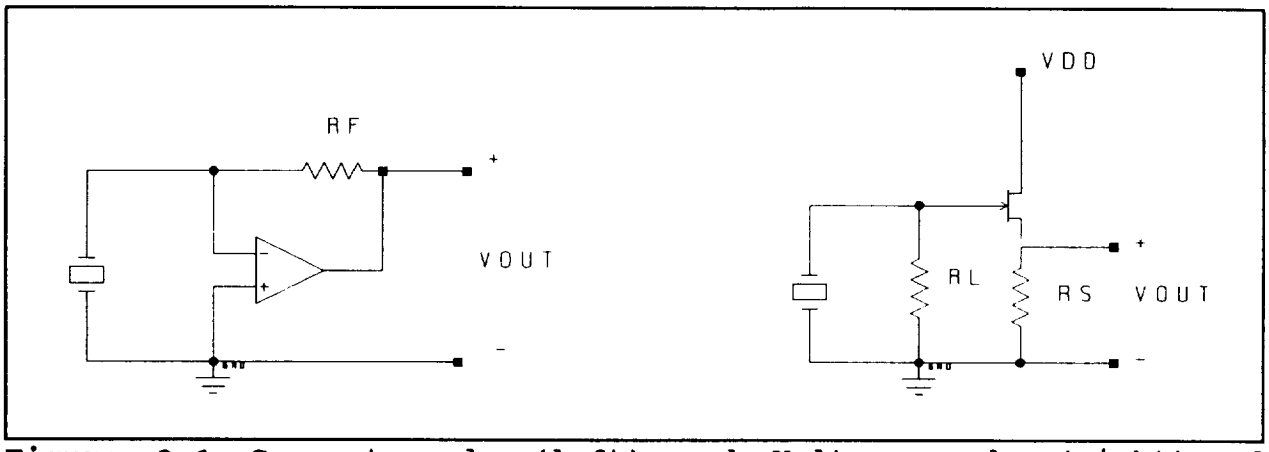

Figure 3.1 Current mode (left) and Voltage mode (right) of operation [Eltec, 1990]

amplifiers, or, second to use the detector as a voltage source aided by transistors.(Fig. 3.1) After the beam was detected, it had to be slowed down for digitization to send the signal to a computer for storage. The existing equipment in the laboratory for data storage worked much slower than the expected operation rate of the detector circuit, so after the signal was detected, it was to be converted for compatibility with the equipment.

NASA's Combustion Diagnostic Laboratory used the detector circuits to normalize signals from other experiments as a function of the laser intensity and to characterize the laser's stability.

The detectors were never exposed to the entire beam, only about 4% of it, the expected amount of reflection from the optic. The power was measured from the reflection along the beam path, giving a relative measure. Because of the need for a universal detector system, a circuit with a totally linear response was needed for proper manipulation of the data. The Eltec 420M3 pyroelectric detector's response was .319 Microamperes per Watt, so the detector circuit needed a full linear response, even for low ranges of operation in case a low power laser was used.

3.1 Current Mode of Operation

The first approach for pulse measurements, the current mode of operation, was undertaken around 1984 by NASA [Vander Wal, 1993],

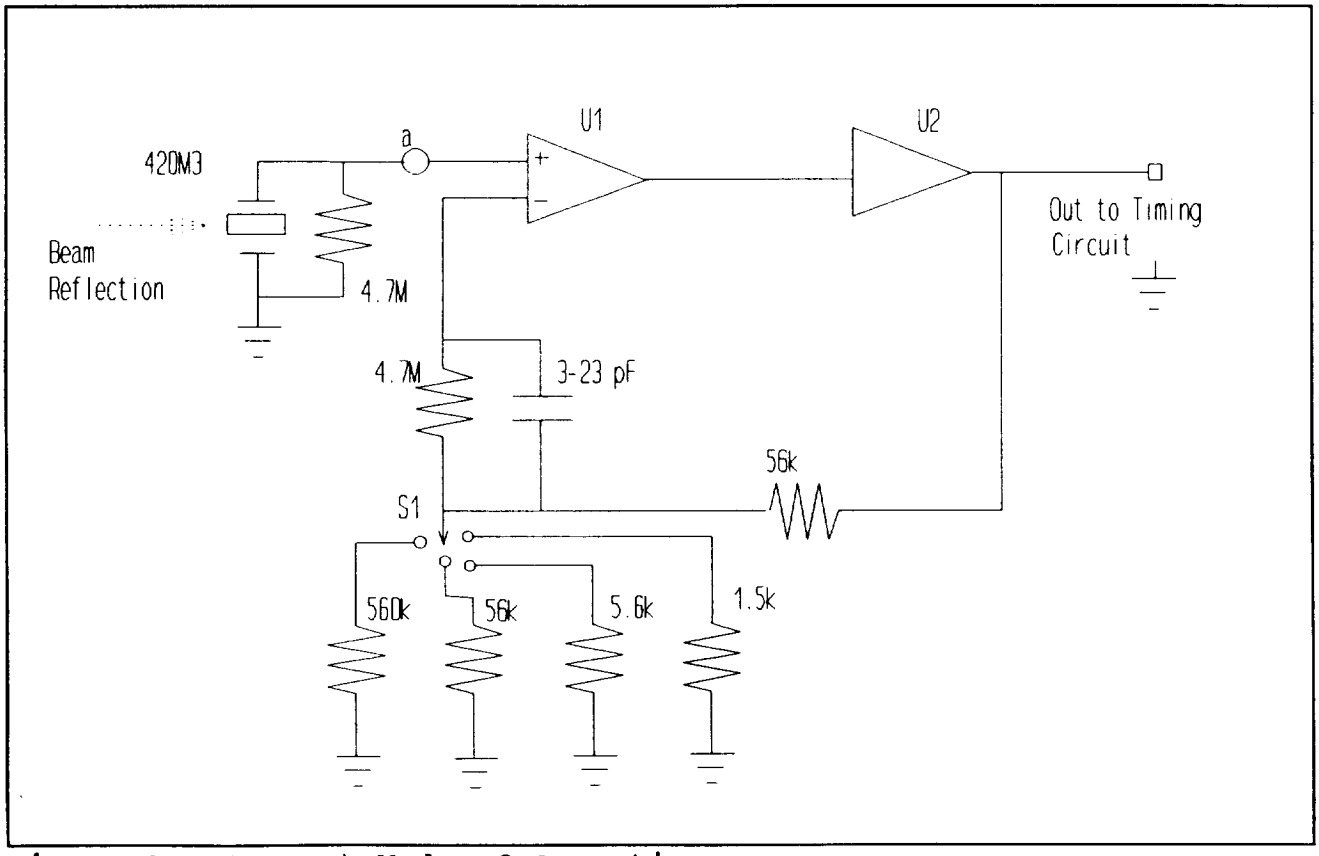

Figure 3.2 Current Mode of Operation

using pyroelectric detectors and op-amps. (Fig. 3.2) The current mode of operation worked on the basis that the output current was proportional to the input current, with the proportionality depending on the placement of the switch, S1, giving different gains for each switch placement. So depending on the switch placement, gains of 1.1, 2, 11, or 38 were possible. Figure 3.3 shows the response of the current mode circuit with a gain set at

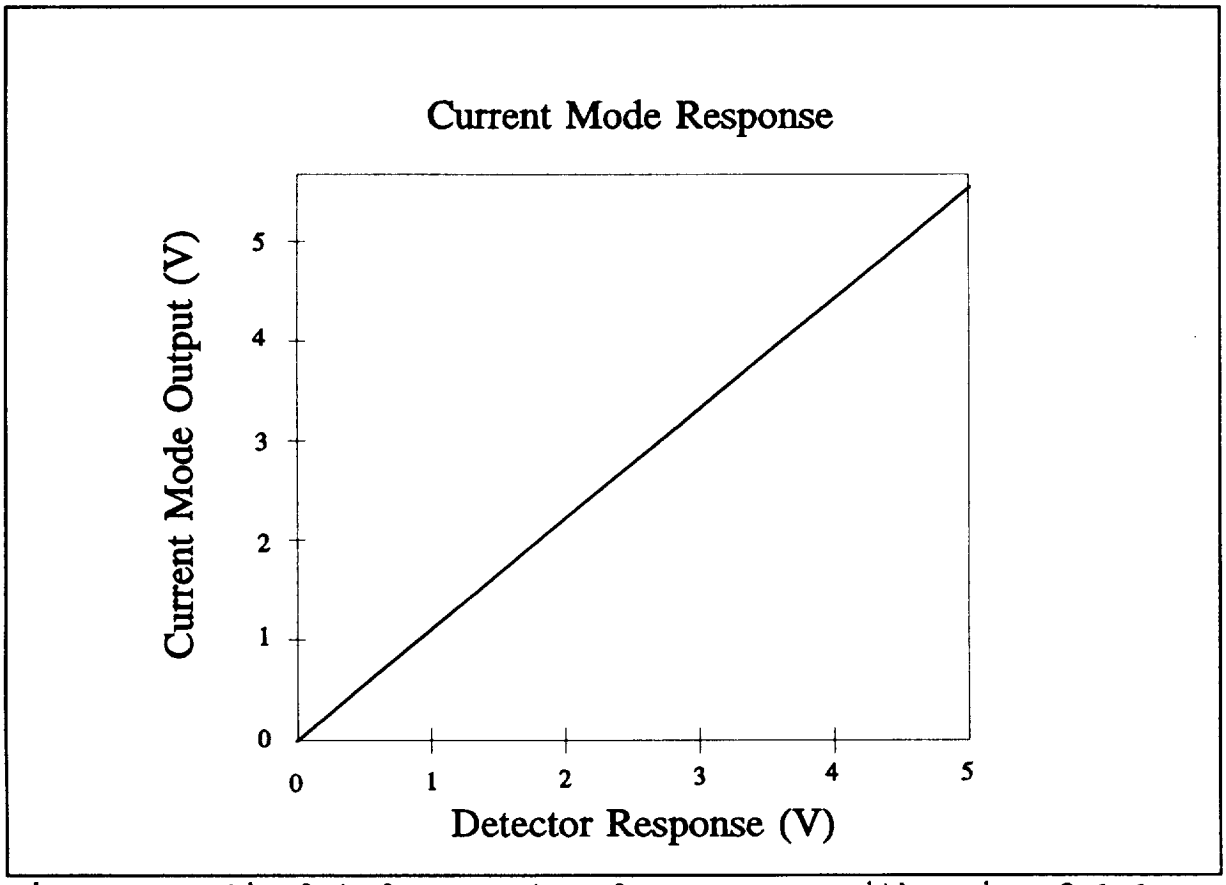

Figure 3.3 Simulated current mode response with gain of 1.1

1.1. The input signal to simulate the response of the detector was supplied by a voltage source substituted at point (a) in the circuit. The current mode gives a linear response through its entire operation, so the output of the circuit is always directly proportional to the detector output.

The circuit had size limitations, it had to be small, small enough to fit in a 3" x 2" x 1" box. Because of the op-amps threshold voltages, an additional power source, a +/-15 Volt supply, was needed. The smallest +/-15 Volt supplies available came in packages of 2" x 2" x ¼" and required an additional outside source of +/- 28 Volts. Another available supply was a 3½" x 2" x 1½" supply which could be hardwired into an ordinary AC wall socket. This type is a little more convenient for laboratory use, but impossible for microgravity use. This circuit was not easily portable for measurements of different systems due to the outside power source; there would have to be an extra power line for it to function.

Because of the strict size and portability constraints for the circuit, the current mode would be impossible to build to those standards, but accommodations to use the circuit were possible. Powering the system from the outside eliminated the possibility of this circuit being easily portable. Higher voltage batteries are available, but to achieve the negative voltage needed for the thresholds of the op-amp, a second battery was needed, and once again the problem of size emerged. Because of these set-backs in the current mode, the alternative voltage mode was to be considered to see if these problems could be overcome.

3.2 Voltage Mode of Operation

The second approach, the voltage mode of operation, attempted during this project, was a smaller and more portable system. (Fig. 3.4) The voltage mode circuit gives an output voltage that

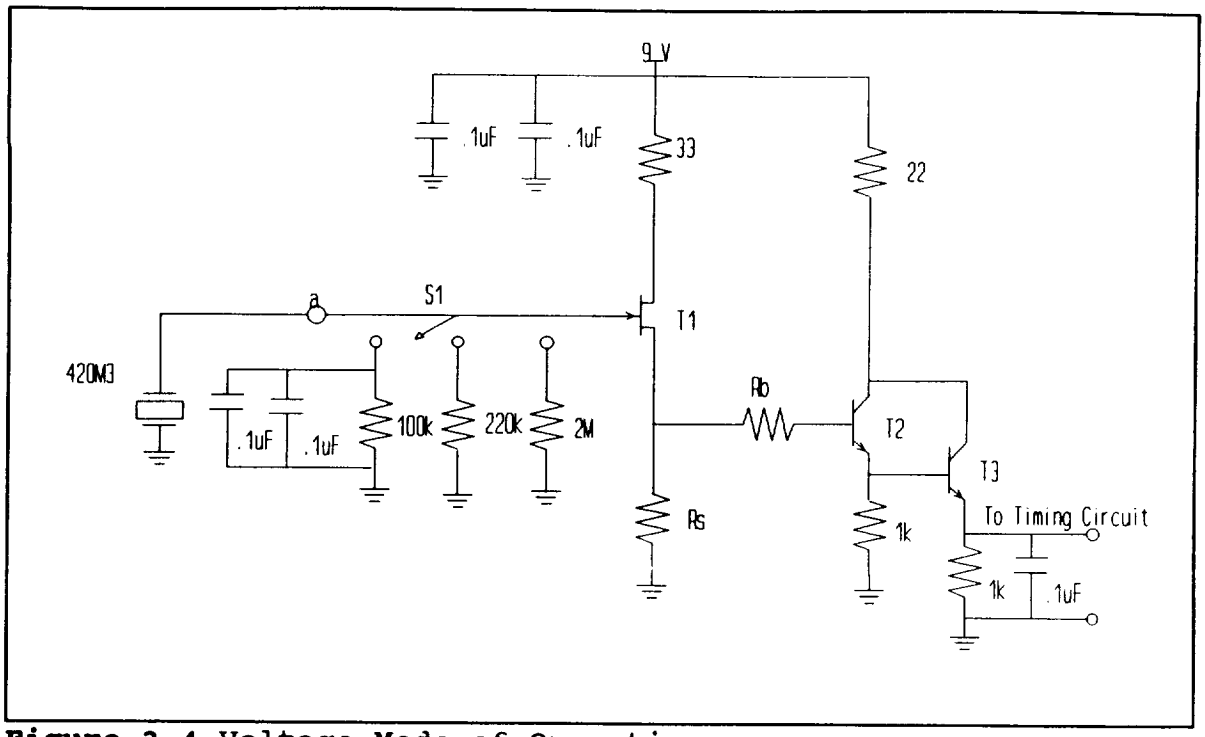

Figure 3.4 Voltage Mode of Operation

corresponds to a voltage given by the detector. The switch, S1, in the circuit controls the rise and fall times of the detector by changing its load, smaller pulses using the 100kΩ resistor and larger pulses using the 2MΩ.

Using the simple voltage mode circuit, like in Figure 3.1, an offset occurred. When the detector had no beam striking it, there was an output voltage. The second stage of this circuit, T2 and T3, were added to eliminate that offset. What was desired was a 0 Volt output with no beam striking the detector. By adding these transistors and nullifying the offset, T2 and T3 were operating in the triode region, causing an exponential response. Figure 3.5 shows the response of the voltage mode circuit, with the same voltage source substitution as the current mode simulation, and clearly shows the exponential output of the system due to those transistors.

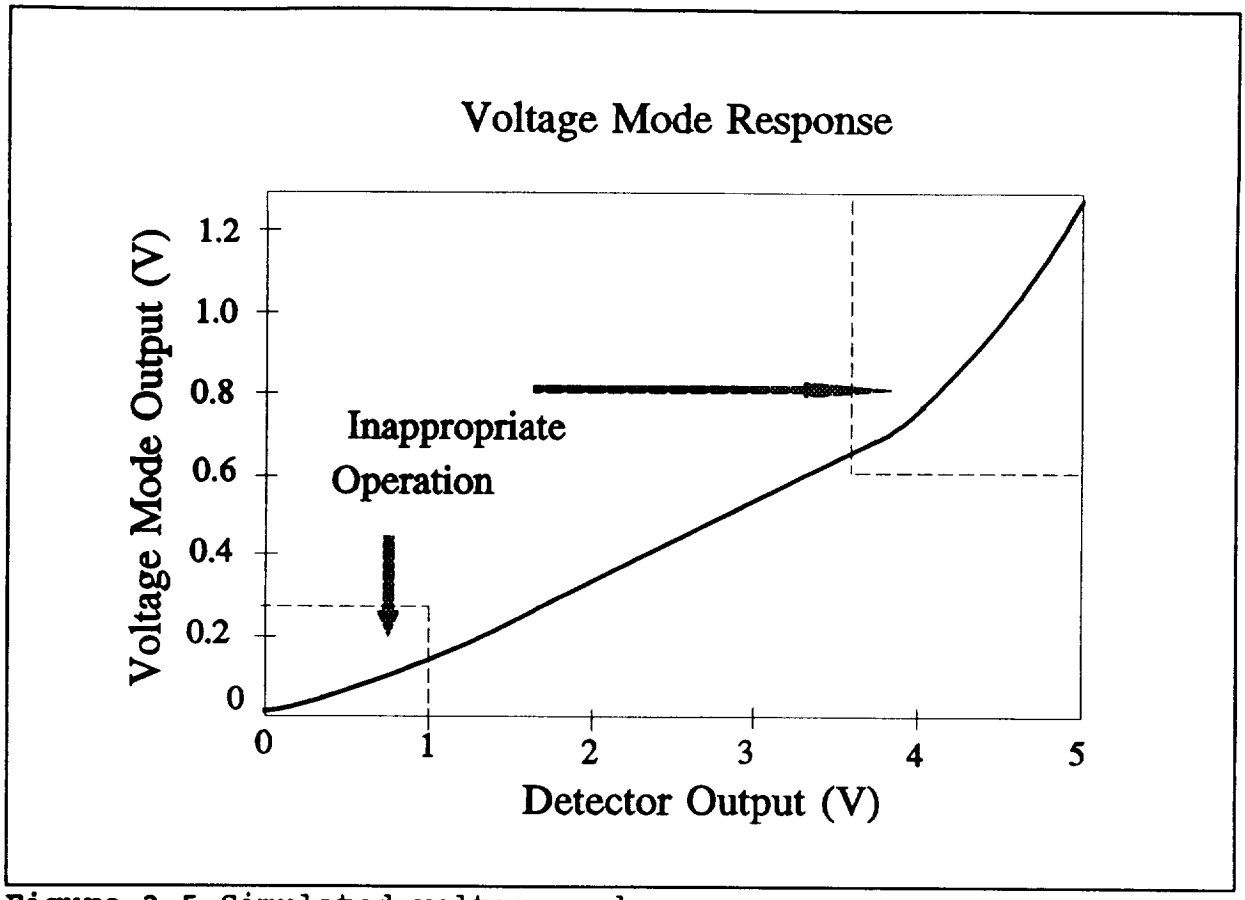

Figure 3.5 Simulated voltage mode response

The power needed to run this circuit was an ordinary 9 Volt battery, much smaller than the supply in the first circuit and could easily fit into the given size requirements. Another attribute to the voltage mode was that it was totally portable. In a small box with no inputs other than the detector on the top of the box, all it needed to work was the laser. A down side to this approach was the overall response of the circuit. The voltage mode did not give a perfectly linear response to the detector output compared to the current mode's operation. Although the circuit has linear ranges in its output, it was necessary for the response to be uniform for all ranges. In the range from 0 Volts to about .75 Volts, the circuit has an exponential response, then becomes linear, with a change in linearity around 4 Volts. Because of the

need for a perfect linear response in order to better see the variances on all laser systems, the voltage mode circuit's operation was unacceptable. The voltage mode would be much better suited for singular laser systems.

3.3 Circuit Selection

It was determined by inspection of the circuits' responses that the current mode was more appropriate. For all inputs, the circuit gave a linearly proportional output. In order to find relationships between two laser pulses, a division between the two pulses would show the percent variance. With the voltage mode, the output started off exponentially, then straightened out for a linear output. Having the exponential output in the lowest range of the voltage mode made the idea of using the transistors unreliable because of the non-linear response in the low range. Because of that non-linear response, comparing two pulses in the low voltage range would not show an accurate percent difference between the pulses. Because of the detectors exponential rise and decay, the detector circuits needed a purely linear response for accurate relative measurements.

One goal of the detector circuit was to have a perfectly linear output for all of the ranges the detector would face, for low power and high power systems. In NASA's use of the circuit, the detector would not always enter the linear range of the voltage mode's transistors. The linear operation of the detector circuit was desired for simpler calculations when comparing laser pulses as well as for a universal detector unit.

The other goal was to have a small detector circuit which could be portable. In order for the current mode to be portable, there would have to be an existing power supply where the circuit was to be used. In all of the laser experiments, there are power supplies already being used in the experiment. For detecting the laser, the current mode was the most reliable because of its totally linear response, and was to be used in the microgravity experiments to obtain the relative power measurements.

3.4 Timing Circuit

Because of the slow Analog to Digital converter already in the lab being used for data acquisition, the detection signal had to be slowed down to be noticed. The high speed of the laser pulse and thermal characteristics of the detector made it impossible for the signal to be sampled. The signal out of the current mode needed to

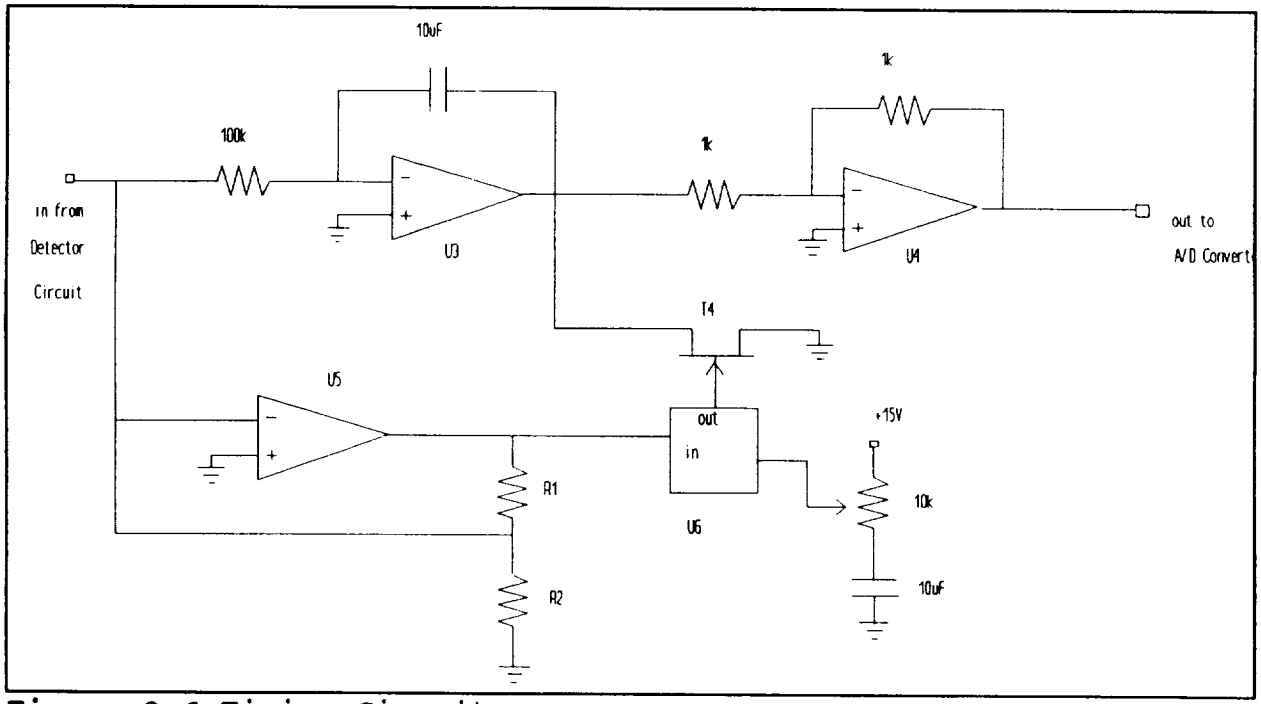

Figure 3.6 Timing Circuit

be stretched long enough for the converter to recognize it. The signal out of the detector circuit lasted for about .1 ms, and the converter had a sampling time of 1 ms. A circuit was designed for the acquisition, and is shown in Figure 3.6.

The timing circuit was fed the output of the detector circuit, integrated by U3, and inverted by U4 for the acquisition equipment. The signal was integrated to "stretch" the signal for compatibility with the A/D converter, providing an analog memory of the beam intensity. Then the signal was inverted to get a positive output because of the negative signal of the integrator. The signal was also amplified along a second path and run into a timing chip to clear the integrator for the next pulse coming from the detector circuit.

Along the second path, the signal coming from the detector circuit was amplified so the timing chip would respond to the signal. The LM555 timing chip responds to a minimum voltage of 1.67 V, and the signal coming out of the detector circuit was in the millivolt range, so amplification was needed for proper operation.

The FET connected to the output of the LM555 cleared the integrated signal, with the clearing depending on the time constant set by the resistor and capacitor connected to the timing chip. For these experiments the timer cleared the signal every 20 ms, giving a measurement for individual pulses. Figure 3.7 shows the circuit operation, using a pulse generator for the input.

The following chapter discusses how these circuits, the current mode detection circuit and timing circuit, were to be used in conjunction by NASA's Combustion Diagnostics Laboratory in their

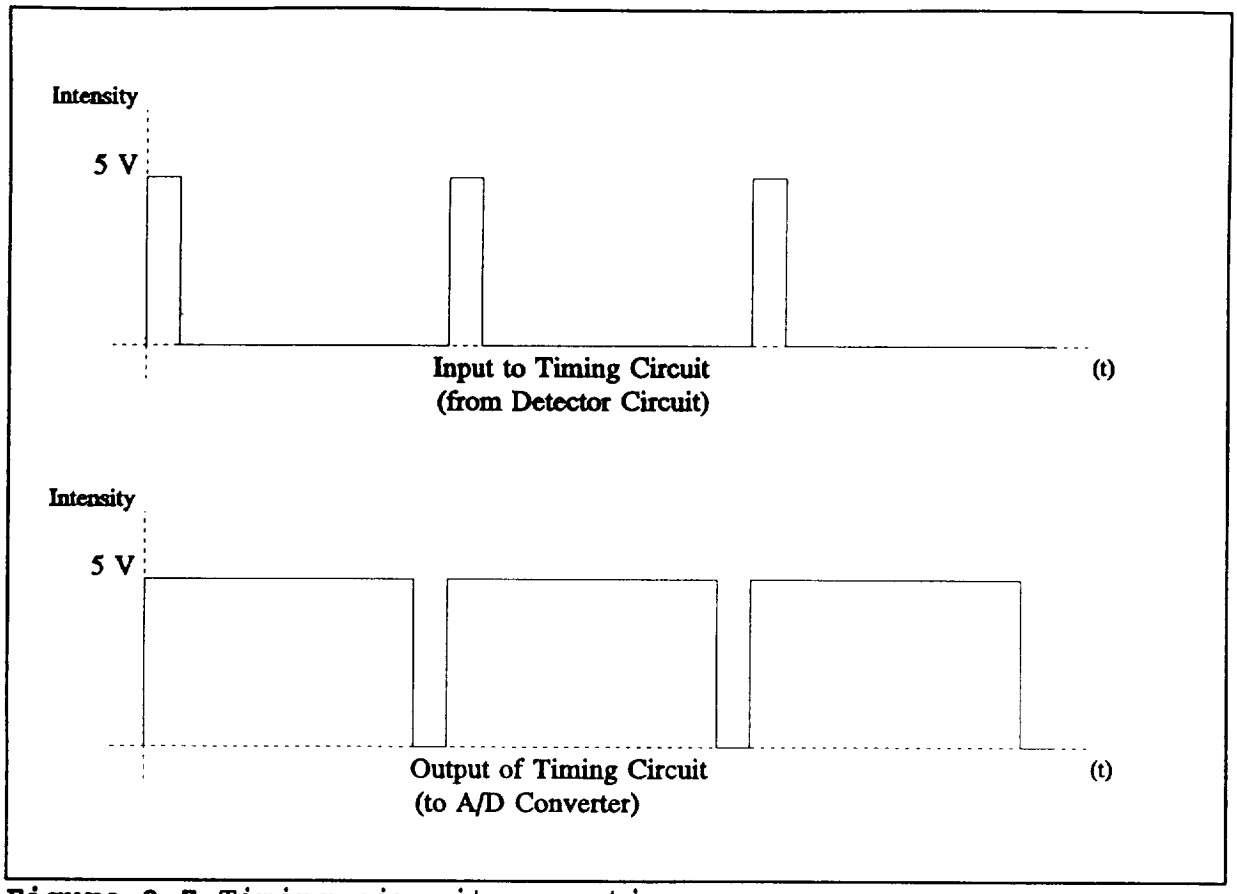

Figure 3.7 Timing circuit operation

combustion experiments. It discusses how both the detector circuit and the timing circuit work together and how the data from these circuits was to be used for a better understanding of the experiments.

Chapter 4

Detector Design Analysis

At the time of this writing, the laser system which the detector was to be used on for the experiments was not operating. Therefore, this chapter will explain how the detector was to operate and how that information was to be used in the microgravity experiments. Information in this chapter was taken from the manufacturer's specifications of the parts being used in the circuits, from experimental tests of the circuits independently and from conversations at the NASA Lewis Research Center.

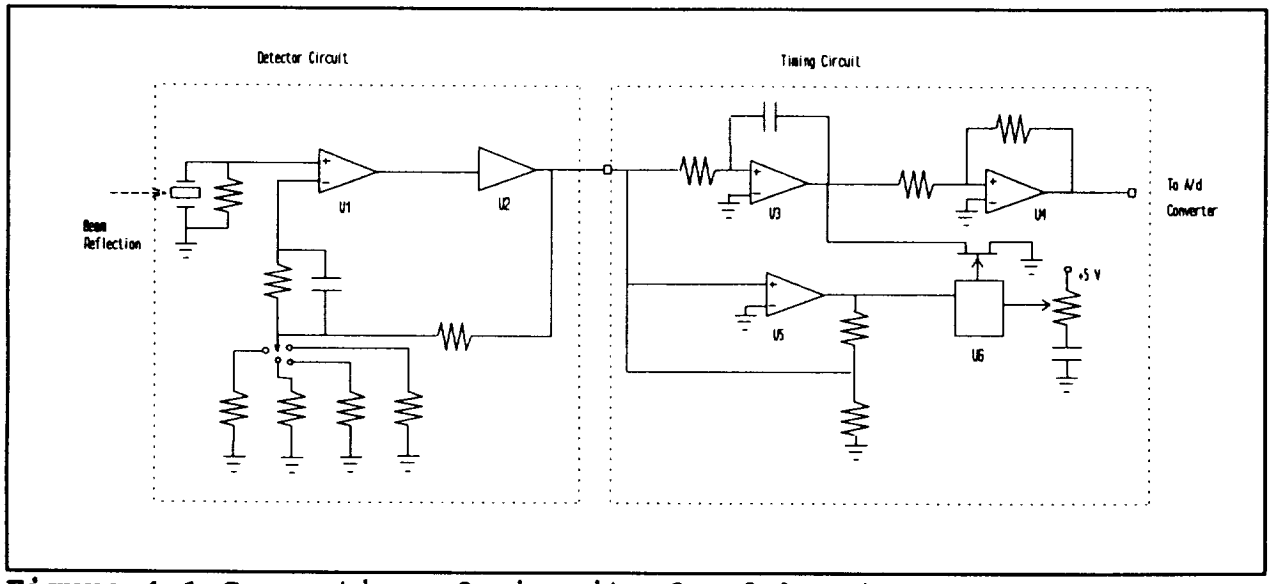

Figure 4.1 Connection of circuits for laboratory use

The laser system which this detector system (Fig. 4.1) was to be used on primarily was a pulsed solid state laser system, capable of firing a 5 ns 330 mJ pulse every 20 ms. Because of the operating parameters of the laser, the pulse could vary anywhere from 314 - 346 mJ. The detector and timing circuits' purpose was to isolate the differences in each individual laser shot.(Fig. 4.2)

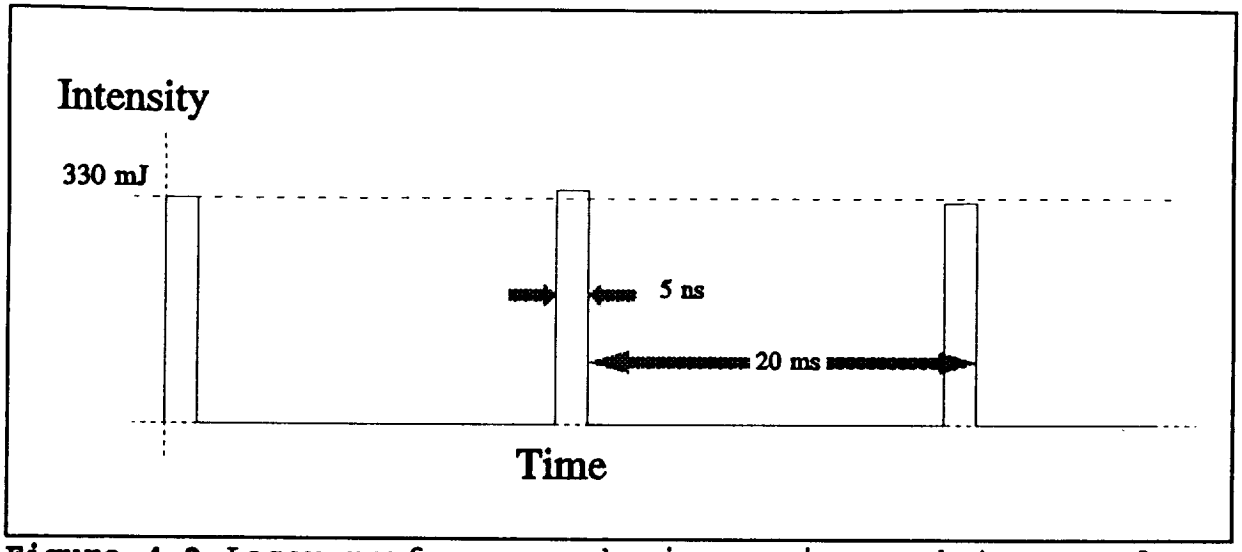

Figure 4.2 Laser performance showing variances between pulses, seen by the pyroelectric detector

As the detector responds to the laser pulse, the op-amp (U1) and current amplifier (U2) in the detector circuit boosts the signal from the pyroelectric detector and send it to the timing circuit. This signal from the detector itself and the signal out of the detector circuit are identical (Fig. 4.3) in form, but the signal out of the circuit is of a higher magnitude.

The integrator and inverter in the timing circuit now makes a "stretched" signal to send to the computerized acquisition

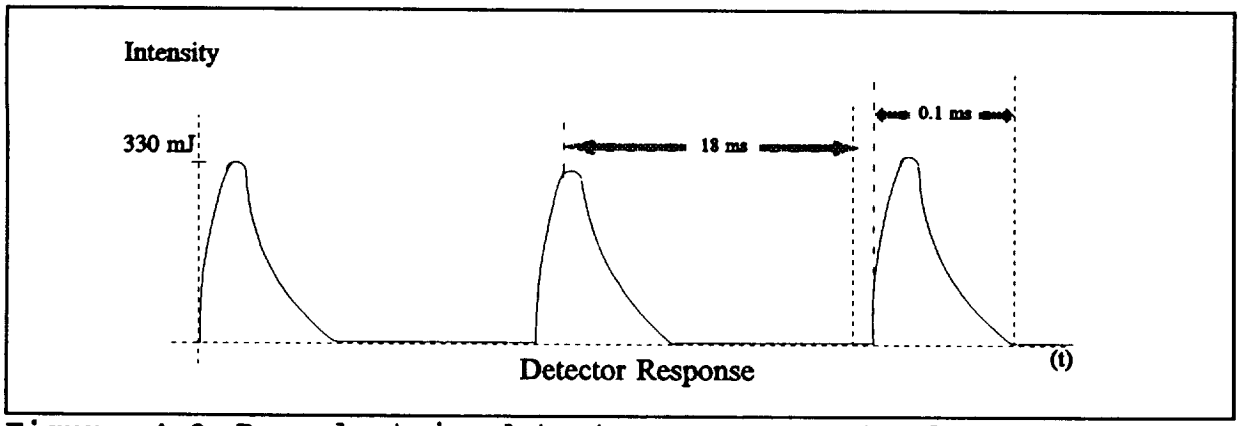

Figure 4.3 Pyroelectric detector response to laser pulse and integrated response

equipment, with the timing chip clearing the integrated signal prior to the next signal from the detector circuit, sending a shot to shot representation of the laser power to the A/D converter. (Fig. 4.4)

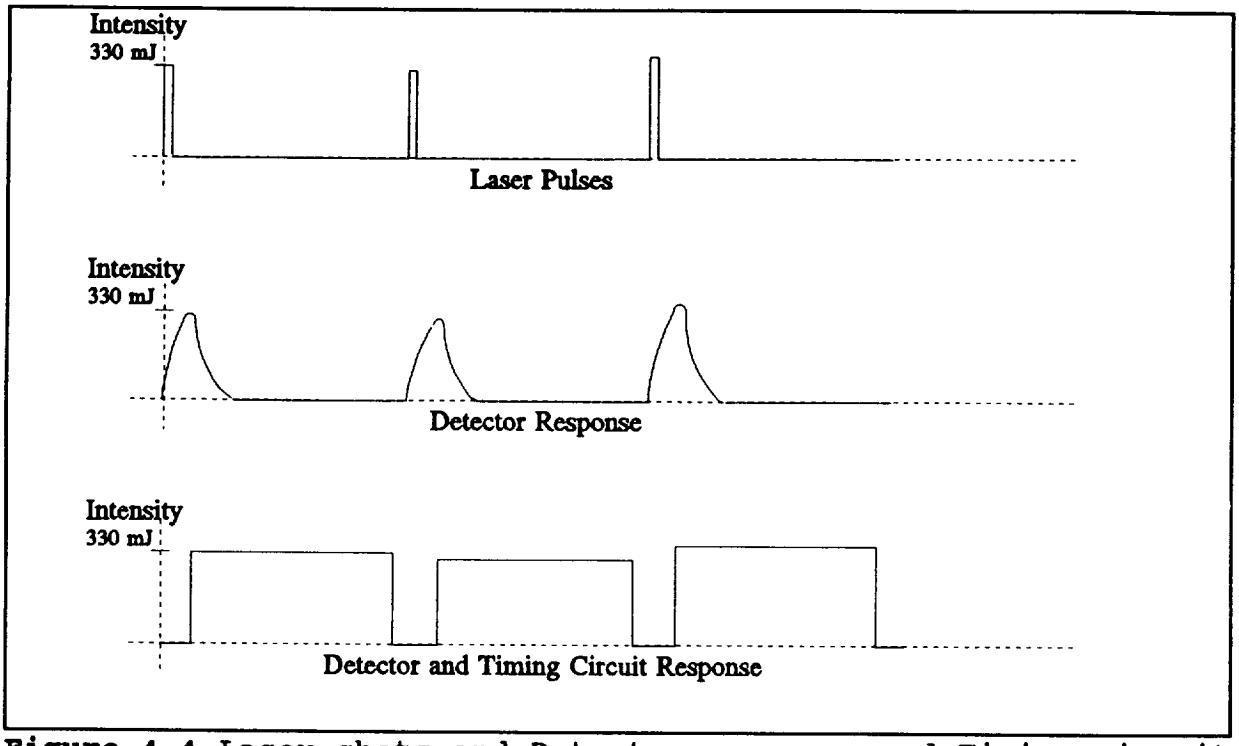

Figure 4.4 Laser shots and Detector response and Timing circuit response to the Laser shots

Now with the intensity measurements from the reflected beam, the other combustion experiment(s) conducted using the original beam can be matched up to its corresponding laser power measurement. By comparing the two different sets of pulses, the combustion experiments can be seen now as a function of the laser power intensity. The comparison between pulses shows the fluctuation of power. For a 2% increase in laser intensity, an ionization rate may have matched that with a 2% increase. On the other hand, a species concentration might have changed, but with a 4% increase. As the laser power varies, the other experiments will vary, most with different characteristics. There could be a direct

1:1 relationship between the power and one experiment, another having a 1:2 relationship, while a third could have a 2:1 relationship. Now this information can be used to make predictions for future experiments, whether in microgravity or not.

Chapter 5

Conclusion

In combustion experiments, whether in microgravity or not, the results can depend on the laser power intensity. But the results can not be fully understood until an accurate measure of the laser power is taken. Experimental results have small variances because of the lasers operating range, usually +/- 5% of the stated power. These variances can be blamed on the instability of the laser, but can not be accepted until the pulses are measured individually. Sometimes other factors, such as differences in the environment or materials cause fluctuations as well.

A portable laser pulse detection system was developed which could operate on multiple laser systems. A design existed with a few shortcomings, and a new design was made as an attempt to eliminate those problems. Once the detection device was decided, a pyroelectric detector, the modes of the detector could be tested. The newer design, the Voltage Mode of Operation alleviated the problems of the older circuit, the Current Mode of Operation, but new problems emerged with the voltage mode. The detector mode had to give a perfectly linear response to the detector output, which the Voltage Mode did not. The Current Mode of Operation responded better for their purposes.

Once the operation mode of the detector was completed, the signal was sent to some computerized acquisition equipment. With slight modifications to the signal out of the detector circuit, the signal was compatible with their computerized acquisition system.

The pyroelectric detector and detector circuit system was

tested and its response was acceptable for all of the conditions it would face in the laboratory. The response of the circuit was a proportional response, as the laser power was doubled, the output of the detector circuit doubled, making the change in the laser power easily determined from the response of the circuit. By using a pyroelectric detector instead of a photodiode, the detector could be used on a laser system of any wavelength without chance of the device being outside of its operation range.

The timing circuit operation was verified with a pulse generator. A pulse was applied to the circuit, and the pulse was integrated and inverted along one path, and cleared every 20 ms by the timing chip and FET on the other path. By adjusting the RC network connected to the timing chip, the clearing signal could be adjusted to suit many different laser systems.

With the detector and timing circuits, the laser was monitored on a shot to shot basis, instead of over a multiple shot period as before. Previously, the laser power measurements were averaged over many shots, leaving an unacceptable margin of error in the calculations. The energy reading of the shots was a sum of all of the shots, then an average value was found. So the data was looked at with the assumption that all of the laser shots in that period were all of the same magnitude. Some of the shots could have actually had that average value, but the likelihood of all having that value is improbable. Now, with the detection and timing circuits, each shot has its own peak, not groups of shots having the same peaks.

With the power measurement for each shot, the combustion experiment(s) conducted can be shown as a function of the laser

power intensity. As the power of the laser changed, the response of the combustion experiment could be looked at to find the dependance on the laser intensity.

By knowing the dependance the experiments have on the laser power, the experiments can be better understood in microgravity. In a run of the experiment in regular gravity, the dependance on the laser power is found, and now when conducted in microgravity, the response of the experiment will have a different response due to the change in gravity. Now the power is known, so the dependance on other factors, like gravity, can be found.

With exact power measurements, the error is drastically reduced, giving much more valid results, and better predictions can be made in future experiments. By looking at the response of the combustion experiment at just one power setting, guesses and assumptions can be made. By taking the fluctuations in one experiment, the response of the same experiment can be predicted for another power setting with a reasonable degree of confidence.

Recommendations for Future Study

For future projects,some changes could be made to the detector design to make the system totally portable, removing its dependance on the +/- 15 V supply. To try this, a redesign of the voltage mode circuit would have to be considered, getting a linear response for the lower voltage range of the transistors.

Other types of detection equipment for the laboratory could be designed and constructed, such as circuits for measurement of flame temperatures, ionization rates, or other such experiments. In

addition, the equipment in the lab, oscilloscopes, A/D converters, and cameras, need interfacing with the computer for data acquisition. Also, using data from the experiments, the combustion phenomena needs normalization as a function of laser power intensity.

References

Centronic Inc, (1989); "Photodiode Catalog," Centronic Inc.; USA.

Cima, D., (1988); "Laser Detection With Lithium Tantalate Pyroelectric Detectors," Eltec Instruments, Inc; USA.

Cima, D., (1992); "Choosing and Using Pyroelectric Detectors," Eltec Instruments, Inc; USA.

Eltec Instruments, Inc., (1990); "Introduction to Infrared Pyroelectric Detectors," Eltec Instruments, Inc; USA.

Hamamatsu Corporation, (1991); "Photodiodes, 1991 Catalog," Hamamatsu Corporation; Japan.

National Aeronautics and Space Administration, (1992); "Microgravity Science and Applications Program 1992 Annual Report", U.S. Government Printing Office.

National Aeronautics and Space Administration, (1992); "The First United States Microgravity Laboratory", U.S. Government Printing Office.

Vander Wal, Dr. R.; "Personal conversations with C. Toth,"; 1 June 1993 - 8 August 1993.